Eindhoven University of Technology

MASTER

Study of the Airflow between the Railway Track Recording Vehicle Underbody, and Ballast Track Bed

Reimerink, Jeroen

Award date:
2021

Link to publication

Disclaimer
This document contains a student thesis (bachelor's or master's), as authored by a student at Eindhoven University of Technology. Student theses are made available in the TU/e repository upon obtaining the required degree. The grade received is not published on the document as presented in the repository. The required complexity or quality of research of student theses may vary by program, and the required minimum study period may vary in duration.

General rights
Copyright and moral rights for the publications made accessible in the public portal are retained by the authors and/or other copyright owners and it is a condition of accessing publications that users recognise and abide by the legal requirements associated with these rights.

- Users may download and print one copy of any publication from the public portal for the purpose of private study or research.
- You may not further distribute the material or use it for any profit-making activity or commercial gain

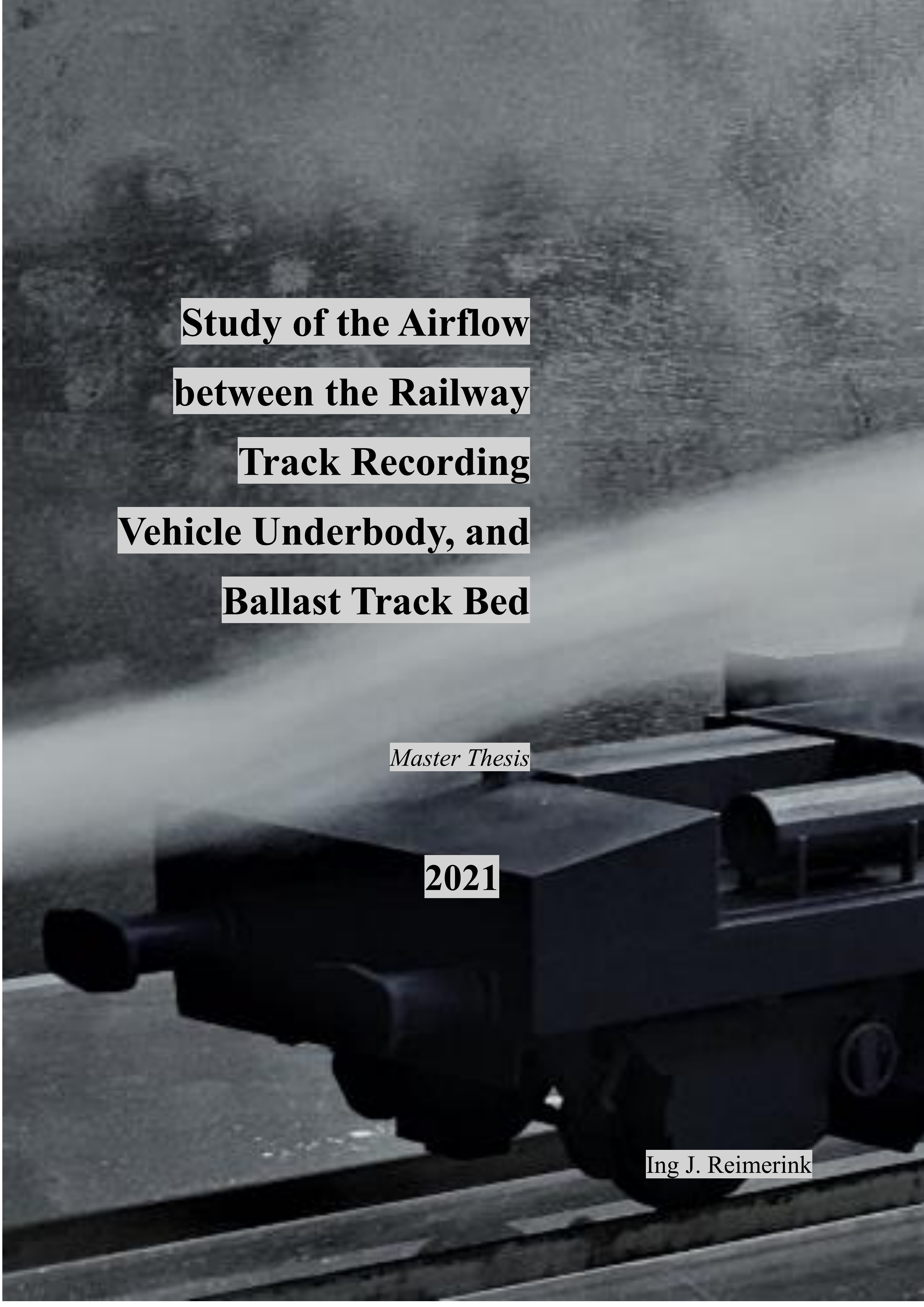

Study of the Airflow between the Railway Track Recording Vehicle Underbody, and Ballast Track Bed

Master Thesis

2021

Ing J. Reimerink

R-2072-A

Study of the Airflow between the Railway Track Recording Vehicle Underbody, and Ballast Track Bed

Master Thesis

2021

July 2021

Ing J. Reimerink

TO MY FAMILY

Eindhoven, the Netherlands;
Amersfoort, the Netherlands;
The Hague, the Netherlands,
July 2021

This work is supported by

Eindhoven University of Technology,
Groene Loper 3, 5612 AE, Eindhoven, the Netherlands

and

Eurailscout Inspection and Analysis,
Berkenweg 11, 3818 LA, Amersfoort, the Netherlands.

J. Reimerink
Study of the Airflow between the Railway Track Recording Vehicle Underbody,
and Ballast Track Bed
July 2021

Copyright © 2021 by J. Reimerink,
Copyright © 2021 EURAILSCOUT.
All rights reserved. No part of the material protected by this copyright notice may be reproduced or utilized in any form or by any means, electronic or mechanical, including photocopying, recording or by any information storage and retrieval system, without the prior written permission from the author.

Printed in Amsterdam, the Netherlands.

Study of the Airflow between the Railway Track Recording Vehicle Underbody, and Ballast Track Bed

Master Thesis

A thesis submitted in fulfilment of the requirements
for the degree of Master of Science

Supervised by

Prof Dr H. J. H Clercx
and
Dr Ir J. C. H. Zeegers

The defence takes place on:
20 July 2021 at 10:00

by

Jeroen Reimerink

Graduation Commission

Supervisor (Chair): **Prof Dr H. J. H. Clercx**

Supervisor: **Dr Ir J. H. C. Zeegers**

Other members: **Dr Ir L. P. J. Kamp**

Dr Ir T. A. J. van Hooff

Advisors: **Ir M. J. W. Sunter**

Abstract

A common way of performing railway infrastructure inspections is with track recording vehicles equipped with optical measurement systems. By measuring track parameters such as the rail profile, for instance, infrastructure managers or maintenance contractors can evaluate rail wear to guarantee the quality and safety of the infrastructure. However, operational movement of these vehicles generates a flow of air between the car underbody and the railway track. This underbody flow is a matter of concern since airflow near the sensor units brings dirt and water droplets, which accumulate on the rail profile measuring system. This accumulation can block the view of the cameras and laser sensors and leads to inaccurate or missing measurement data.

The goal of this study is to investigate the general flow under the inspection vehicle, find its main influential parameters, and describe the flow near the optical sensors. An additional aim is to provide recommendations for a next-phase project to investigate the effect of geometric modifications on the pollution of the optical sensors.

In this study, the underbody flow of a specific inspection vehicle (SIM) is described with the help of computational fluid dynamics (CFD) simulations by using the commercial software COMSOL. A κ-ε Reynold-average Navier-Stokes (RANS) turbulence model and a simplified geometric model of the SIM and a locomotive are used to calculate the airflow around and underneath the vehicle. The CFD model is qualitatively validated by a wind tunnel test with a 1:18 scale model using smoke visualisation techniques. After the validation, full-scale numeric simulations are performed and different complexities are added individually: relative motion between train and ground, the consideration of ballast and sleepers, and the rotation of the axels and wheels.

Both the wind tunnel test and the CFD simulations indicate a highly turbulent flow and a low-pressure area under the complex bottom surface of the SIM which allows water droplets and dirt to easily enter the bogie area of the SIM. An evaluation near the sensor units under the SIM reveals an unsteady and irregular flow in the bogie area with high vorticity, resulting in high energy dissipation, which is reinforced by the rotating wheels and the relative motion between SIM and ground. Moreover, the relatively high airflow speed between both sensor units causes swirls directly under it, and small dust and water particles can accumulate on the sensor boxes.

Because the flow is highly unstable, it is hardly possible to fully eliminate dirt and water droplets, but a longer-term solution could be mounting a windshield in front of the vehicle which push the flow directly to the sides, resulting in a lower flux of air under the vehicle. In addition, filling the gap between the sensor boxes can reduce high air flow and the energy dissipation locally and prevent airflow coming in the area under the sensor box. A study into these geometric modifications and its effect on the trajectories of particles and droplets is recommended.

Keywords*:* *Railway track inspection, train aerodynamics, train underbody flow, bogie area flow, CFD simulation, κ-ε turbulence model, wind tunnel visualisation.*

Preface

I encountered several setbacks before I started this graduation project, but I am very glad to say that the dissertation “Study of the Airflow between the Railway Track Recording Vehicle Underbody, and Ballast Track Bed” is finally before you. It has been written to fulfil the graduation requirements of the master programme of applied physics at the Eindhoven University of Technology.

This project was undertaken on request of the company Eurailscout Inspection & Analysis B.V., a subsidiary of the Dutch company Strukton Rail and the French company SNCF. A combination of theoretical, numerical, experimental, and organisational aspects made this project a multidisciplinary challenge, which also made it interesting, instructive, and fun to execute.

Developing the thesis statement of this research study was a challenge. The variety of (potentially) influencing aspects, its uniqueness, and the pool of comparable studies made it a complex thesis case. The key to successfully fulfilling this project was to find the relative contributions of each aspect, put them in perspective, and focus on the most important ones.

In general, I feel it is a privilege to live in a country that facilitate the possibility to follow a course of study at a university. Moreover, I completed this project with the help of many people, some of whom I would like to give a special thanks.

From the Eindhoven University of Technology, I would like to thank my supervisor, Prof Dr H. J. H. Clercx (Herman), for his professional guidance during this graduation period. His pragmatic and constructive advice helped me to keep focussed on the main aspects of the project. I also wish to thank Dr Ir J. C. H Zeegers (Jos) for his support and advice. A combination of his critical eye, theoretical knowledge, hard work, and feeling for the practical part of work, especially during the wind tunnel experiment, was part of this achievement. I also want to thank G. W. J. M. Oerlemans (Gerald) for his support in helping to set up the wind tunnel experiment. Gerald was the most constant factor during this difficult part of the project. In addition, I want to thank J. M. van der Veen (Jørgen) for his support with the optical part of the wind tunnel experiment. Lastly, I want to thank Dr Ir L. P. J. Kamp (Leon) for providing me with the software and computational hardware assets to perform the numerical work.

In general, I want to thank the company Eurailscout Inspection & Analysis for giving me the opportunity to perform this graduation project and financially supporting it. From the company Eurailscout, I want to thank Ir M. J. W. Sunter (Martin) for his support in his role as project client. I also want to thank S. Li MSc (Shaoguang) for his support and advice. His research background brought this thesis to a higher level. Finally, I want to give thanks to Ir S. Beltman (Bas) for the possibilities he gave me to perform this project.

My family deserves a particular note of thanks. I preceded to undertake this project with the confidence my parents gave me, along with their mental support over the last 30 years. Additionally, I want to say a special thanks to my girlfriend, Mr C. Hulsegge (Chantal), for her fantastic support over the last 13 years and her own ambition, which kept us motivated and resulted in a double graduation for the both of us.

Finally, I wish you, the reader, pleasure in reading this report.

Jeroen Reimerink
The Hague,
28 May 2021

Table of Contents

Abstract .... **ix**

Preface .... **xiii**

Table of Contents .... **xvii**

List of Figures .... **xxi**

List of Tables .... **xxv**

List of Symbols .... **xxvii**

List of Acronymns/Abbreviations .... **xxix**

1 Introduction **1**

- 1.1 Background 2
  - 1.1.1 Railway Inspection 3
  - 1.1.2 The Switch Inspection Vehicle 4
  - 1.1.3 Rail Profile Measurement System 6
- 1.2 Problem Statement and Hypothesis 7
- 1.3 Research Goal 9
- 1.4 Research Plan 10
- 1.5 Thesis Outline 13

2 Literature Review **15**

- 2.1 Introduction 15
- 2.2 Previous Studies 16

2.3 Underbody Flow 17
2.3.1 Analytical Description 18
2.3.2 Influence of Track 19
2.3.3 Influence of Vehicle 20
2.4 Particle Movement 21
2.5 Train Modifications 22
2.6 Conclusion 23
3 Setup of the Numerical Flow Simulation 25
3.1 Choosing the CFD Model 26
3.2 The κ-ε Turbulence Model and Wall Functions 27
3.2.1 Reynolds-Average Navier-Stokes Model 27
3.2.2 Mathematical Description 28
3.2.3 Analytical Wall Functions 30
3.3 Geometric Setup 30
3.4 Model Setting 33
3.5 Meshing and Computing 34
3.6 Mesh Analysis 36
4 Validation by Wind Tunnel Test 39
4.1 Important Experimental Decisions 39
4.2 Geometric Setup 41
4.3 Validation of Wind Tunnel Setup 46
4.4 Experimental and Numerical Configurations 47
4.5 Experimental Results and Validation 49
4.5.1 Results in the FDD 49
4.5.2 Results in the BDD 52
4.6 Conclusion 55
5 Configuration Analysis and Numerical Results 57
5.1 Configuration Setup 58
5.2 Influence of the Different Configurations 60
5.2.1 Effect on Velocity 60
5.2.2 Effect on Pressure 61
5.2.3 Effect on Vorticity 62
5.2.4 Conclusions of Configuration Analysis 64

5.3 General Flow Characteristics ... 65
5.4 Streamline Analysis ... 67
5.5 Flow Near the Sensor Units ... 69
5.5.1 Vorticity Field Near the Sensor Units ... 69
5.5.2 Velocity Field Near Sensor Units ... 70
6 Conclusions and Recommendations ... 73
6.1 Conclusions ... 74
6.2 Recommendations ... 75
References ... 77
Summary ... 83

List of Figures

Figure 1: Examples of railhead degradation. A: Fracture near bolt hole of the welding plate, B: railhead surface fracture, C: surface squats at rail contact area, D: exfoliation of railhead. **2**

Figure 2: Photograph of the SIM connected with a locomotive of the company Strukton Rail. **4**

Figure 3: Schematic drawing of the SIM and the sensor boxes underneath the vehicle. A: Side view, B: bottom view. **5**

Figure 4: Schematic rear view of the SIM and the sensor units of the RPMS, including A: the visualisation of the coverage of the sensor units, B: bottom view, C: side view, and D: bottom-side view of the sensor units. **6**

Figure 5: A: Photograph of the polluted sensor unit taken from under the SIM. B: Profile density plots of two-dimensional profiles. In this figure, the profiles measured over 20 m are plotted on top of each other in the coordinate system of the left box of the SIM12 measurement system. The red dots around the profile indicate that there was dust and/or water droplets between the sensor unit and the railhead, at the time of measurement. The chaotic lines near the upper surface of the railhead foot are the detection of vegetation. **7**

Figure 6: Cause-and-effect diagram visualising the relationship between the incorrect measurement data and the fouling of the sensor unit. **7**

Figure 7: The solution approach consists of five intermediate steps, from understanding the flow behaviour to the implementation of the geometric modification. **9**

Figure 8: Visualisation of the research plan. Here, the numerical model is based on the real situation, and study results from literature provide extra input to the numerical model. The results of the numerical model are compared with the experimental results. **12**

Figure 9: Upper-side view and underside view of the simplified geometry of the SIM. A: Upper-side view of the SIM, B: underside view of the SIM, C: upper-side view of SIM and locomotive in connected position, D: underside view of SIM and locomotive in connected position. **30**

Figure 10: Geometric setup of the computational domain. A: Side view, B: front view, C: rear view. **32**

Figure 11: Geometric side and bottom view of the SIM with different mesh sizes. A: Extra-coarse mesh, B: coarse-size mesh, C: normal mesh, D: fine mesh. **35**

Figure 12: Visualisation of dimensionless pressure and dimensionless velocity of the four different mesh sizes plotted against the dimensionless length of both vehicles in the longitudinal direction. A: Dimensionless pressure in the forward driving direction, B: dimensionless pressure in the backward driving direction, C: dimensionless velocity in the forward driving direction, D: dimensionless velocity in the backward driving direction. **37**

Figure 13: Photographs of the wind tunnel at the Eindhoven University of Technology in the Netherlands. **41**

Figure 14: Example of raw printed material Standard Bleu X10. .... **42**

Figure 15: Photographs of the scale models. A: Side view of the locomotive, B: side view of the SIM, C: bottom view of the locomotive, D: bottom view of the SIM. **43**

Figure 16: Geometric setup of the wind tunnel experiment. A: Longitudinal inside view in the opposite direction of the flow field, B: longitudinal inside view in downstream direction flow field, C: photograph of the smoke generator, D: Photograph of the nozzle outlet of the smoke injector. **45**

Figure 17: Photograph of the geometric and optic setup of the wind tunnel experiment taken from the semi-open side of the wind tunnel **39**

Figure 18: Results of the cylinder flow experiment with a flow speed of ~0.5 m/s and a cylinder diameter of 150 mm. **46**

Figure 19: Simulation setup, which is comparable to the geometric setup in the wind tunnel to validate both results against each other. A: Side view of the numerical set-up, B: rear-view of the numerical set-up, C: front view of the numerical set-up. **48**

Figure 20: Side view of the experimental and numeric results in the FDD. A: Experimental result of configuration 1, B: numeric result of configuration 1, C: experimental results of configuration 2, D: numeric result of configuration 2. .... **50**

Figure 21: Upper view of the experimental and numeric results in the FDD. A: Experimental result of configuration 2, B: numeric result of configuration 2. .... **51**

Figure 22: Side view of the experimental and numeric results in the BDD. A: Experimental result of configuration 3, B: numeric result of configuration 3, C: experimental result of configuration 4, D: numeric result of configuration 4. .... **53**

Figure 23: Upper view of the experimental and numeric results in the FDD. A: Experimental result of configuration 4, B: numeric result of configuration 4. .... **54**

Figure 24: Relative velocity, pressure, and vorticity at TOR in relative longitudinal direction for four configurations and two driving directions. A: Relative velocity in the FDD, B: relative velocity in the BDD, C: relative pressure in the FDD, D: relative pressure in the BDD, E: relative vorticity in the FDD, F: relative vorticity in the BDD. **61**

Figure 25: Visualisation of vorticity of the underbody region of the SIM moving in the forward direction. A: Basis configuration, B: ground roughness configuration, C: moving ground configuration, D: rotating wheels boundary condition. In the backward direction, E: basis configuration, F: ground roughness configuration, G: moving ground configuration, H: rotating wheels boundary condition. **63**

Figure 26: Side view of 3-D vorticity plot (> 10 1/s). A: FDD (to the left), B: BDD (to the right). **66**

Figure 27: Bottom view 3-D vorticity plot (> 20 1/s). A: FDD (to the left), B: BDD (to the right). **67**

Figure 28: Visualisation of 500 streamlines passing the bottom of the sensor unit in A: the FDD and B: the BDD. **68**

Figure 29: A 2-D visualisation of the vorticity just under the sensor units in A: the FDD and B: the BDD. **69**

Figure 30: A 2-D visualisation of the velocity magnitude and direction field just below the sensor units A: in the FDD and B: in the BDD. **70**

List of Tables

Table 1: Process of understanding, describing, and validating the flow behaviour at the underbody of the vehicle....................**12**
Table 2: Experimental determined values of the model constant of the κ-ε turbulence model (CFD Module User's Guide, 2018) **29**
Table 3: Geometry statistics of the geometric setup **32**
Table 4: List of configured model values....................**34**
Table 5: Calculation details of the simulations of the pushed orientation (FDD) with the four different mesh size performed on HP Desktop (128GB RAM) with two Intel(R) Xenon(R) 3.10 GHz processors (64 cores) with Windows 10 Enterprise 2016 (64 bit) as the operation system **36**
Table 6: Calculation details of the simulations of the pulled orientation (BDD) with the four different mesh size performed on HP Desktop (128GB RAM) with two Intel(R) Xenon(R) 3.10 GHz processors (64 cores) with Windows 10 Enterprise 2016 (64 bit) as the operation system **36**
Table 7: Geometric details of the SIM (original and scaled) compared to the sizes of the wind tunnel....................**42**
Table 8: Dimension specifications of the components used in the experimental setup **43**
Table 9: Overview of the four different experimental configurations **47**

Table 10: Calculation details of the additional numerical setup of both the pushed orientation (FDD) and the pulled orientation (BDD) performed on HP Desktop (128GB RAM) with two Intel(R) Xenon(R) 3.10 GHz processors (64 cores) with Windows 10 Enterprise 2016 (64 bit) as the operation system **..49**

Table 11: Overview of the four different simulation configurations, wherein the simulation of the track, the rotating wheels, and the relative motion of the ground are individually added to each configuration.**..58**

Table 12: Mesh and calculation statistics of the four different numerical configurations in the pushed orientation (FDD) performed on HP Desktop (128GB RAM) with two Intel(R) Xenon(R) 3.10 GHz processors (64 cores) with Windows 10 Enterprise 2016 (64 bit) as the operation system **59**

Table 13: Mesh and calculation statistics of the four different numerical configurations in the pulled orientation (BDD) performed on HP Desktop (128GB RAM) with two Intel(R) Xenon(R) 3.10 GHz processors (64 cores) with Windows 10 Enterprise 2016 (64 bit) as the operation system **59**

Table 14: Overview of the combined configuration of the moving ground and rotating wheels **65**

Table 15: Simulation statistics of the combined RWC and MGC for both driving directions performed on HP Desktop (128GB RAM) with two Intel(R) Xenon(R) 3.10 GHz processors (64 cores) with Windows 10 Enterprise 2016 (64 bit) as the operation system **65**

List of Symbols

x	Longitudinal coordinate	$[m]$
y	Lateral coordinate	$[m]$
z	Height coordinate	$[m]$
$\mathbf{v}$	Velocity vector	$[ms^{-1}]$
L_D	Length of fluid domain	$[m]$
W_D	Width of fluid domain	$[m]$
H_D	Height of fluid domain	$[m]$
$\mathrm{h_g}$	Underbody gap height	$[m]$
V	Speed	$[m]$
u	Velocity x-component	$[\mathrm{ms}^{-1}]$
v	Velocity y-component	$[\mathrm{ms}^{-1}]$
w	Velocity z-component	$[\mathrm{ms}^{-1}]$
ρ	Density	$[\mathrm{kgm}^{-3}]$
μ	Dynamic viscosity	$[\mathrm{kgm}^{-1}\mathrm{s}^{-1}]$
ν	Kinematic viscosity	$[m^2s^{-1}]$
z_0	Surface roughness	$[m]$
u^*	Friction velocity	$[ms^{-1}]$
p	Pressure	$[kgm^{-1}s^{-2}]$
t	Time	$[s]$
$\mathbf{F}$	Force vector	$[kgms^{-2}]$
F_i'	Fluctuation term of force vector component	$[kgms^{-2}]$
u_i'	Fluctuation term of velocity vector component	$[ms^{-1}]$
κ	Kinetic energy per unit mass	$[m^2s^{-2}]$

List of Acronymns/Abbreviations

BC	Basis configuration
BDD	Backward driving direction
BSC	Ballast and sleeper configuration
CFD	Computational fluid dynamics
COMSOL	COMSOL multiphysics
DB	Deutsche Bahn Aktiengesellschaft
DNS	Direct numerical simulations
EU	European Union
Eurailscout	Eurailscout Inspection and Analysis B.V.
FDD	Forward driving direction
IMU	Inertial measurement unit
LDA	Laser Doppler anemometry
LES	Large eddy simulation
LHS	Left-hand side
MGC	Moving ground configuration
PIV	Particle image velocimetry
RANS	Reynolds-averaged Navier-Stokes
RHS	Right-hand side
RPMS	Rail profile measurement system
RWC	Rotating wheels configuration
SIM	Switch inspection and measurement
SNCF	Société nationale des chemins de fer français
TOR	Top of rail
UFM	Universal Fahrweg Messzug

Chapter 1

Introduction

Rail travel is an increasingly popular means of transport in the Netherlands (Salvenberg, Bakker, Ooststroom, & Anne Anneman, 2007). More than 1.2 billion daily passengers travel by train, and the expectation is that this number will increase by 30 to 40% in the coming years (ProRail, 2021). Therefore, the Dutch government intends to increase the rail transport frequency by 50% for the busiest railway lines by 2028 (Van Velthoven & Van der Meer, 2018).

In addition, the Dutch railway network has the highest track occupation density (i.e. number of passengers per length of track) in the European Union (EU) [Ramaekers, Wit, & Pouwels, 2009]. This means that the track occupation will be even higher in the coming years. The intense use accelerates the railway track degradation and has a negative impact on the reliability and safety of the railway infrastructure (Corshammar, 2005). To guarantee a safe and reliable railway network, inspections and maintenance are of significant importance.

1.1 Background

Track settlement,[1] rail degradation, rail rolling contact fatigue (Figure 1), and catenary[2] wear are amongst the main factors of railway infrastructure degradation (Lyngby, Hoksta, & Vatn, 2008). To maintain the reliability and safety of the railway infrastructure, preventive and corrective maintenance such as rail grinding, milling, tamping,[3] and ballast cleaning should be conducted. Whilst, in the past, maintenance planning and procedures were based on experience, they are currently based more on reliability evaluation and lifecycle cost consideration (Carretero, Pérez, & García-Carballeira, 2003).

With the understanding of railway system degradation, the severity of the degradation and the expected lifespan of individual infrastructure components can be

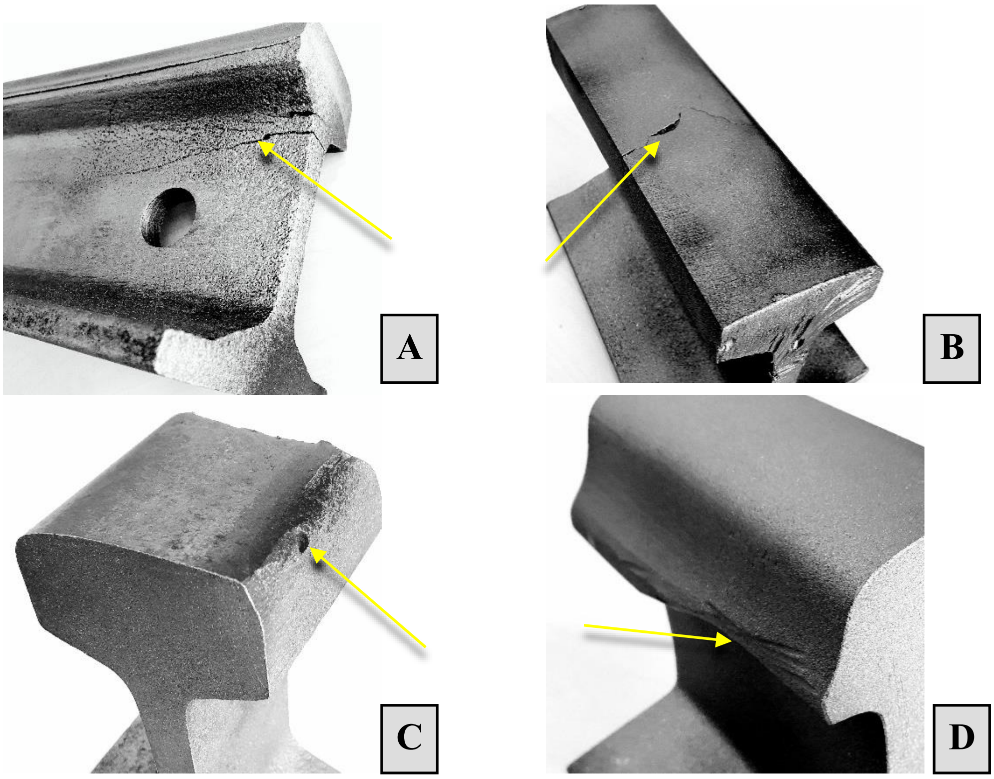

Figure 1: Examples of railhead degradation. **A:** Fracture near bolt hole of the welding plate, **B:** railhead surface fracture, **C:** surface squats at rail contact area, **D:** exfoliation of railhead.

---

[1] Loss of track level and alignment.
[2] Overhead line.
[3] Tamp the track ballast under railway tracks to make the tracks more durable.

estimated and quantified, and maintenance procedures can be optimised. Thereby, the lifespan of the infrastructure components can be prolonged, and in the meantime, the maintenance costs can be reduced.

1.1.1 Railway Inspection

To quantify the infrastructure degradation and the decision for maintenance intervention, regular railway inspections are required. Such inspections can be performed either by human visual observations when inspectors walk along the track or with measurement systems either instrumented with portable equipment or installed on a track recording vehicle (Lyngby, Hoksta, & Vatn, 2008). The drawback of the human visual inspection is that not all defects are visible and, thus, detected. Furthermore, it is less accurate, less reproducible, and susceptible to subjective interpretation.

In contrast, portable measurement equipment can be used to measure several specific railway defects with a high level of accuracy; however, the disadvantages are their low efficiency, which is not suitable for continuous measurement (Lyngby, Hoksta, & Vatn, 2008), and with the light weight and low measurement speed of the system, the measurement cannot reflect the system performance under a dynamic loading condition.

A more efficient method for inspections is performing loaded measurements with track recording vehicles (Lyngby, Hoksta, & Vatn, 2008). Most of these vehicles use laser systems, accelerometers, high-speed cameras, and ultrasonic and eddy current systems to measure infrastructure parameters such as track geometry, rail profile, and rolling contact fatigues (Lyngby, Hoksta, & Vatn, 2008).

Eurailscout Inspection and Analysis B.V. (Eurailscout) is a Dutch railway inspection company which performs railway measurements for companies in Western Europe such as ProRail,[4] SNCF,[5] and Deutsche Bahn.[6] Eurailscout provides multiple inspection solutions, including both hand measurement systems and measurement recording vehicles, to perform a loaded and dynamic measurement of the railway infrastructure. By making use of ultrasonic testing, laser sensors, and high-resolution video recordings, Eurailscout determines infrastructure parameters such as track geometry, catenary wear, and rail geometry with an accuracy in compliance with relevant standards and in a wide measurement speed range.

---

[4] Dutch rail management company.

[5] French rail management company.

[6] German rail management company.

1.1.2 The Switch Inspection Vehicle

Eurailscout has a fleet of measurement vehicles, each built for specific measurement functions. Whereas, for example, the Universal Fahrweg Messzug (UFM) is used to continuously measure the main track at high speed, the switch inspection and measurement (SIM) vehicle measures complex track components such as switches. This makes the SIM ideal for inspections of track structures with many switches (e.g. near large train stations). Moreover, the SIM is a relatively small vehicle which can be transported by truck to other railway tracks in the world, making it a flexible solution to measure switches (Figure 2.1).[7] The SIM was developed and designed by Eurailscout, and a total of six SIMs are part of their fleet. A SIM is not a self-driving vehicle and therefore requires a locomotive to provide the traction (Figure 2.2). The locomotive and SIM are connected at the higher end of the SIM Figure 2.3). Furthermore, the combination of the two vehicles can drive back and forth. The orientation with the SIM as the leading vehicle is called pushed orientation and is the forward driving direction

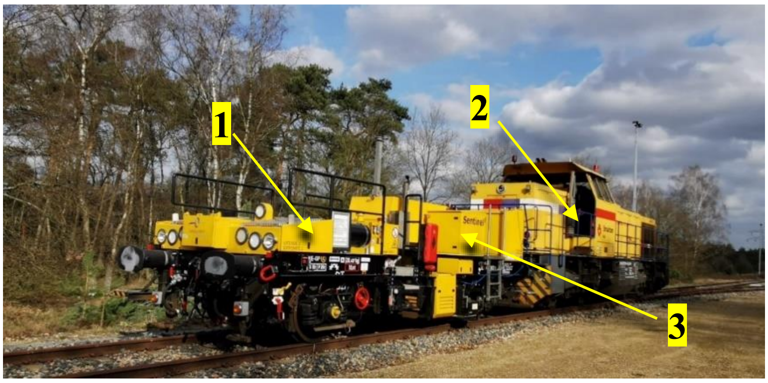

Figure 2: Photograph of the SIM connected with a locomotive of the company Strukton Rail. **1)** SIM vehicle, **2)** locomotive, **3)** rear side and higher end of the SIM.

---

[7] "Figure 2.1" refers to the arrow(s) labeled with number "1" in "Figure 2". This method is used in the rest of this dissertation.

(FDD). This corresponds to driving to the left in Figure 2. The locomotive as the leading vehicle is called the pulled orientation and is the backward driving direction (BDD). This corresponds to driving to the right in Figure 2.

The SIM consists of a single frame (Figure 3) with two axles (Figure 3.6**)**, two buffers on each side (Figure 3.4), and a brake system (Figure 3.5**)**. It also has a video inspection system, including multiple camera units (Figure 3.2) protected by a shielding plate (Figure 3.7), a rail profile measurement system (RPMS) including two laser sensor units (Figure 3.1), and a track geometry measurement system including an inertial measurement unit (IMU). This makes the SIM capable of performing video inspections, track geometry measurements, and in-depth switch inspections in accordance with EN13848-2016.[8] The SIM also has a localisation system which uses a tachometer, a

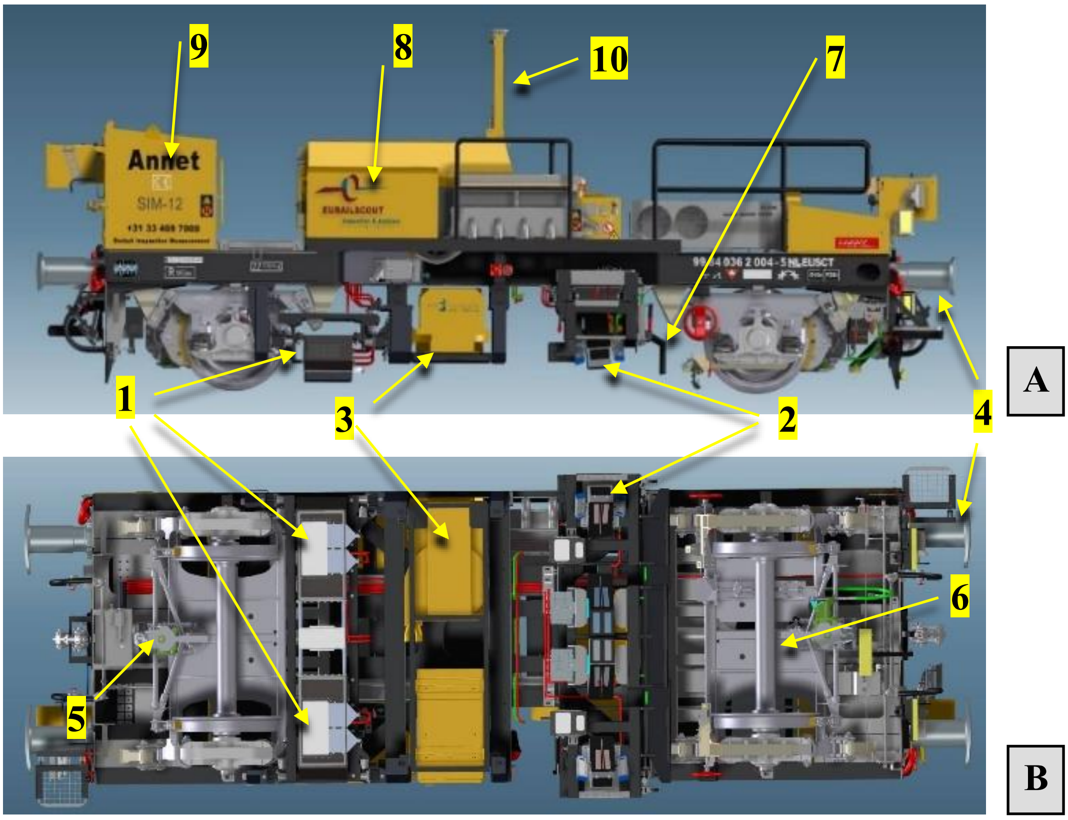

Figure 3: Schematic drawing of the SIM and the sensor boxes underneath the vehicle. **A:** Side view, **B**: bottom view. **1)** Sensor unit of the RPMS, **2)** video measurement system, **3)** air blower system, **4)** buffer, **5)** brake system, **6)** axle, **7)** camera shielding plate, **8)** computer racks, **9)** generator.

---

[8] European norm which describes the minimum requirements for track geometry measuring principles and systems to produce comparable results when measuring the same track.

GPS antenna (Figure 3.10), and the IMU, which makes it possible to generate accurate location information. Data processing and data storage occur in separate computer units mounted in racks at the upper side of the SIM (Figure 3.8). To provide these systems with energy, a generator is installed at the rear side of the SIM (Figure 3.9).

1.1.3 Rail Profile Measurement System

The RPMS consists of two measurement units (i.e. two sensor boxes), which are mounted on each side under the car body of the vehicle, approximately 18 cm above the top of rail (TOR),[9] relatively close to the rear axle (Figure 4A). The wide coverage in the lateral direction (Figure 4.1) makes it possible to perform detailed inspections of the railhead (Figure 4.2) and objects such as the switch blade[10] (Figure 4.3) and frog area.

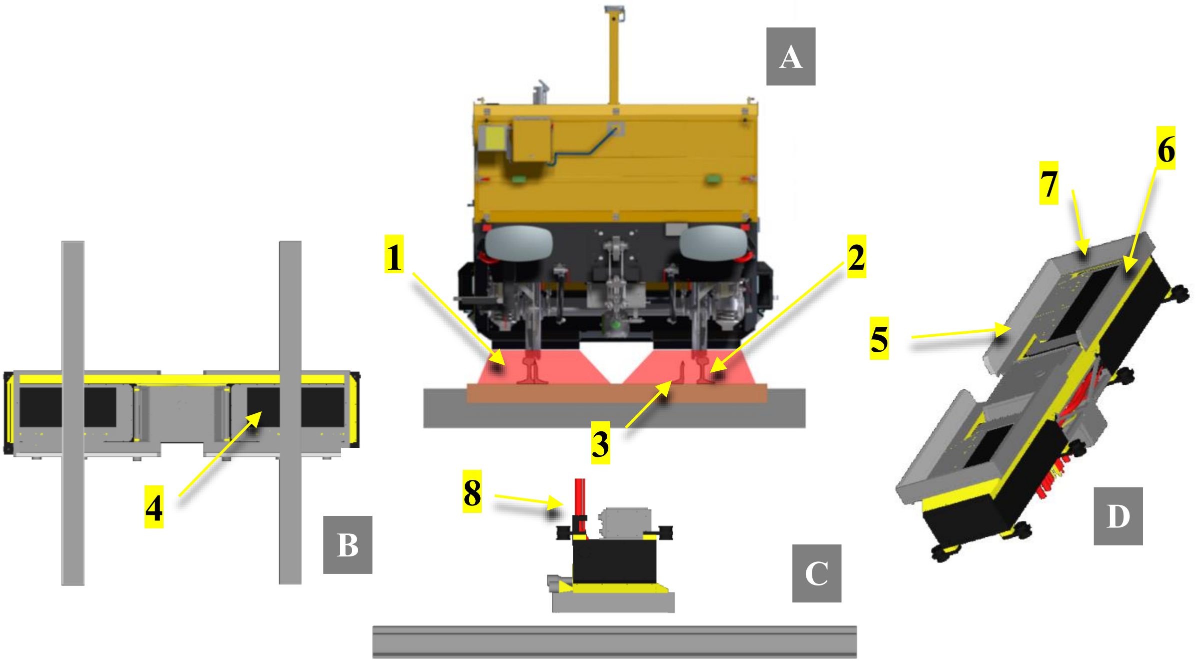

Figure 4: Schematic rear view of the SIM and the sensor units of the RPMS, including **A:** the visualisation of the coverage of the sensor units, **B:** bottom view, **C:** side view, and **D:** bottom-side view of the sensor units. **1)** Left railhead and cover range of the left sensor unit, **2)** railhead, **3)** switch blade, **4)** transparent window, **5)** brushes at leading side, **6)** brushes at trailing side, **7)** brushes at the lateral side, **8)** sensor cables.

---

[9] TOR is the height at the highest point of the railhead, which is normally 180 mm from the ground for a standard railhead.

[10] Part of a switch.

Each sensor unit has four to six cameras and two or three lasers, which cover approximately half of the track bed width. This guarantees that each measurement unit can make a full coverage of the rail profile regardless of the lateral SIM movement. Each camera scans a small section, and by working together, they can make a full 2-D scan of the rail cross-section profile. A minimum sample distance of 20 mm can be guaranteed with a maximum operational speed of 60 km/h during measurement.

The sensor units are closed boxes to protect the sensors from external influences (Figure 3B–D). The five surrounding sides of these two sensor units are made of metal to protect the sensors from mechanical influences and to mount them underneath the SIM, leaving the underside of the sensor units as a transparent window pointing towards the railhead (Figure 4.4), used for the cameras to detect the laser light. Brushes are mounted at the leading (Figure 4.5), trailing (Figure 4.6), and lateral sides (Figure 4.7) of the sensor box to avoid water contamination from the wheels due to a wet railhead and/or rain. Data and power from and to the lasers and cameras are transported by cables, which are connected at the upper side of the sensor unit (Figure 4.8).

1.2 Problem Statement and Hypothesis

Because the RPMS is an optical measurement system, it is very sensitive to obstructions between the sensor unit and the rail track. A common problem is that passing waterdrops, containing dirt and dust, accumulate on the transparent window at the underside of the sensor unit (Figure 6A), resulting in a haze (Figure 5.1). Based on practical experience, this phenomenon is related to the driving direction of the vehicle because accumulation of dirt and water occurs more often when the SIM and locomotive are driving in the BDD than the FDD.

Fouling of the measurement system window has a negative effect on the performance of the measured profiles. The laser reflections can be obstructed, or the field of view of the different cameras can (partially) be blocked. Consequently, the measured rail profiles can become distorted with anomalies or gaps. Figure 6B depicts an example of measured profiles affected by obstruction of the window. Here, the main issue is the gap in the rail profile measurement data (Figure 6.2), which makes it impossible to calculate the correct flangeway clearance and check gauge.

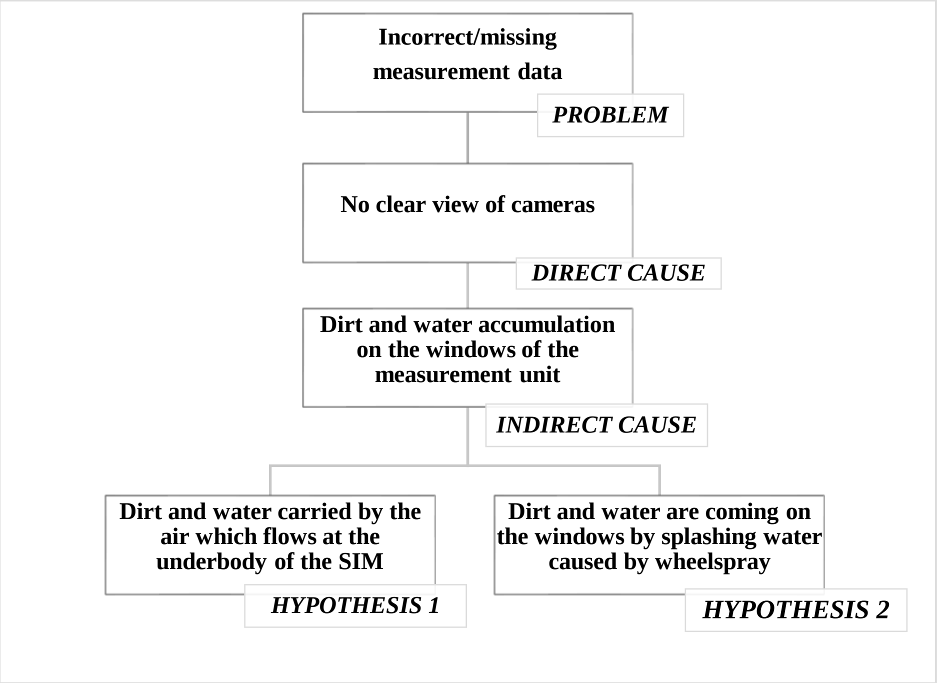
Incorrect/missing measurement data
PROBLEM
No clear view of cameras
DIRECT CAUSE
Dirt and water accumulation on the windows of the measurement unit
INDIRECT CAUSE
Dirt and water carried by the air which flows at the underbody of the SIM
HYPOTHESIS 1
Dirt and water are coming on the windows by splashing water caused by wheelspray
HYPOTHESIS 2

Figure 5: Cause-and-effect diagram visualising the relationship between the incorrect measurement data and the fouling of the sensor unit.

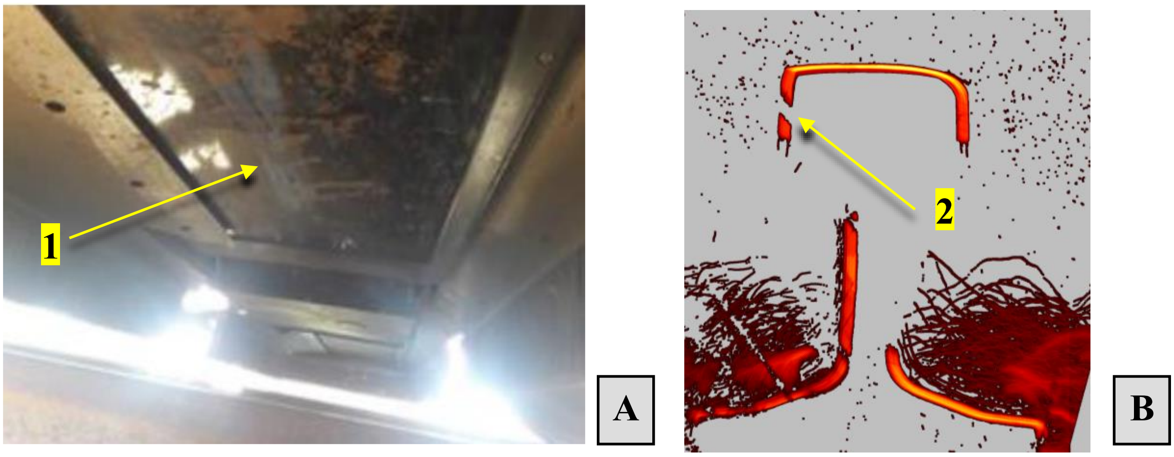

Figure 6: Examples of the problem statement. **A:** Photograph of the polluted sensor unit taken from under the SIM. **B**: Profile density plots of two-dimensional profiles. In this figure, the profiles measured over 20 m are plotted on top of each other in the coordinate system of the left box of the SIM12 measurement system. The red dots around the profile indicate that there was dust and/or water droplets between the sensor unit and the railhead, at the time of measurement. The chaotic lines near the upper surface of the railhead foot are the detection of vegetation. **1)** A haze of brown-coloured pollution is visible on the window of the sensor unit, **2)** a diagonal striation trough the profile as a consequence of partly block view of the cameras.

There are two hypotheses regarding the causes of water and dirt attaching to the windows of the sensor box (Figure 5). The first explanation is that small water droplets contaminated with dirt move with the airflow caused by the movement of the vehicle and hit the glass windows. The second cause is splashing water from rotating wheels when the SIM is passing over a wet railhead.

Since the introduction of an additional layer of brushes between the wheels and the sensor units, it is unlikely that water from the rotating wheels directly reaches the windows, which is endorsed by field observations. Therefore, it is reasonable to conclude that hypothesis 1 is more likely the major cause of the problem. This means that fouling of the sensor windows is caused by indirect transfer and is therefore probably mostly caused by light particles (e.g. a haze of water droplets as a consequence of their lack of inertia, which thereby more easily follow the streamlines of the airflow). For this reason, the focus of this study is on hypothesis 1.

1.3 Research Goal

The long-term goal is to implement an effective geometric modification to the SIM which prevents accumulation of water and dirt on the windows of the RPMS caused by the flow of air induced by the SIM's movement. To realise this modification, five intermediate goals are defined (Figure 7).

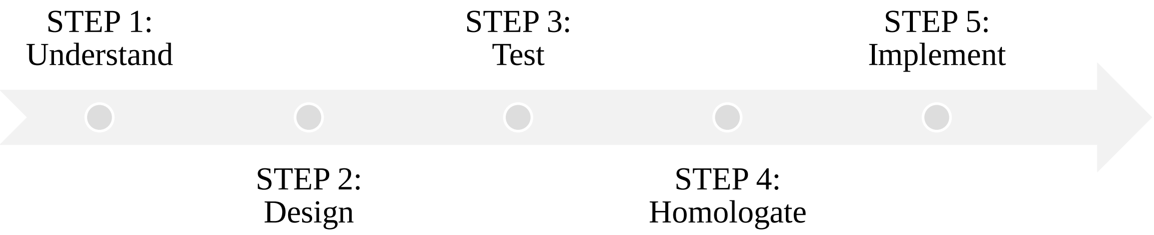

Figure 7: The solution approach consists of five intermediate steps, from understanding the flow behaviour to the implementation of the geometric modification.

First, the current situation must be understood, which means that there must be sufficient knowledge of the flow behaviour under the vehicle and especially around the sensor boxes. Without this, it is unlikely to find an optimal geometric modification. After understanding the flow behaviour, it is possible to design a geometric modification mounting on an effective location of the vehicle (step 2). The third step is to build the modification, mount it to the vehicle, and test the performance. If these tests result in the desired outcomes and have proven its effectiveness, the suggested modification should be validated against the safety requirement of the European and national norms in the form of a request of change (step 4). If it is shown to be a successful homologation, the modification can be implemented and used in operation (step 5).

This study is limited to step 1 (i.e. understanding the flow behaviour). Steps 2–5 will be conducted as a follow-up project and are therefore not the focus of this study. Thus, the research goal herein is formulated as follows:

1) Find the main parameters which influence the flow at the underbody of the SIM.
2) Investigate and describe the flow behaviour close to the underbody of the SIM.
3) Explain why the RPMS is sensitive to water and dirt accumulation.
4) Provide a recommendation as an input for a modification study in a next phase.

1.4 Research Plan

As described in the previous section, the first step is to understand the flow behaviour, but there are multiple approaches to obtain insights into the flow characteristics around and under the SIM (e.g. experimentally and numerically [Baker, 2019]).

An example of an experimental approach is measuring the flow around trains via trackside measurement (on railway track testing), but trackside testing is difficult to perform. For instance, measurement technique, calibration, localisation of measurement data, requirement of instrumentation, and location of measurement are complex aspects of trackside testing. In addition to the complexity, it is expensive, takes a significant amount of time, and requires much organization and many human resources . Moreover, the influence of the atmospheric environment makes reproducibility and data interpretation difficult. On the other hand, the advantage of full-scale testing is that the measurement is based on the real situation without any simplification and assumptions (Baker, 2019).

Instead of trackside testing, an alternative experimental approach is measuring flow in a more controllable environment (e.g. wind tunnels). Because of the disadvantage of full-scale testing, flow measurements are often performed by using wind tunnels with the help of physical (small-scale) models (Baker, 2019). However, simulations of scale models in wind tunnels are simplifications of a more complex actual situation (i.e. it does not cover the entire actual process or necessarily match reality [Baker, 2019]). It is therefore important to give special attention to these discrepancies between models and reality (Baker, 2019).

Another disadvantage of scale models in wind tunnels is the difference in Reynolds number. The relatively small scale and low generated speed in wind tunnels results in a Reynolds number which is lower than it is in the real situation. This can lead to a difference in flow behaviour between the situations, especially on the smaller scale.

An example of a numerical approach is utilising computational fluid dynamics (CFD). CFD has been proven a successful tool to simulate the train aerodynamics and evaluate the influences of geometric changes (García, Crespo, Berasarte, & Goikoetxea, 2011). It is the most common approach in simulating flow around trains and does not depend on experimental resources and related organization. The advantage of CFD is that it presents a full numerical solution of parameters such as velocity and pressure at every point of interest. This makes it possible to directly determine and visualise flow properties (e.g. vorticity or streamlines which pass specific points).

Because of the complexity of this study, and for practical considerations, the latter (a numerical simulation) is employed as the main tool to describe and understand the flow under the SIM. A geometric model of the SIM and a locomotive, together with components of the track infrastructure, is part of the numerical simulation, which is performed in the commercial software COMSOL Multiphysics (COMSOL). To be fully prepared for the simulation, a literature study is presented in advance. Based on knowledge and experience described in the literature, the geometrical components of the vehicles and infrastructure are effectively chosen or simplified. After the numerical simulation, the model is qualitatively validated via a wind tunnel test with 3-D rapid prototyping printed models of both the SIM and locomotive (Figure 8). Finally, after validation of the numerical model, different configurations are simulated with various model conditions. These simulations should provide enough information about the flow characteristics under the SIM to be used as input to design a modification in a next-phase project. These four steps are summarised in Table 1.

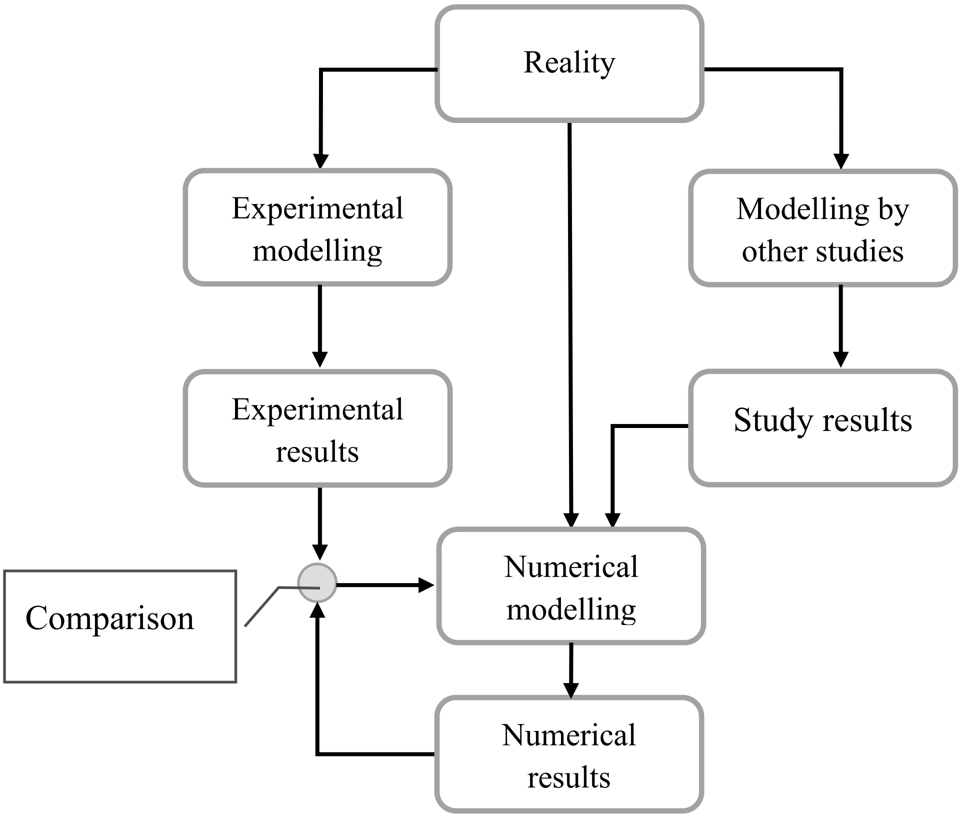
Reality
Experimental modelling
Modelling by other studies
Experimental results
Study results
Comparison
Numerical modelling
Numerical results

Figure 8: Visualisation of the research plan. Here, the numerical model is based on the real situation, and study results from literature provide extra input to the numerical model. The results of the numerical model are compared with the experimental results.

Table 1: Process of understanding, describing, and validating the flow behaviour at the underbody of the vehicle.

Step 1	Literature study
Step 2	Simplified CFD modelling
Step 3	Validation
Step 4	CFD modelling for different scenarios

1.5 Thesis Outline

Chapter 2 of this thesis is a literature review, wherein the general flow characteristics of trains are described, especially at the underbody region. It summarises the influence of the geometry of the train and the infrastructure on flow behaviour based on comparable studies. This insight can be used to effectively make modelling decisions for the numerical simulation. The results from comparable studies can also be used to validate the findings of the numerical simulation and the wind tunnel test.

The simulation setup in the COMSOL environment is described in chapter 3. Its starts with a short description of numerical techniques commonly used for these situations and presents arguments for making certain simulation decisions. It also explains the geometric model of the vehicles, a mathematical description of the numerical flow model, the boundary conditions, the meshing techniques, and the different configurations. Chapter 4 presents the validation of the numerical model in chapter 3, whereby the experimental setup and the results of the wind tunnel test are described, including how this validates the simulation results. The results of the numerical simulation are provided in chapter 5, which begins with a configuration analysis to investigate the influence of different conditions and how these matches the expectations. After the analysis, a more detailed description of the airflow under the SIM and around the sensor box is presented. The last chapter draws the conclusions and recommendation of this study, which can be used for a follow-up project.

Chapter 2

Literature Review

The SIM is designed to perform measurements on the railway infrastructure; thus, it is not a general railway vehicle such as cargo and passenger trains. This makes the aerodynamics knowledge of these vehicles limited. Despite the fact that the SIM special vehicle (is a relatively short, it has a specific geometric shape, and their operational speed is relatively low), it moves on a railway track, and therefore industrial railway aerodynamics is the most related subject to this study. Literature on this topic can help in understanding the general flow under the SIM and in making the right simulation decisions. It can also provide a foundation on which to design a geometric modification to solve the problem related to this study.

2.1 Introduction

A fundamental description of train aerodynamics can be traced back to the beginning of the 20th century (Baker, 2019). In this period, aerodynamics studies were mainly performed with the aim to reduce drag force. Since the 1960s, other aspects of train aerodynamics such as crosswind and tunnel aerodynamics have also increased in popularity amongst researchers. At the end of the 20th century, high-speed trains made their appearance, which resulted in new aerodynamic concerns. In recent years, the operational speed and number of high-speed trains have increased, and therefore train aerodynamics is of growing research interest. Indeed, most currently published studies are related to aerodynamics of high-speed trains.

Flow around trains is, in general, a turbulent flow characterised by chaotic behaviour and high Reynolds numbers (Nieuwstadt, 2016; Baker, 2019). Pressure and velocity are the main parameters of interest in train aerodynamics and depend on the train's geometry, driving speed, and properties of the surrounding air (Baker, 2019). Moreover, flow around trains can be divided into different regions, each with their own characteristics: nose, boundary layer, wake, and underbody region (Baker, 2019).

The underbody region of trains is probably the most valuable subject of train aerodynamics for this study. For a better understanding of the flow under the SIM and the most important parameters, a summary of the most relevant studies is described in this chapter. The subsequent structure of the chapter is organised as follows. Section 2 provides an overview of studies on underbody flows. The third section presents a general description of the characteristics of under-region flow of trains, followed by a more detailed description of the main influential parameters. The fourth section discusses the results from studies on particle movement in the under region. Finally, information is given about geometric modifications implemented in the past to manipulate the flow under the bottom section of the train.

2.2 Previous Studies

Since the fast development of high-speed trains, numerical and experimental studies of the underbody flow are of growing interest for research in the railway industry (García, Crespo, Berasarte, & Goikoetxea, 2011; Quinn et al., 2010; Zhang, Li, Tian, Gao, & Sheridan, 2016). Most studies on underbody flow are related to the problem of flying ballast problem (Soper, et al., 2017), which endangers people near the railway track. It can also cause damage to the infrastructure, the train components beneath the car body (Paz, Suárez, & Cabarcos, 2018), and other infrastructure elements such as the acoustic screens (Soper et al., 2017). One of the main causes of flying ballast is the strong aerodynamic flow in the space between the train and track (Soper et al., 2017). With the increase in operational velocity, especially for high-speed trains, flying ballast is of growing concern (Paz, Suárez, & Cabarcos, 2018; Wang, Zang, Zang, Xie, & Krajnović, 2018).

Other studies on the underbody flow of trains have been performed to achieve traction power reduction for energy saving or noise reduction (Zhang, Wang, Wang, Xiong, & Gao, 2018). In the past, optimising the shape of the nose and tail has been proven an effective method and has been developed to an acceptable level (Baker, 2019; Tian, 2019). Recently, drag force caused by the bogie area[11] is of more interest (Zhang, Wang, Wang, Xiong, & Gao, 2018). For example, there are many studies investigating the effect of bogie cut-out angles[12] on the underbody aerodynamics performance of high-speed trains (Zhang, Wang, Wang, Xiong, & Gao, 2018).

Studies on the underbody region flow have also been performed to reduce the snow and ice accumulation (Kloow, 2011), which can affect safety and traction performance (Gao, Zhang, Xie, Zhang, & Zhang, 2019; Zhang, Wang, Wang, Xiong, & Gao, 2018; Tian, 2019). For example, it can damage the bogie of the train, or suspensions can accumulate with ice and lose their functionality (Kim, Jang, Hong, & Kim, 2015; Giappino, Rocchi, & Schito, 2016). The accumulation of ice also results in an increase of axle load, affecting traction performance and safety (Cao, Huang, & Yin, 2016).

2.3 Underbody Flow

The overall results of numerical calculations, as well as full-scale and scale-model measurements of the underbody flow of trains, show a highly sheared and turbulent flow between the car bottom surface and the ground (Soper, et al., 2017). The flow between the track and the underbody of the train is also highly turbulent, unstable, and complex (García, Crespo, Berasarte, & Goikoetxea, 2011; Zhu, Hu, & Thompson, 2016; Baker C., 2019; Zhang, Wang, Wang, Xiong, & Gao, 2018). The velocities of the airflow under a train are relatively strong, and velocity fluctuations can be of the same order of the velocity of the train (Baker C. , 2019; Cao, Huang, & Yin, 2016; M., Wang, Zhu, & Zhang, 2020).

---

[11] The area around the chassis of a railway vehicle.

[12] Shape of the side car body.

The results of Quinn et al. (2010) have shown that the underbody flow is characterised by an inward flow (to the centre of the track) near the nose and tail of the vehicle and a lateral outward flow in between those regions. Other studies have also proven that the velocity at the nose part is much larger and exhibits more turbulent behaviour and velocity reduction along the length of the train (Zhang, Wang, Wang, Xiong, & Gao, 2018). Additionally, at a certain longitudinal length, the flow begins to stabilise, and fluctuations in the velocity decrease (Baker C. , 2019).

When trains are moving at high speed, the bogie area is under negative pressure (Wang, Zang, Xie, Zhang, & Gao, 2018)**,** (Liu, Wang, Zhu, & Zhang, 2020). The longitudinal pressure profile of the underbody region of the passing train has a well-known profile (Baker C. , 2014) characterised by a high positive spike, followed by a negative spike for the head part of the train (Kwon & Park, 2006), (Ido, Saitou, Nakade, & Likura, 2008)**,** (García, Crespo, Berasarte, & Goikoetxea, 2011)**.** Then the pressure slowly increases and will stabilise around the third coach from where the flow developed (Kwon & Park, 2006)**,** (Ido, Saitou, Nakade, & Likura, 2008), (García, Crespo, Berasarte, & Goikoetxea, 2011).

2.3.1 Analytical Description

An analytical description of the underbody flow of a train is only possible with simplifications. García, Crespo, Berasarte, and Goikoetxea (2011) have studied the underbody flow and developed an analytical solution based on turbulent Couette flow[13] to describe the underbody flow. The solution has been verified by numerical simulations, and both results are in agreement.

The plain Couette flow assumption is based on infinite plates, where the lower plate, representing the ground, is standing still, and the upper plate, representing the bottom surface of the train, is moving with a constant speed V. This is a simplified analytical form of the underbody flow, where the bottom surface of the train, ballast, and sleepers are approximated with an equivalent roughness, and the flow is assumed to be fully developed. The analytical solution of the longitudinal flow component, u, of the velocity as a function of the height, z, from the ground is given by

---

[13] Model of a viscous flow in the space between to separated surfaces where one surface is moving tangentially to the other surface.

$$u(z) = 2.5u^{*}\left[\ln\left(\frac{2h_{\mathrm{g}}}{\pi z_{0gnd}}\sin\left(\frac{\pi z}{2h_{\mathrm{g}}}\right)\right) - \ln\left(\cos\left(\frac{\pi z}{2h_{\mathrm{g}}}\right)\right)\right] \tag{1}$$

where h_{g} is the gap height between the track and the under surface of the train; $\mathrm{z}_{0\mathrm{gnd}}$ is the surface roughness of the ground; and u^{*}, the frictional velocity, is in this case given by

$$u^{*} = \frac{V}{2.5\ln\left(\frac{2h_{\mathrm{g}}}{\pi z_{0gnd}}\right) + \ln\left(\frac{2h_{\mathrm{g}}}{\pi z_{0trn}}\right)} \tag{2}$$

where V is the speed of the train and $\mathrm{z}_{0\mathrm{trn}}$ the equivalent roughness of the under surface of the train. Equation (1) reflects a logarithmic velocity profile (Soper, et al., 2017) between the ground and the bottom surface of the trains, which depends on the roughness of the train and the ground, their height, and the speed of the moving train. Besides the fact that the bottom surface of the SIM has a complex structure and the flow can only be assumed to be developed after a certain length and in reality there is also a transversal velocity component, this analytical model still describes a general behaviour and the parameters of influence.

2.3.2 Influence of Track

The geometry of the track, which mainly consists of ballast and sleepers, is a main factor which influences the underbody flow, especially when it is close to the ground (Kaltenbach, et al., 2008), (Soper, et al., 2017). As mentioned in the previous section, an analytical equivalent roughness model (García, Crespo, Berasarte, & Goikoetxea, 2011) has been developed for ballast and sleepers to account for their influence on the underbody flow. Other researchers have used this model to determine the equivalent roughness of the track bed (Rocchi, Schito, Tomasini, Giappino, & Premoli, 2013). Results from wind tunnel experiments, on-track measurements, and numerical simulation have indicated that the equivalent roughness differs amongst different kinds of tracks, but the overall trend displays an equivalent sand roughness between 4 and 10 mm.

Nonetheless, other studies have resulted in different values (Soper, et al., 2017). According to Soper et al. (2017), the cause of these discrepancies is that there is no physical reason that the flow should have a constant shear stress. However, both Quinn et al. (2010) and Deeg, Jonsson, Kaltenbach, Schober, and Weise (2008) have argued that there are significant lateral variations of the velocity profile under the train, not only in the longitudinal component of the velocity but also in the lateral velocity term, which are not taken into account.

Other researchers have studied the aerodynamic characteristics of the train underbody with a more realistic ballast track (Paz, Suárez, & Cabarcos, 2018), for example, by performing CFD simulations. They simulated different ballast geometries and concluded that for heights larger than 15 cm from the ground, the flow is independent of the geometry of the ballast. The main difference they found is that the flow near the ballast bed is more chaotic with a rough profile compared to one with a flat profile. They also noticed that a small swirl could appear between the ballast and the sleeper.

2.3.3 Influence of Vehicle

The geometry of the underbody of the train has a major influence on the flow behaviour under the train (Zhang, Wang, Wang, Xiong, & Gao, 2018). Major geometry characteristics are the roughness of the under surface, the length of the train, the geometry of the bogie area, and the shape of the bogie side plates (Zhang, Wang, Wang, Xiong, & Gao, 2018; Baker C., 2019; García, Crespo, Berasarte, & Goikoetxea, 2011). As well as relative motion between the track and the bottom surface of the train and the rotation of the wheels (Zhang, Li, Tian, Gao, & Sheridan, 2016).

As stated in section 2.2, the pressure and velocity components will stabilise at a certain longitudinal length under the train. García, Crespo, Berasarte, and Goikoetxea (2011) have proven that the flow stabilises after the third coach. This means that from the rear part to the tail part of the train, the turbulence level has decreased. Nevertheless, this situation only occurs for relatively long trains, and since the SIM is a short vehicle, this does not apply.

In addition, the shape of the bogie cavities influences the flow field as they can increase both the magnitude of the flow and its unsteadiness (Soper, et al., 2017). Furthermore, the shape of the bogie side plates has a major impact on the velocity profile under the train (Zhang, Wang, Wang, Xiong, & Gao, 2018).

2.4 Particle Movement

Although studies on the underbody regions are increasing, research on the movement of water and dirt particles in the bogie area and their accumulation is limited in railway aerodynamics (Liu, Wang, Zhu, & Zhang, 2020). In other fields such as the automotive industry, there is much more knowledge about particle motion at the underbody. However, these cases are not easily comparable because there is a significant difference in flow behaviour, wheel model, and size (Liu, Wang, Zhu, & Zhang, 2020) between trains and cars. Nonetheless, more studies have been performed in the last several decades to describe snow and water movement in the bogie area of trains (Wang, Zang, Zang, Xie, & Krajnović, 2018).

These studies have revealed that particles around a train, such as water droplets, dirt particles, or snow particles, can easily enter the bogie area (Gao, Zhang, Xie, Zhang, & Zhang, 2019) of high-speed trains under influence of the pressure difference between the bogie area and the surroundings, and they can deposit in the bogie area (Liu, Wang, Zhu, & Zhang, 2020), (Kloow, 2011). Particle accumulation in the bogie area occurs most at a lower speed (~200km/h) [Wang, Zhu, & Zhang, 2020]. Such studies have also claimed that accumulation of snow particles in the bogie area decreases significantly with increasing driving velocity. However, experiments were mostly applied to high-speed trains, so there is not much knowledge about particle deposition at relatively low speeds.

Other studies on particle motion have been performed to investigate the influence of water spraying from wheels. These have shown that water droplets from the wheels can accumulate in the bogie area, especially at the train's underbody above the wheels and the front, rear, and side plates of the bogie (Liu, Wang, Zhu, & Zhang, 2020; Wang, Zang, Zang, Xie, & Krajnović, 2018) have also numerically simulated snow moving in the bogie area of a two-bogie train. This study has revealed that the density and particle diameter have a main influence on the accumulation of snow in the bogie area (Wang, Zang, Zang, Xie, & Krajnović, 2018). Higher densities and larger diameters of the snow particles significantly decrease accumulation (Wang, Zang, Zang, Xie, & Krajnović, 2018). In addition, snow accumulation occurs much more at the bottom part of the bogie than on the top part.

2.5 Train Modifications

Multiple solutions have been proposed to avoid accumulation or manipulate the underbody flow, but they were mostly related to modifications of the track (e.g. adding snow shields along the track to reduce the amount of snow on the track [Bettez, 2011] or reducing the ballast height). However, geometric modifications to the train to prevent accumulation of snow or dirt are rarely found in literature (Wang, Zang, Zang, Xie, & Krajnović, 2018).

Other solutions have been developed to reduce high mean velocities and turbulence near the underbody of a train. It has been proven that smoothing the under surface of the vehicle has a positive effect on reducing the turbulence fluctuations at the undercar body (Soper, et al., 2017; Zhang, Wang, Wang, Xiong, & Gao, 2018; Zheng, Zhang, & Zhang, 2011). In addition, fairing the undercar body region as much as possible, especially near the bogie (Soper, et al., 2017)**,** is seen as an effective method to reduce turbulence (Liang & Shu, 2003).

Another successful method is the implementation of a fully closed fairing system of the inter-car gap between train carriages (Huang, Chen, & Jiang, 2012). Niu, Zhou, and Liang (2017) have investigated the influence of the use of obstacle deflectors at the nose of a train. They concluded that this modification greatly affects the flow behaviour underneath the first part of the train. Similarly, Wang, Zang, Zang, Xie, and Krajnović (2018) found a large difference in the flow behaviour and accumulation of snow in the bogie area between a straight bogie cut-out and an inclined bogie cut-out.

2.6 Conclusion

Based on the literature review, the following conclusions in relation to the goal of this study can be made. The airflow at the underbody region of a train is characterised by a highly turbulent, low-pressure, and unpredictable flow. At the nose, the velocity and pressure fluctuations under the train are high, but they reduce and stabilise at a certain length, which is much longer than the length of the SIM and the locomotive. The longitudinal pressure is characterised by a spiky behaviour at the nose, slowly decreases over the length of the vehicle, and spikes again in the tail area. The velocity profile between the bottom surface of a train and the track bed reflects a logarithmic behaviour, with relatively high velocity at the nose region which slowly decreases over the length of the vehicle. Ballast, sleepers, underbody geometry, body side plates, bogie shape, vehicle length, driving speed, the relative motion between train and track and the rotation of the wheels are the main influential parameters.

Because the underbody flow, especially the bogie area, is a low-pressure region, particularly when trains are driving at a high speed, makes particles around the train easily enters the bogie area. Accumulation of these particles in the bogie area is a common issue which depends on the size and density of the particles and the driving speed. These accumulations mostly occur in lower parts of the bogie area. To prevent accumulation in the bogie area, bogie fairing and shielding the nose region of a train have been proven to manipulate the underbody flow and reduce turbulence.

This knowledge gives an insight in the underbody flow of trains and is used to effectively make modelling decisions for the numerical simulation (Chapter 3). In additions, it is also used to validate the findings of the wind tunnel test (Chapter 4) and the results of the numerical simulations (Chapter 5).

Chapter 3

Setup of the Numerical Flow Simulation

Fluids are generally described by the Navier-Stokes equation (NSE), and since the velocity terms are relatively low at ~10m/s (which is the normal operational speed of the SIM), the flow can be assumed to be incompressible. The incompressible version of the NSE is given by

$$\rho\frac{\partial\mathbf{u}}{\partial t}+\rho(\mathbf{u}\cdot\nabla)\mathbf{u}=\nabla\cdot\left[-p\mathbf{I}+\mu\left(\nabla\mathbf{u}+(\nabla\mathbf{u})^{T}\right)\right]+\mathbf{F} \tag{3}$$

$$\nabla\cdot\mathbf{u}=\mathbf{0}$$

where $\mathbf{u}$ is the velocity vector, ρ the density of the air, t the time, p the pressure, μ the dynamic viscosity of the air, and $\mathbf{F}$ the external forces acting on the air.

Analytically solving the NSE is only possible for some very specific situations where the geometry is simple and the Reynolds number is low. Since trains have complex geometries, and the flow around them is highly turbulent (Baker C. , 2019), (García, Crespo, Berasarte, & Goikoetxea, 2011), (Zhu, Hu, & Thompson, 2016), (Zhang, Wang, Wang, Xiong, & Gao, 2018), an analytical approach is not possible. A better approach is to linearise the NSE and then solve it with the help of high-performance computers. This process of solving the flow equation is known as CFD, a valid tool to describe the underbody flow under trains (García, Crespo, Berasarte, & Goikoetxea, 2011).

3.1 Choosing the CFD Model

CFD is based on discretising the computational domain into a finite number of computational cells and then solving the solution for each cell using specific boundary conditions at the interface at each cell. A substantial amount of effort has been spent in developing CFD methods for turbulence calculation for engineering applications (Versteeg & Malalasekera, 2007). These methods can be grouped in three main categories (Versteeg & Malalasekera, 2007):

- Direct numerical simulation (DNS)
- Large eddy simulation (LES)
- Reynolds-averaged Navier-Stokes model (RANS)

DNS is the most direct way of calculating the flow including all turbulent fluctuation components. However, calculating these components requires high-cost computer resources, which makes it inapplicable for industrial use. LES is a more intermediate method which uses space filtering, where large eddies pass, and small eddies are rejected, but this method still requires high computational capacity. The RANS method is based on the mean flow and the average properties of the turbulence flow. Compared to the other methods, this requires fewer computer resources and is therefore widely used in engineering applications (Versteeg & Malalasekera, 2007).

In most CFD studies on the underbody flow of trains, RANS modelling is commonly used (Soper, et al., 2017), (Wang, Zang, Zang, Xie, & Krajnović, 2018), (García, Crespo, Berasarte, & Goikoetxea, 2011). In addition, other models are employed (e.g. the delayed detached eddy [DDS] method, which is a combination of delayed LES and RANS [[Paz, Suárez, & Cabarcos, 2018], and the etached eddy simulation (DES) method based on the κ-ε model [Zhang, Wang, Wang, Xiong, & Gao, 2018]. Some researchers even prefer using time-dependent DES instead of RANS because of the unpredictable flow at the underbody region of the train (Zhang, Wang, Wang, Xiong, & Gao, 2018). In this study, a very detailed description of flow fluctuations is not necessary, and time-average properties are sufficient. Therefore, the RANS model is applied.

Numerical simulations of the underbody flow are mostly performed with the commercial software ANSYS Fluent. To the best of the author's knowledge, none is performed by the software COMSOL.

In the following sections, the numerical simulation setup is described, which includes the geometric structure of the locomotive and the SIM, the κ-ε turbulence model, the wall functions, wall condition, boundary conditions, inlet and outlet of the model, and the mesh.

3.2 The κ-ε Turbulence Model and Wall Functions

The airflow in this numerical setup is described by the κ-ε turbulence model together with analytical wall function. The κ-ε model is a RANS turbulence model and can be derived from the RANS equation. A mathematical description of both the κ-ε turbulence model and the wall function are provided in this section.

3.2.1 Reynolds-Average Navier-Stokes Model

The RANS model is a time average form of the Navier-Stokes equation. The idea is based on Reynolds decomposition, where the different quantities of velocity, pressure, and force are decomposed into an averaged and a fluctuation term, $u_i = U_i + u_i'$, $p = P + p'$ and $f_i = F_i + {f_i}'$. Substituting these quantities in the NSE and ensemble-averaging leads to

$$\rho\frac{\partial \mathbf{U}}{\partial t} + \rho\mathbf{U}\cdot\nabla\mathbf{U} + \nabla\cdot\overline{(\rho\mathbf{u}'\otimes\mathbf{u}')} = -\nabla P + \nabla\cdot\mu(\nabla\mathbf{U} + (\nabla\mathbf{U})^T + \mathbf{F} \qquad (4)$$

$$\nabla\cdot\mathbf{U} = \mathbf{0}$$

which is known as the RANS equation. The fluctuation term $\nabla\cdot\overline{(\rho\mathbf{u}'\otimes\mathbf{u}')}$, in equation (4) appears, which is called the Reynolds stress tensor. When assuming the Reynolds stress is purely diffusive, the term can be expressed as

$$\rho\overline{(\mathbf{u}' \otimes \mathbf{u}')} = \frac{1}{3}\rho\, tr((\mathbf{u}' \otimes \mathbf{u}')\mathbf{I} - \mu_T(\nabla\mathbf{U} + (\nabla\mathbf{U})^T) \tag{5}$$

where μ_T is the turbulent viscosity. The second part of equation 5 can be written in terms of kinetic energy

$$\frac{1}{3}\rho\, tr(\mathbf{u}' \otimes \mathbf{u}')\mathbf{I} = \frac{2}{3}\rho k \tag{6}$$

where k is the turbulent kinetic energy.

3.2.2 Mathematical Description

The κ-ε model is a two-equation turbulent model which focusses on the effect of the turbulent kinetic energy $k(t)$ and the turbulence dissipation rate $\varepsilon(t)$, which are the sum of the mean kinetic energy $\bar{k}$, the mean dissipation rate $\bar{\varepsilon}$, the turbulent kinetic energy k', and the dissipation rate ε', respectively (Versteeg & Malalasekera, 2007). The mean kinetic energy $\bar{k}$ is the kinetic energy per unit mass and is defined as $\bar{k} = \frac{1}{2}(\bar{u}^2 + \bar{v}^2 + \bar{w}^2)$, with $\bar{u}$, $\bar{v}$, and $\bar{w}$ the mean velocity components in the x, y, and z directions, respectively.

The κ-ε model relies on the assumption that the turbulence is in equilibrium in the boundary layer, where production equals dissipation at a high Reynolds number (CFD Module User's Guide, 2018). By utilising the RANS equation (4) and inserting the definitions given by equations (5) and (6), along with some algebra, the turbulent kinetic energy k reads

$$\rho\frac{\partial k}{\partial t} + \rho\mathbf{U}\cdot\nabla k = \nabla\cdot\left(\left(\mu + \frac{\mu_T}{\sigma_k}\right)\nabla k\right) + P_k - \rho\varepsilon \tag{7}$$

were μ_T is the turbulent viscosity. The first term on the left-hand side (LHS) of the equation is the rate of change of the kinetic energy, and the second term on the LHS is the transport of the kinetic energy by convection. The first term on the right-hand side (RHS) is a combination of the pressure, viscous stress, and Reynolds stress. The second term on the RHS is the production term of the kinetic energy, and the last term is the rate of destruction of the kinetic energy.

The production term P_k is given by

$$P_k = \mathrm{\mu_T}\left[\nabla\mathbf{U}:(\nabla\mathbf{U} + (\nabla\mathbf{U})^{\mathrm{T}}) - \frac{2}{3}(\nabla\cdot\mathbf{U})^2\right] - \frac{2}{3}\mathrm{\rho k}\nabla\cdot\mathbf{U} \tag{8}$$

and the transport equation of dissipation ε reads then

$$\mathrm{\rho}\frac{\partial\mathrm{\varepsilon}}{\partial\mathrm{t}} + \mathrm{\rho}\mathbf{u}\cdot\nabla\mathrm{\varepsilon} = \nabla\cdot\left(\left(\mathrm{\mu} + \frac{\mathrm{\mu_T}}{\mathrm{\sigma_\varepsilon}}\right)\nabla\mathrm{\varepsilon}\right) + \mathrm{C_{\varepsilon,1}}\frac{\mathrm{\varepsilon}}{\mathrm{k}}\mathrm{P_k} - \mathrm{C_{\varepsilon,2}}\mathrm{\rho}\frac{\mathrm{\varepsilon}^2}{\mathrm{k}} \tag{9}$$

where the turbulent viscosity $\mathrm{\mu_T}$ is modelled by

$$\mu_T = \rho\mathrm{C_\mu}\frac{k^2}{\varepsilon} \tag{10}$$

where $\mathrm{C_\mu}$ is a specific model constant. The constants $\mathrm{C_\mu}$, $\mathrm{C_{\varepsilon,1}}$, $\mathrm{C_{\varepsilon,2}}$, $\mathrm{\sigma_k}$ and $\mathrm{\sigma_\varepsilon}$ are experimentally determined (Wilcox, 1998). These values are given in Table 2.

Table 2: Experimental determined values of the model constant of the κ-ε turbulence model (CFD Module User's Guide, 2018)

Constant	Value
$\mathrm{C_\mu}$	0.09
$\mathrm{C_{\varepsilon,1}}$	1.44
$\mathrm{C_{\varepsilon,2}}$	1.92
$\mathrm{\sigma_k}$	1.0
$\mathrm{\sigma_\varepsilon}$	1.3

The assumptions made in the κ-ε turbulence model (e.g. the equilibrium between production and dissipation) result in accuracy limitations, especially for flows with adverse pressure gradients (Wilcox, 1998). It also provides an under-prediction of recirculation zones (Wilcox, 1998), and it is in poor agreement with experimental results for rotating flows (Driver & Seegmiller, 1985).

Nevertheless, this RANS approach is commonly used in train aerodynamics application (Soper, et al., 2017), (Wang, Zang, Zang, Xie, & Krajnović, 2018), (García, Crespo, Berasarte, & Goikoetxea, 2011), and therefore equations (7) and (9), together with the definition of equation 8 and the model constant in Table 2, describe the κ-ε model used as a basis in the rest of this document to describe the airflow around the SIM and the locomotive.

3.2.3 Analytical Wall Functions

Due to mesh resolutions, the κ-ε model is not valid when the solution zone is close to a solid wall. It is possible to solve this limitation after manipulation with the κ-ε model, but it requires a very high mesh resolution and correspondingly high levels of computer resources (CFD Module User’s Guide, 2018). In this CFD simulation, wall analytical functions are used to describe the volume between a solid wall and a lift-off distance δ_w from the solid wall. The κ-ε model described in the previous section, together with wall functions, forms the fluid model in this CFD design.

3.3 Geometric Setup

The geometry of the SIM used in this CFD setup is based on the original, fully detailed 3-D drawing. It has been manually simplified, with the help of 3-D drawing software, to a 98% reduction compared to its original size. The simplification is to remove

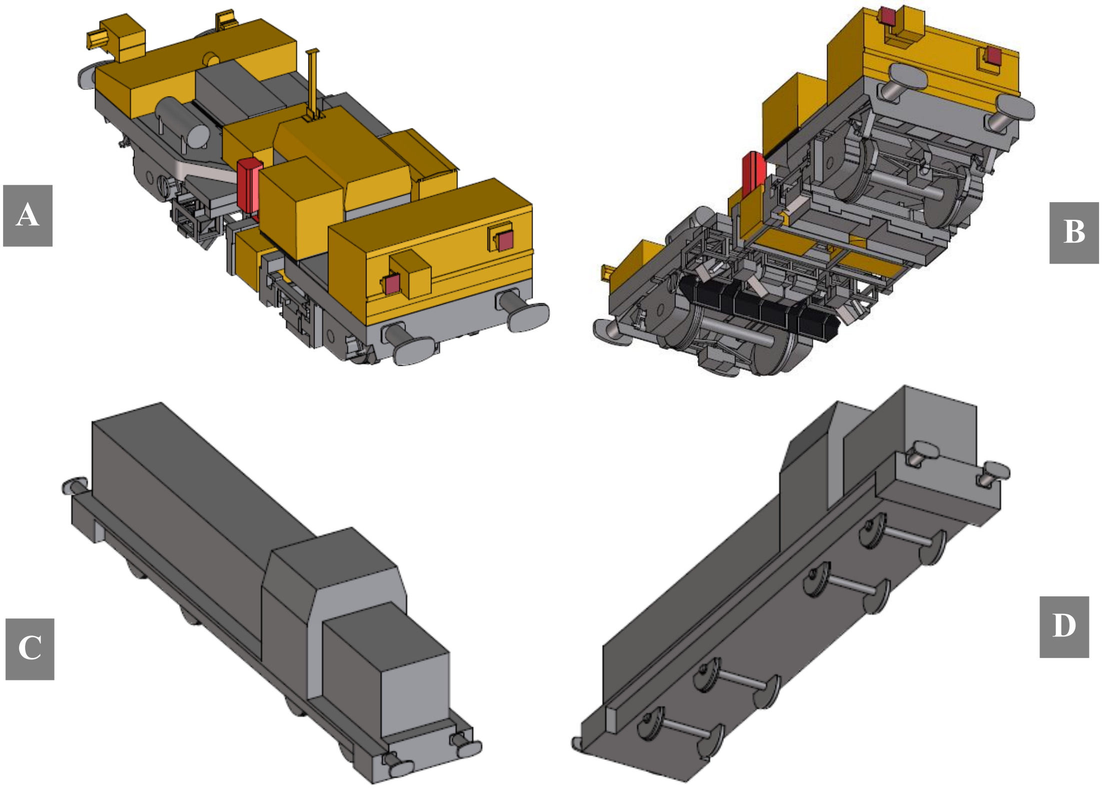

Figure 9 : Upper-side view and underside view of the simplified geometry of the SIM. **A**: Upper-side view of the SIM, B: underside view of the SIM, **C**: upper-side view of SIM and locomotive in connected position, **D**: underside view of SIM and locomotive in connected position.

unnecessary details and irrelevant small size elements (e.g. cables, screws, and other small objects), and complex geometric objects have been combined and transformed into simple shapes, especially at the upper side of the vehicle. Although the reduction rate is high, the general shape of the vehicle was kept intact, which makes it presumably representative of aerodynamic effects (9A–B). For numerical simulations, this geometry is still quite complex to implement in COMSOL compared with other numerical simulations, as mentioned in the previous chapter.

Since this study is focussed on the flow at the underbody of the SIM, a detailed geometry of its connected locomotive is not necessary. Therefore, the geometry of the locomotive is much more simplified than the SIM and consists of a rectangular frame, four cylinder-shaped axles, and eight wheels with a simplified wheel profile (Figure 9C–D).

Both 3-D drawings of the vehicles have been converted to a .step file (COMSOL-recognisable format) to import them as a 3-D object in the COMSOL environment with the CAT Import Module.[14] After importing the model, a geometric check is performed to remove those geometric imperfections which can result in numerical simulation failures. After that, the vehicles of the SIM and locomotive are coupled so they form two connected vehicles.

The infrastructure in the simulation is limited to the left and right rail. The rail is simulated as two long rectangular bars along the whole length of the computational domain with a height of 180 mm and a width of 142 mm, which correspond to the nominal size of the UIC60[15] rail. The inner distance between the two rails is 1435 mm, which corresponds to the rail standard gauge[16] width. The simulation domain is set to L_D=144 m length, which is around six times the length of both vehicles together (Figure 10). The height H_D and width W_D of the fluid domain is set to 16.2 m and 12.6 m, respectively, which are at least five times the size of the vehicle. An overview of all dimensional values is listed in Table 3.

---

[14] The CAD Import Module is an add-on to COMSOL Multiphysics for importing geometries created in CAD software.

[15] UIC60 is the technical term of the nominal rail type in the railway industry in the Netherlands.

[16] Term for the inner distance between the left and right rail.

Table 3: Geometry statistics of the geometric setup

Description	Value	Description	Value
Space dimension	3	Length of vehicle	23.11 m
Total number of boundaries	1708	Width of vehicle	2.58 m
Total number of edges	5205	Length of fluid domain	144 m
Number of vertices	3382	Width of fluid domain	12.60 m
Length of SIM	8.43 m	Height of fluid domain	16.2 m
Length of locomotive	14.68 m	Height of rail	180 mm

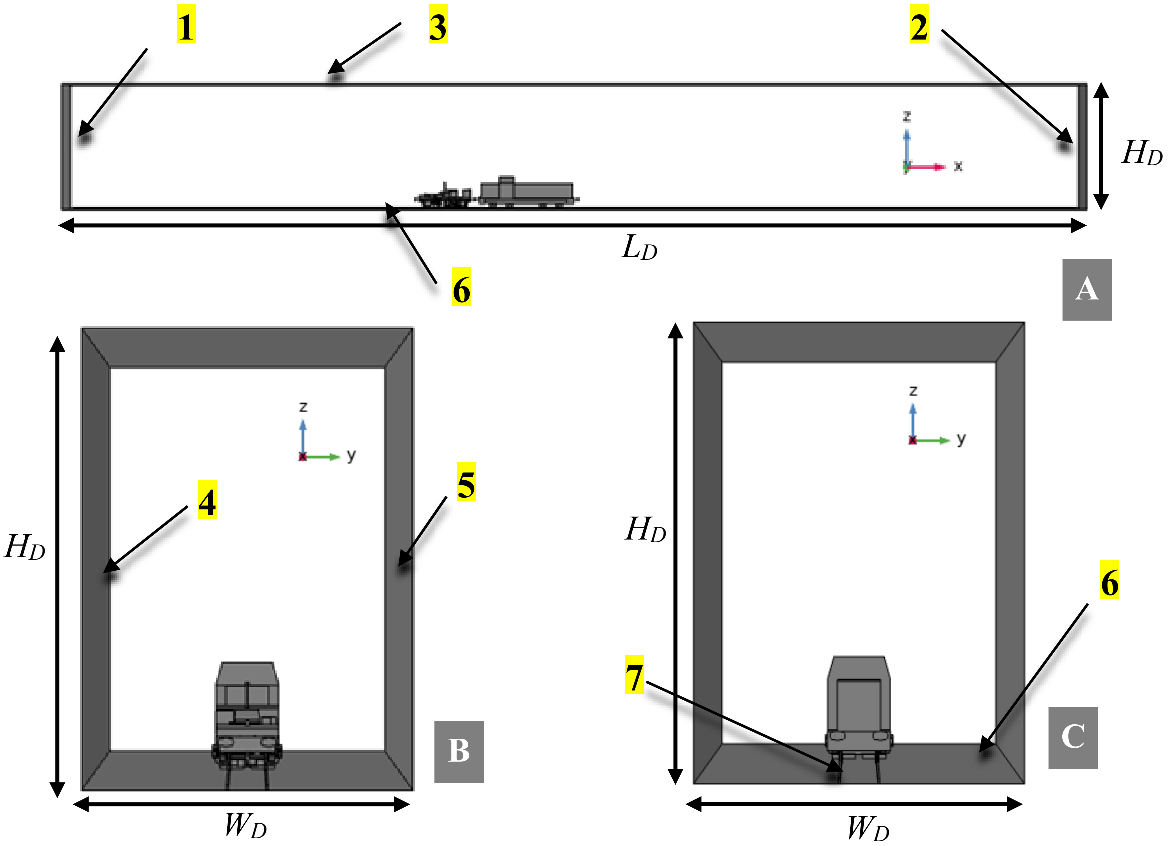

Figure 10: Geometric setup of the computational domain. **A**: Side view, **B**: front view, **C**: rear view. **1)** Flow inlet surface, **2)** flow outlet surface, **3)** upper domain boundary (slip wall), **4)** left domain boundary (slip wall), **5)** right domain boundary (slip wall), **6)** bottom domain boundary (no-slip wall), **7)** rectangular rail (no-slip wall).

The surface on the left (Figure 10.1) is the flow inlet surface, and on the right (Figure 10.2) is the flow outlet surface. The inlet flow is defined as a fully developed flow with a configurable average velocity, which means that there is only a normal velocity component at the inlet surface. The outlet is defined as a pressure outlet, which means that the pressure at the outlet surface is set to be uniform and constant. The upper (Figure 10.3), the left (Figure 10.4), and the right (Figure 10.5) domain boundaries are walls with a slip condition. This means that neither kinetic energy nor fluid can penetrate these walls. The bottom domain boundary (Figure 10.6), rails, and geometry of the vehicles are set to walls with a no-slip condition. At these, no-slip walls act in addition to the nonpenetration conditions, a nonslip condition, which means that the air directly at the wall has the same velocity as the wall.

3.4 Model Setting

To complete the fluid model, several parameters must be configured. The turbulence constants listed in Table 2 are examples of configured parameters and are set to constants based on experimental results from literature. Other parameters are the inlet and outlet conditions of the fluid domain. As stated, the inlet is set to a fully developed flow with an average inlet velocity. The longitudinal inlet velocity component is set to 5 m/s, which is comparable to the operational speed of the SIM and is an optimal speed for the wind tunnel simulation to validate the numerical model. The inlet condition, combined with the side and upper walls and the nonslip floor, results in a fully developed turbulent boundary layer flow. The pressure outlet is set at zero pressure.

Other settings that must be determined are the density and the kinematic viscosity of the air. The density ρ of the air is set to be 1.204318 kg·m^{-3} and the kinematic viscosity υ at 1.5062·10^{-5} m^{2}s^{-1}, which are comparable to air properties at a temperature of 20°C (CFD Module User's Guide, 2018). The model is time independent and external forces, including gravity, are excluded. The initial velocity value of the fluid domain is equally set to the value of the inlet velocity. All of these values are summarised in Table 4.

Table 4: List of configured model values

Description	Value
u_{inlet}	5 m/s
v_{inlet}	0 m/s
w_{inlet}	0 m/s
p_{out}	0 Pa
ρ	1.204318 kg·m^{-3}
μ	1.5162·10^{-5} m^{2}s^{-1}
$u_{initial}$	5 m/s
$v_{initial}$	0 m/s
$w_{initial}$	0 m/s

3.5 Meshing and Computing

Before the numerical model can be solved, the geometric model should be divided into elements called mesh. Herein, there are three different types of meshes. The first one is for the fluid domain, which is a standard mesh in COMSOL specifically designed for fluid properties. The second one is the mesh for the walls (the geometry of the vehicles and the boundaries of the fluid domain). The third is for the volume close to the walls, which is the wall-function area. To verify the quality of the mesh, different mesh sizes have been used to analyse their impacts on the fluid properties: extra coarse, coarse, normal, and fine. The mesh appearance of the SIM with four different mesh sizes is shown in Figure 11.

With the meshed model, the next step is to start the numerical simulation. The calculation is performed in COMSOL Multiphysics version 5.6 together with the CFD module and the CAT Import Module. The simulation software is installed on an HP Desktop (128GB RAM) with two Intel(R) Xenon(R) 3.10 GHz processors (64 cores) with Windows 10 Enterprise 2016 (64 bit) as the operation system. The FDD (pushed orientation) and BDD (pulled orientation) have been calculated. Both configurations are performed with the four different-meshed sizes. In total, there are eight calculations, which converted to a solution for the three velocity components and the pressures.

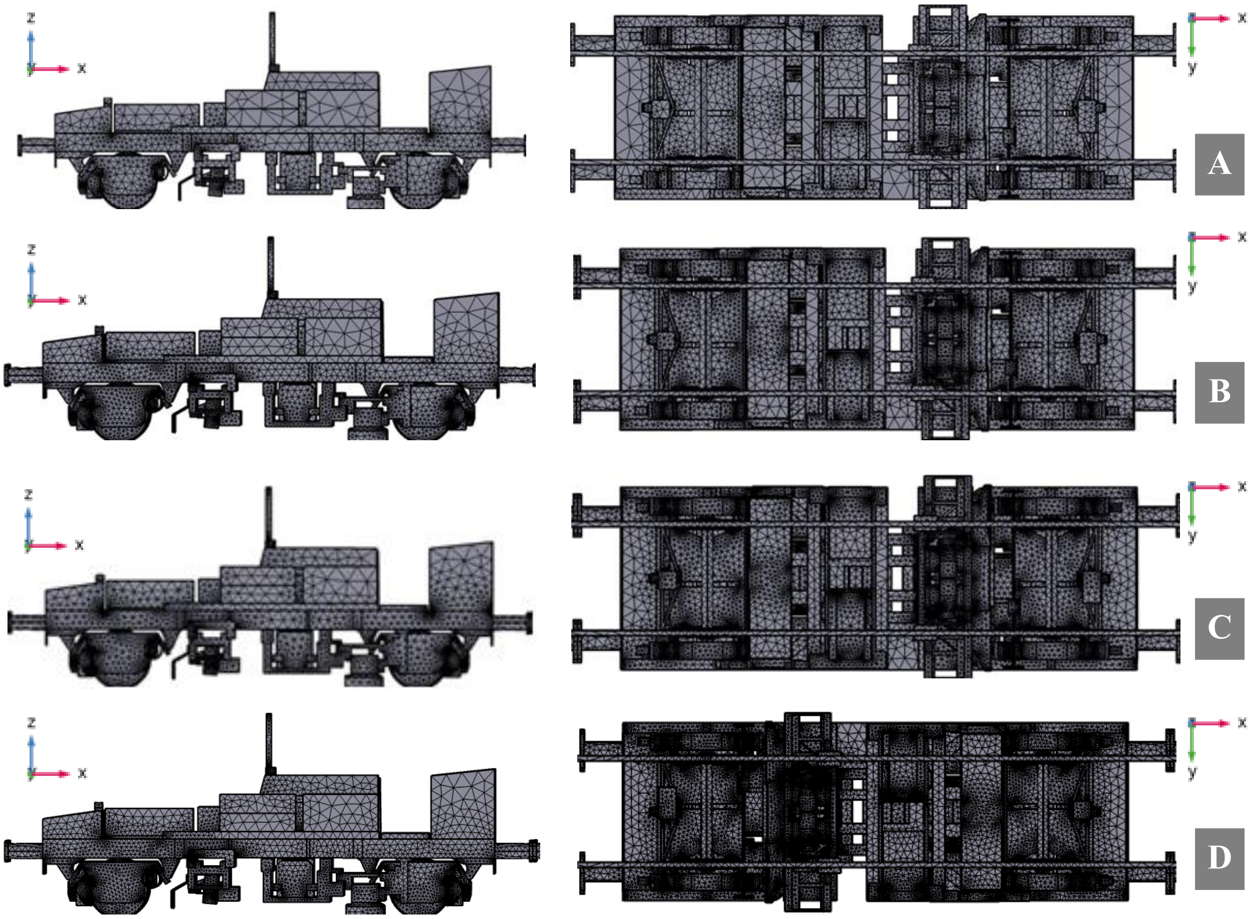

Figure 11: Geometric side and bottom view of the SIM with different mesh sizes. **A**: Extremely coarse mesh, **B**: coarse mesh, **C**: normal mesh, **D**: fine mesh.

Specific details about the number of mesh elements, skewness mesh quality,[17] and calculation time are summarised in Tables 5 and 6.

---

[17] Skewness mesh quality is a quality measure of the generated mesh and has a value between 0 and 1, where 1 represents a perfectly regular element. The skewness is defined as the average of the following quantities: $\min\left(1 - max\left(\frac{\theta_i - \theta_e}{\pi - \theta_e}, \frac{\theta_e - \theta_i}{\theta_e}\right)\right)_i$, where θ is the angle of an edge in a mesh element and θ_e the angle of the corresponding edge in n ideal mesh element.

Table 5: Calculation details of the simulations of the pushed orientation (FDD) with the four different mesh size performed on HP Desktop (128GB RAM) with two Intel(R) Xenon(R) 3.10 GHz processors (64 cores) with Windows 10 Enterprise 2016 (64 bit) as the operation system

Value	Extra coarse	Coarse	Normal	Fine
Number of elements	541,694	1,157,476	2,018,971	3,723,537
Skewness mesh quality	0.5370	0.5876	0.6150	0.6391
Calculation time	00h:44m:10s	01h:37m:47s	02h:52m:50s	09h:17m:46s

Table 6: Calculation details of the simulations of the pulled orientation (BDD) with the four different mesh size performed on HP Desktop (128GB RAM) with two Intel(R) Xenon(R) 3.10 GHz processors (64 cores) with Windows 10 Enterprise 2016 (64 bit) as the operation system

Value	Extra coarse	Coarse	Normal	Fine
Number of elements	548,954	1,159,191	2,028,673	3,728,625
Skewness mesh quality	0.5355	0.5860	0.6154	0.6407
Calculation time	00h:34m:23s	02h:01m:54s	02h:56m:40s	09h:04m:25s

3.6 Mesh Analysis

The results of the eight simulations with the different mesh sizes are visualised in Figure 12. In this figure, the dimensionless pressure and velocity at a virtual line in the middle of the track at TOR[18] height is plotted against the dimensionless lateral length under both the SIM and the locomotive, corresponding to the schematic drawing of the connected vehicles in the plot. Here, Figures 12A and 12B are the dimensionless pressure in FFD and BDD, respectively and Figures 12C and 12D the dimensionless velocity for the FDD and BDD. Each of the four figures displays the results of the different mesh sizes: extra coarse, coarse, normal, and fine, where each increasing mesh size is a roughly doubling of the number of mesh elements.

---

[18] Top of rail is the height at the highest of the railhead, which in this case is 180 mm from the ground.

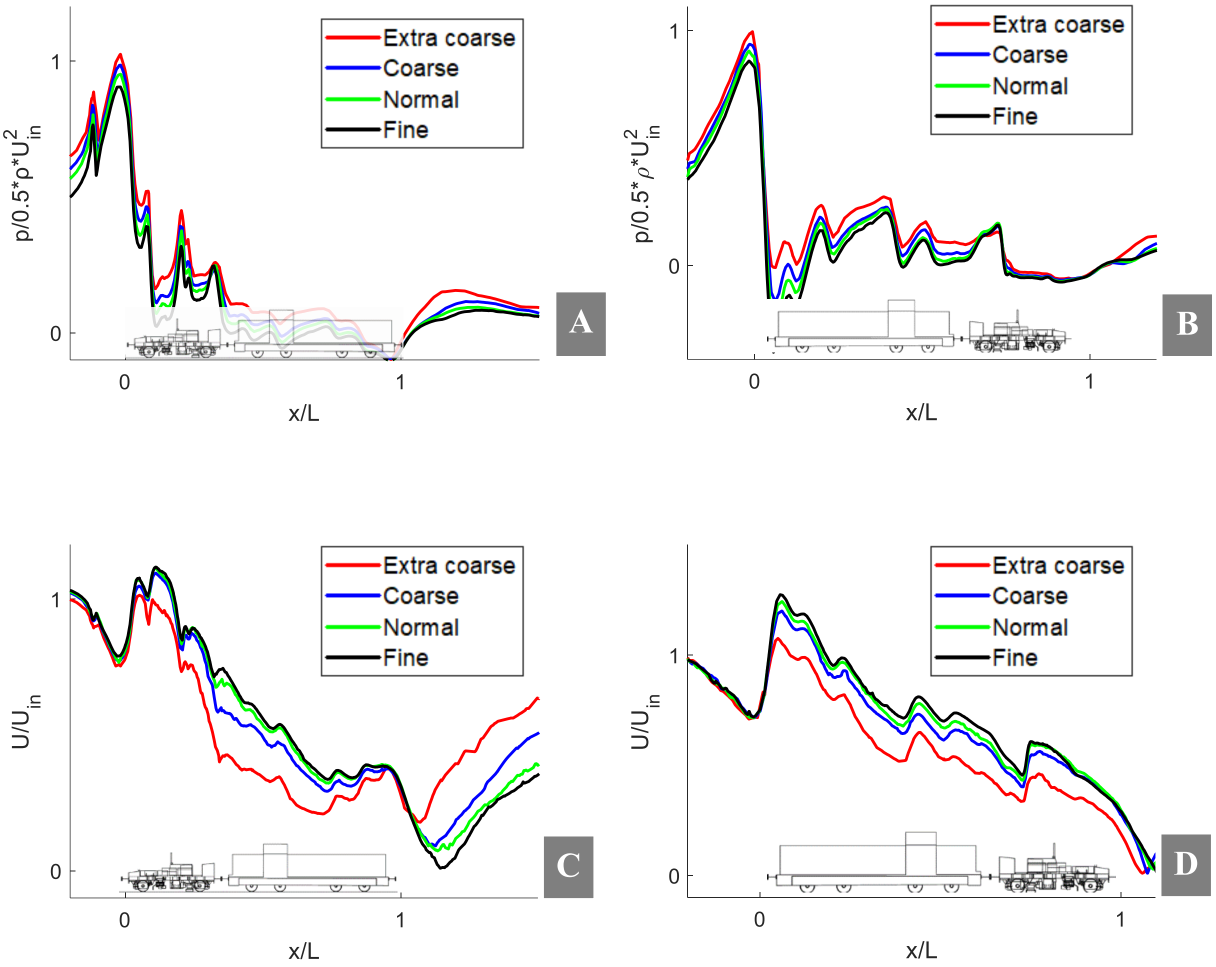

Figure 12: Visualisation of dimensionless pressure and dimensionless velocity of the four different mesh sizes plotted against the dimensionless length of both vehicles in the longitudinal direction. **A**: Dimensionless pressure in the FDD, **B**: dimensionless pressure in the BDD, **C**: dimensionless velocity in the FDD, **D**: dimensionless velocity in the BDD.

These four figures illustrate that the extra course mesh has a relatively large difference to the other mesh sizes, which have smaller differences when increasing the number of mesh elements and seem to converge. Each increasing mesh size seems to halve the difference in velocity and pressure and thereby its computational error. The difference between the normal and fine mesh is relatively small and does not show any discontinuities. Therefore, it can be concluded that fine mesh has enough accuracy for this simulation and provides a good balance between calculation time and mesh accuracy.

Chapter 4

Validation by Wind Tunnel Test

As described in chapter 1, experimental testing in a wind tunnel environment has multiple advantages compared to on-track tests. Therefore, validation of the numerical model via a wind tunnel test with a scale model is a logical step. It should be noted that wind tunnel model measurements, especially with a simplified and scale model, do not reflect the real situation. Discrepancies between model experiments and real scale can be considerable when not making the right decisions in the design of the wind tunnel experiment (Baker C. , 2019).

4.1 Important Experimental Decisions

One of the main decisions in designing a wind tunnel experiment is whether to simulate the relative motion between the train and the ground (Baker C. , 2019). When a static model of a train is used and mounted on a plate, there is no relative motion between the ground and the train. In that case, the underbody flow of the train does not represent the real situation of a moving train. This problem can be solved by making use of a moving belt as a moving ground to simulate the relative movement between the train and the ground. One of the difficulties here is holding the train model in its position just above the belt. A more realistic method is using a moving train model, but this introduces many complexities. It is difficult to generate enough speed, and long track models are needed. Moreover, measuring the flow around a moving train is much more complicated than a non-moving train.

A second specification of design is the generation of the right Reynolds number during the wind tunnel test and its discrepancy with the real situation. A typical value for the Reynolds number in a wind tunnel is in an order of magnitude of ~10^5, where it is around 10^6 in the real situation (Baker C. , 2019). However, in the high Reynolds range, the difference in Reynolds numbers mainly results in a variance in behaviour at very small scale and does not affect the large-scale flow characteristics. According to Baker (2019), wind tunnel tests with Reynolds number $> 2 \cdot 10^5$ (based on train height) are generally assumed to represent the real situation.

A third main aspect in designing a wind tunnel experiment is the limitation of the wind tunnel size. Whereas in the real situation, a train moves in the open air, in a wind tunnel, there is the influence of walls, which generate a boundary layer of airflow and induce blockage in the wind tunnel. Both phenomena influence the airflow in the wind tunnel. However, it is important that the dimensions of the wind tunnel are large enough compared to the size of the geometric model, which results in a negligible influence of the boundary layer and the effect of blockage.

A fourth main decision regards the parameter(s) to measure, the measurement domain, and the best corresponding measurement technique. Multiple devices are commonly used to measure flow velocity around a train in a wind tunnel. For example, the speed can be directly measured with an anemometer or derived from a pressure measurement with multiple probes. The disadvantage of these measurements is that the devices must be inserted in the flow field and thereby influence the surrounding flow. Nonintrusive methods as particle image velocimetry (PIV) and laser Doppler anemometry (LDA) do not have this disadvantage. Both are optical measurement techniques which rely on lasers and the injection of seeding particles which can be detected by cameras. With the help of software, a quantitative measurement of the velocity can be performed without influence on the flow as long as the seeding particles are small.

A disadvantage of PIV is the complexity and amount of time to design the experiment and the limited amount of general information from a measurement as it only occurs at a specific part. For the underbody region of the train, there is also difficulty in measuring the flow because of the small area between the floor and the under surface. A measurement technique which is not quantitative but qualitative is smoke visualisation. It is relatively easy to conduct, covers a large geometric domain, and shows the general flow behaviour around the train model and vortex zones. The goal of this study is to obtain insight into the general characteristics of the underbody flow. As a detailed quantitative validation of the CFD model is not necessary, this validation study employs a smoke visualisation technique.

The remaining part of this chapter describes the geometric model of the vehicle, the experimental structure, the results, and comparisons with the numerical simulations as part of its validation.

4.2 Geometric Setup

The experimental validation was performed in an 8m-long, closed-loop wind tunnel at the Eindhoven University of Technology (Figure 13). The height of the measurement section is 1050 mm, and the width is 700 mm. To avoid the influence from the boundary

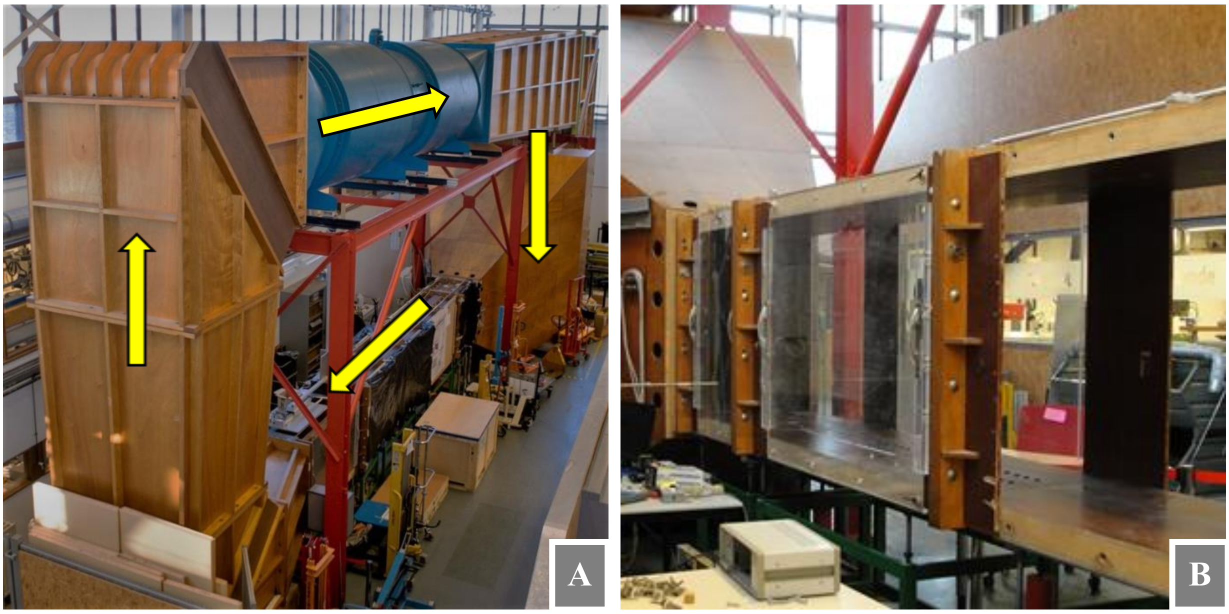

Figure 13: Photographs of the wind tunnel at the Eindhoven University of Technology in the Netherlands.

layer caused by the walls of the wind tunnel on the flow around the geometric model, a maximum scale ratio of around 1:5 (4% blockage) between the linear dimensions of the geometric model and the wind tunnel was determined. Comparing the dimensions of the SIM, the width, in this case, is the constrained dimension (see Table 7).

Table 7: Geometric details of the SIM (original and scaled) compared to the sizes of the wind tunnel

Dimension	Wind tunnel	SIM (Original)	SIM (Scale)	Ratio (scale model : wind tunnel)
Height	1,050 mm	3,240 mm	180 mm	1 : 5.8
Width	700 mm	2,520 mm	140 mm	1 : 5
Length	8,000 mm	8,424 mm	468 mm	1 : 17.1

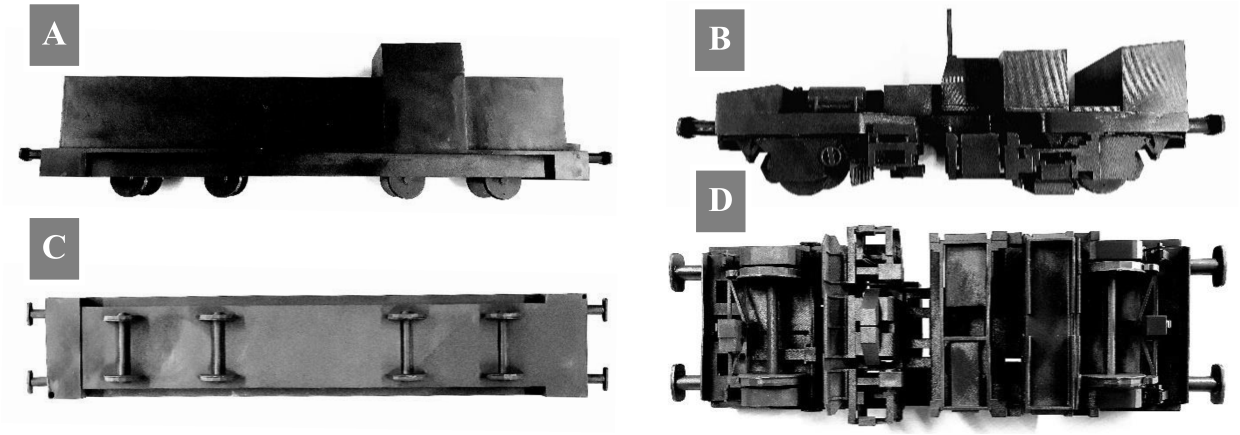

Figure 14: Photographs of the scale models. **A:** Side view of the locomotive, **B:** side view of the SIM, **C:** bottom view of the locomotive, **D:** bottom view of the SIM.

Therefore a 1:18 scale model was used to perform the wind tunnel test. This scale model has been 3D-printed via the rapid prototyping technique with the material Standard Bleu X10, which is a light but relatively strong printing material (Figure 15). After printing, the scale model was painted a dark-grey colour to have enough contrast with the smoke and the black background of the wind tunnel (Figure 14).

To minimise the effect of the boundary layer near the flow, a 3m-long transparent plate (henceforth called a “floor”) was installed at a height of 200 mm above the wind tunnel’s floor. This false floor covers the full width of the wind tunnel and is made of 1cm-thick transparent plexiglass. The floor is supported by 18 aluminium rods to keep the floor in place and avoid it bending under its own weight. On the transparent floor, a

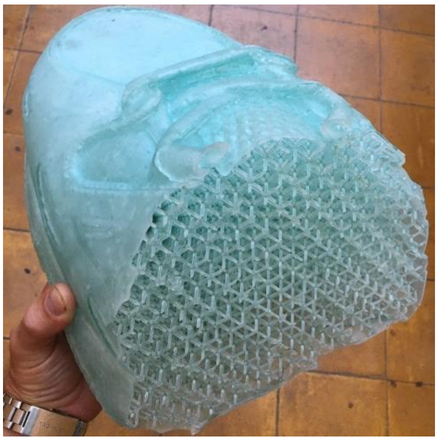

Figure 15: Example of raw printed material Standard Bleu X10.

Table 8: Dimension specifications of the components used in the experimental setup

Object	Dimension	Value
False floor	Length	3,000 mm
	Thickness	10 mm
	Width	700 mm
Railhead	Length	3,000 mm
	Height	10 mm
	Width	4 mm
Sharp nose	Length	50 mm
	Width	700 mm
	Thickness	10 mm
	Angle	15°
Wing	Length	50 mm
	Width	700 mm
	Thickness	10 mm
	Angle	15°
Pillars	Length	200 mm
	Diameter	30 mm

20mm-high scale model of the railhead is mounted. The rail has a width of 10 mm and covers the full 3,000mm-long floor.

The floor has a sharp (15˚) edge to reduce the influence of the frontal surface of the floor. At the end of the floor, a 5cm-long wing element at an angle of 15˚ was installed to optimize the flow field in the wind tunnel. Table 8 presents a full overview of the dimensional details of these components. The scale models of both vehicles were placed at the very front end of the floor to maximally reduce the influence of the natural boundary layer in the wind tunnel and to have as small a boundary layer as possible on the false floor (Figure 16A).

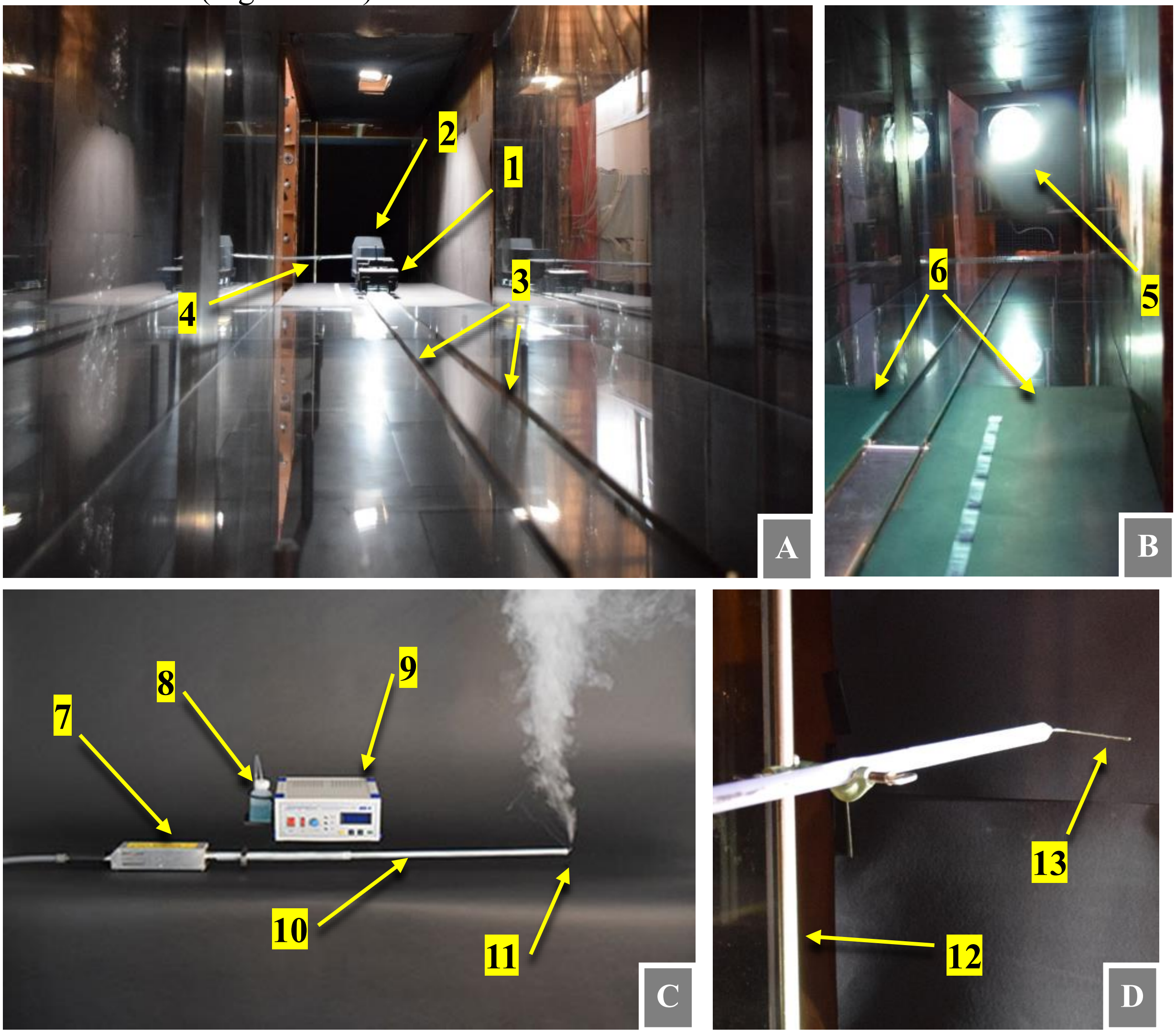

Figure 16: Geometric setup of the wind tunnel experiment. **A**: Longitudinal inside view in the opposite direction of the flow field, **B:** longitudinal inside view in downstream direction flow field, **C:** photograph of the smoke generator, **D:** Photograph of the nozzle outlet of the smoke injector**. 1)** Scale model of the SIM, **2)** scale model of the locomotive, **3)** left and right scale model of the railhead, **4)** smoke injector, , **5)** high-intensity spotlight, **6)** black matte paper, **7)** heating element, **8)** smoke fluid reservoir, **9)** smoke control unit, **10)** air transport tube, **11)** injection nozzle, **12)** tripod, **13)** injection nozzle.

A Safex Controller NS4 smoke injector was placed a few centimetres before the front end of the vehicle. The smoke generator consists of a long metal pipe, a heat element, a smoke fluid reservoir, a pump, and a long metal tube (Figure16C). [19]The pump pushes the smoke fluid through the pipe and was heated at the very end of the tube, where the fluid would condensate into white smoke. At the end of the tube, a nozzle was mounted with a diameter of 2 mm, pointing to the front end of the vehicle (Figure16D).

The inside of the wind tunnel was covered with matte black paper to reduce reflection and increase contrast to the white smoke. Additionally, the transparent floor was covered with matte black paper except for the area between the railheads.

Under the wind tunnel, two spotlights were installed. The light was directed in the upward direction through an open area in the tunnel and through the transparent floor to light up the underbody of the scale models (which is why the area between the railhead was not covered with black paper). Furthermore, on the roof of the wind tunnel, a spotlight was mounted in the downward direction to light up the full upper area of the vehicles. At the end of the tunnel, a large spotlight was mounted in the longitudinal direction of the wind tunnel to make the smoke visible (Figure 16B).

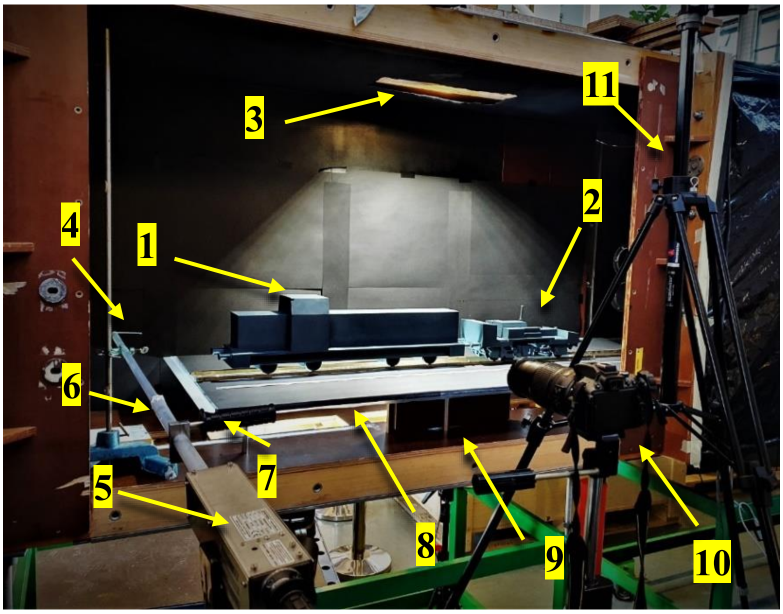

1. **Locomotive**
2. **SIM**
3. **Spotlight**
4. **Smoke nozzle**
5. **Smoke heater**
6. **Smoke injector tube**
7. **Sharp edge of floor**
8. **Floor**
9. **Floor pillar**
10. **Camera**
11. **Camera tripod**

Figure 17: Photograph of the geometric and optic setup of the wind tunnel experiment taken from the semi-open side of the wind tunnel.

---

[19] Source: https://www.dantecdynamics.com/product/safex-fog-probe-system-ns4-220-vac.

A camera on a tripod was placed at the partially open side of the wind tunnel at the same height as the vehicles to record the flow with a side view (Figure 17). The smoke injector was placed in a lateral position through the semi-open window into the wind tunnel, and the nozzle, at the end of the injector, was pointed in the flow direction at the middle of the vehicle. Next to the wind tunnel, another large tripod was installed, which extended over the roof the wind tunnel. The camera could be switched to this tripod to record the flow from above via a gap in the wind tunnel.

4.3 Validation of Wind Tunnel Setup

The experimental design, as described in the previous section, has been validated via performing a cylinder flow experiment (Figure 18) by mounting a cylinder 150 mm in diameter on side wall of the wind tunnel at half height (Figure 18.1). The smoke injector was placed around 30 cm in front of the cylinder. The initial idea was to simulate a laminar Von Kármán vortex street, but this phenomenon occurs at a Reynolds number of around 200, which means a very low speed must be realised with the current cylinder diameter. Decreasing the diameter of the cylinder causes the flow behind it to not be clearly visible since the outflow beam of smoke is relatively wide (Figure 18.2).

However, velocities well below 1m/s in the current setup resulted in two other major problems. The first is that the smoke has a relatively high temperature compared

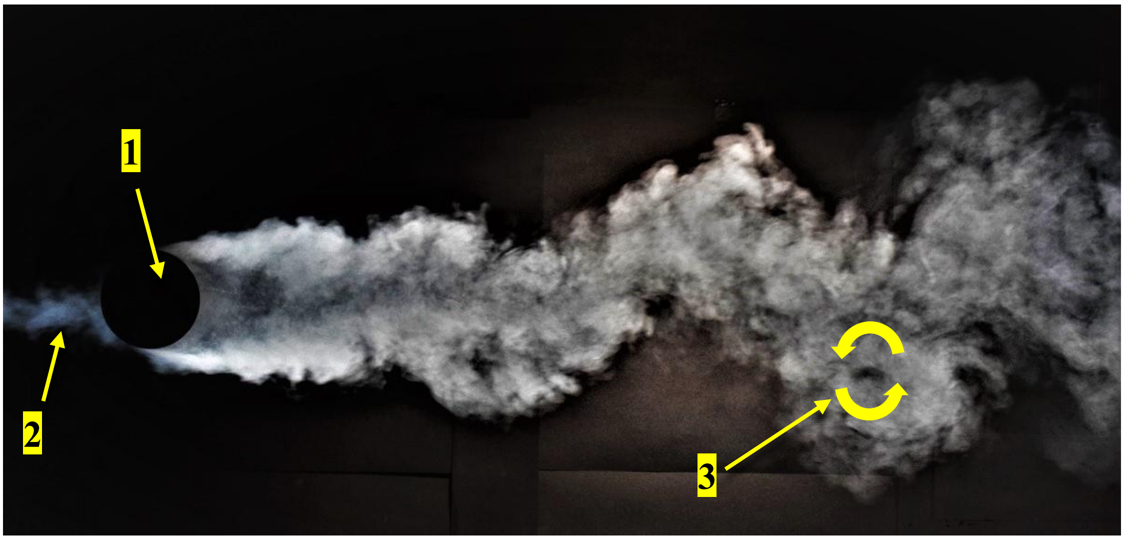

Figure 18: Results of the cylinder flow experiment with a flow speed of ~0.5 m/s and a cylinder diameter of 150 mm. **1)** Outflow at the nozzle of the smoke generator, **2)** cylinder, **3)** the creation of a anticlockwise vortex.

to that of the air in the wind. This is because the smoke generator works by heating up smoke liquid, which then condensates when it exits the nozzle. The effect of this temperature difference is that the smoke tends to stream a bit upwards, which is aggravated by lowering the speeds. A second negative aspect of lowering the speed, is the velocity difference between the outflow of the condensed smoke at the nozzle and the airflow in the wind tunnel. Since the smoke generator has a fixed flux of outflow, this means that the outflow velocity is at some point higher than the airflow in the wind tunnel. This velocity difference causes flow instabilities directly after injecting the smoke in the wind tunnel, and the small beam of injected smoke disappears rapidly.

Therefore, this experiment was performed with a flow speed of ~0.5 m/s, resulting a Reynolds number of 15,000 which is, in this case, the optimal balance to avoid the negative effects of a too low flow speed and the Reynolds number. This results in the generation of a turbulent vortex street, as shown in Figure 18 and anticlockwise vortices (Figure 17.3).

4.4 Experimental and Numerical Configurations

The setup described in the previous section was used to perform a series of experiments, each with a different configuration setting. Four experimental configurations were performed: two different heights of smoke injection, both in the two driving directions (Table 9). The smoke was injected a few centimetres in front of the first vehicle at the heights of 10 mm and 100 mm from the floor, respectively.

Table 9: Overview of the four different experimental configurations

Configuration	Orientation	Injection height
1	FDD	100 mm
2	FDD	10 mm
3	BDD	100 mm
4	BDD	10 mm

To compare the wind tunnel visualisation with the numerical results, an additional numerical setup, which includes extra elements specific to the wind tunnel, was performed in COMSOL to get a better comparison between both situations. This additional structure was based on the general experimental design described in chapter

3, but in this case, more conditions were added to reflect the conditions in the wind tunnel (Figure 19). The temporary simulation was performed for both driving directions based on a fine mesh size.

One of the main differences between the original setup and this one were the model sizes. The size of the full model was reduced by a 1:18 ratio, mimicking the wind tunnel setup. Other differences are the boundary conditions at the side (Figure 19.1) and upper (Figure 19.2) walls, which were set to a no-slip situation to simulate the influence of the wind tunnel walls. The fake floor (Figure 19.3), including the pillars (Figure 19.4), the sharp nose (Figure 19.5), and the wing at the end of the floor (Figure 19.6), were also added to the simulation. Additionally, the dimensions of the fluid domain in the simulation environment were identical to the sizes of the wind tunnel. Both numerical computations converted to a solution, and the statistical details are listed in Table 10.

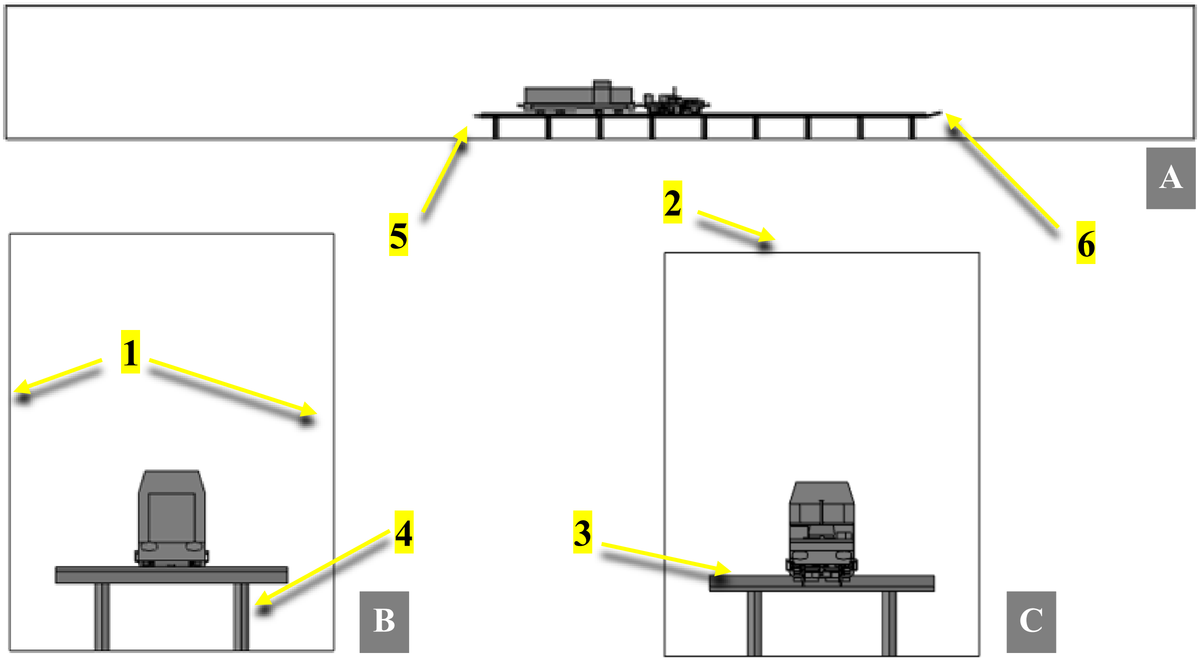

Figure 19: Simulation setup, which is comparable to the geometric setup in the wind tunnel to validate both results against each other. **A:** Side view of the numerical set-up, **B:** rear-view of the numerical set-up, **C:** front view of the numerical set-up. **1)** No-slip side walls, **2)** no-slip upper wall, **3)** fake floor, **4)** false flour pillar, **5)** sharp nose of the false floor, **6)** wing at the end of the false floor.

Table 10: Calculation details of the additional numerical setup of both the pushed orientation (FDD) and the pulled orientation (BDD) performed on HP Desktop (128GB RAM) with two Intel(R) Xenon(R) 3.10 GHz processors (64 cores) with Windows 10 Enterprise 2016 (64 bit) as the operation system

Value	FDD	BDD
Number of elements	3,613,959	3,598,223
Mesh quality	0,6366	0,6391
Calculation time	05h:44m:35s	05h:30m:55s

4.5 Experimental Results and Validation

The results of the wind tunnel experiment, and how they are in agreement with the numerical results discussed in section 4.4, are described in this section. It starts with the results of the FDD (section 4.5.1) followed by those in the BDD (section 4.5.2). The conclusion based on these results are found in section 4.5.3.

4.5.1 Results in the FDD

The wind tunnel results and the corresponding numerical results of the FDD (configurations 1 and 2 in Table 9) are presented in Figure 20. The side-view result of configuration 1 is shown in Figure 20A and its corresponding numeric results in Figure 20B. The test in Figure 20B was performed by visualising a streamline which passes the same position as the location of the smoke injector in the wind tunnel, plus 199 streamlines in the cross-sectional area of 2 cm around this point. This means that a total of 200 streamlines are visualised.

Figures 20A and 20B both illustrate that the airflow from this injection point streams over the upper car body of the SIM (Figure 20.1–.2). Above the inter-car gap between the SIM and locomotive, the flow seems to divide into two directions (Figure 20.3–4). From this point, one-part flows further in the longitudinal direction and streams over the upper part of the locomotive (Figure 20.5–6). The second part flows downward in a z-shaped pattern through the inter-car gap in the direction of the ground (Figure 20.7–8) and further between the ground and the under-car body of the locomotive. Both

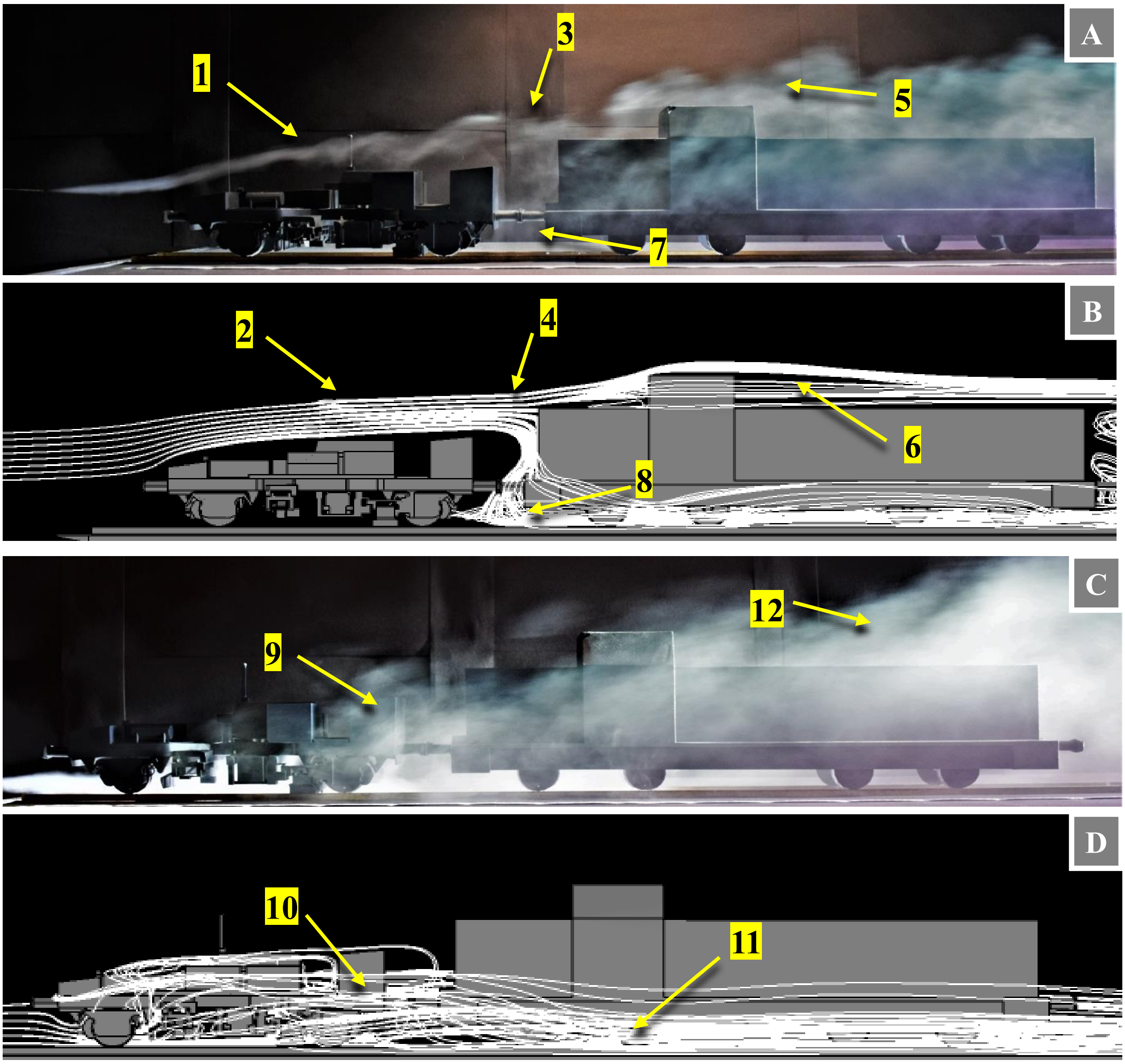

Figure 20: Side view of the experimental and numeric results in the FDD. **A**: Experimental result of configuration 1, **B**: numeric result of configuration 1, **C**: experimental results of configuration 2, **D**: numeric result of configuration 2. **1-2)** After smoke injection, the flow streams direct over the upper car-body, **3-4)** a part of the flow separates from the main flow and streams downward into the inter-car gap, **5-6)** the main flow goes further and streams over the upper-surface of the locomotive. **7-8)** after intersecting the inter-car gap the separated part of the flow streams further trough the under-body region of the locomotive, **9&10)** a part of the underbody flow of the SIM is pushed to the sides, **11)** after this, the flow moves further trough or close to the underbody region of the locomotive, **12)** whereas the wind tunnel result shows a more upward flow along the length of the locomotive.

the wind tunnel measurement and numerical results show this flow phenomenon, but the main differences are observed in the smaller structures of the flow. Whereas the numerical results indicate a smooth flow pattern, the wind tunnel results reflect more fluctuations at a smaller scale. This discrepancy can be explained by the RANS turbulence model used for the numerical simulation since this model is based on the assemble averaged flow.

Figures 20C and 20D depict the results of the injection of smoke at a low height in the FDD mode (configuration 2 in Table 9). Both findings show that the flow initially streams through the under-car body region of the SIM, but its complex underbody geometry causes a strongly turbulent flow state. A part of the flow is pushed to the sides, escapes out of the underbody region, and streams further along the sides of the SIM. This is clearly visible in both results in Figure 20.9–10. From this point, there appears to be a difference between the numerical and wind tunnel results. The former reflects

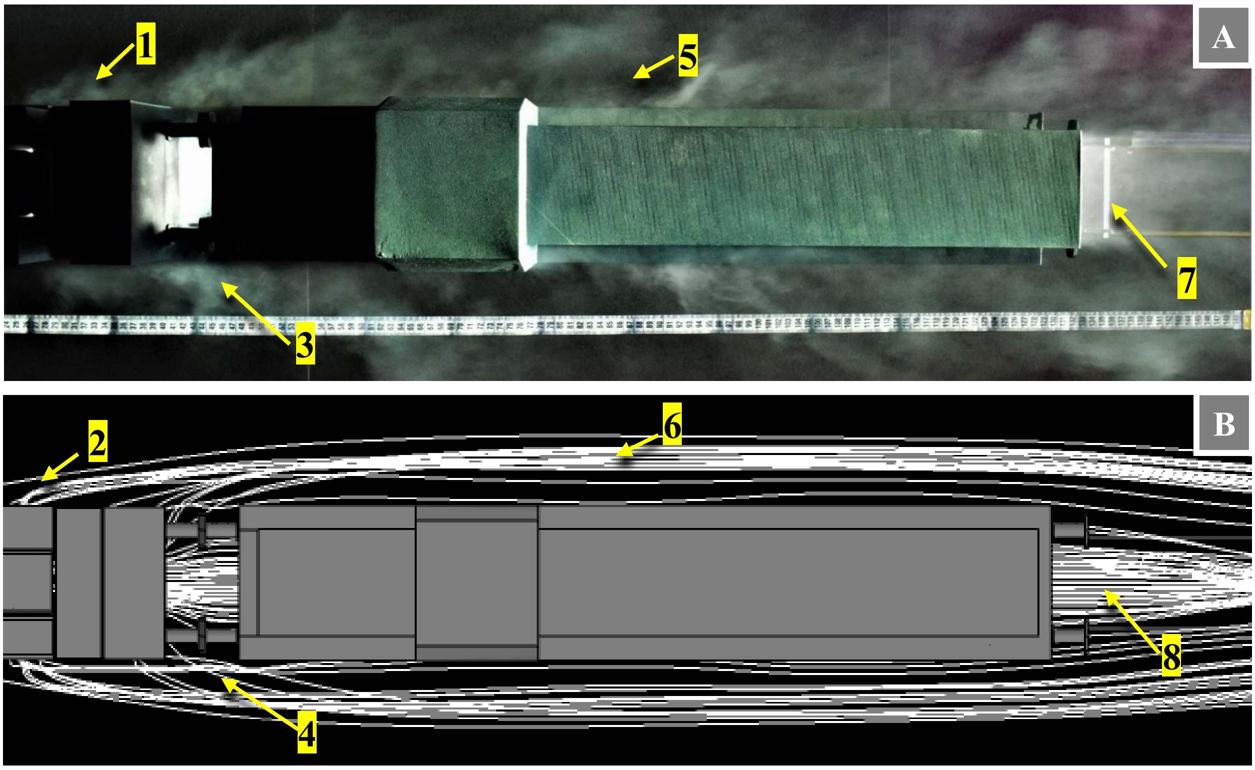

Figure 21: Upper view of the experimental and numeric results in the FDD. **A**: Experimental result of configuration 2, **B**: numeric result of configuration 2. **1-2)** Flow is escaping the underbody region of the SIM at its rear side, **3-4)** this phenomenon also appears at the inter-car gap between both vehicles, **5-6)** the escaped flow moves further parallel to the locomotive in the downstream direction, **7-8)** The rest of the flow moves straight forward, passing the full underbody region, and escapes the region below the bottom of the locomotive at the rear side.

that the flow inclines downward and to the underbody region of the locomotive (Figure 20.11). The latter result, on the other hand, shows a more upward flow at the sides of the locomotive (Figure 20.12). An explanation for this upward flow is the relatively high temperature and therefore the low density of the smoke. The relatively low speed of the air at the rear side of the SIM increases this effect.

The top-view results of this same configuration are displayed in Figure 21 (Figure 21A, the experimental results and Figure 21B, the numerical results). Both findings reveal that the smoke is partly escaping the region below the bottom of the SIM at both sides of the rear part of the vehicle (Figure 21.1–2). This phenomenon also appears at the inter-car gap between both vehicles (Figure 21.3–4). The escaped flow moves further parallel to the locomotive in the downstream direction (Figure 21.5–.6). The rest of the flow moves straight forward, passing the full underbody region, and escapes the region below the bottom of the locomotive at the rear side (Figure 21.7–8).

4.5.2 Results in the BDD

The experimental and numerical results of the BDD setup are presented in Figure 22 (Figures 22A and 22B are the results of the high-level smoke injection, configuration 3 in Table 9). These findings reveals that the flow moves upwards over the locomotive (Figure 22.1–2) and then follows the upper surface. Then, behind the locomotive, the flow moves slightly downwards and transfers in the direction of the upper surface of the SIM (Figure 22.3–4). Both results are in good agreement, and none of the injected smoke particles reaches the under-body region, which means that air particles from the upper side of the locomotive do not reach the sensor unit. The main difference between the results is the diverging flow above the SIM in Figure 22.3 compared to the smooth flow in Figure 22.4. This is probably a direct consequence of the averaging behaviour of the numerical turbulence model, which also was noted in Figure 20B.

The results of configuration 4 (low smoke injection in the BDD) are represented in Figures 22C and 22D, illustrating the injected smoke under the whole length of the locomotive (Figure 22.5–6). A part of the flow escapes from the under region of the locomotive, especially near the axles and wheels, and then follows a path parallel and close to the locomotive.

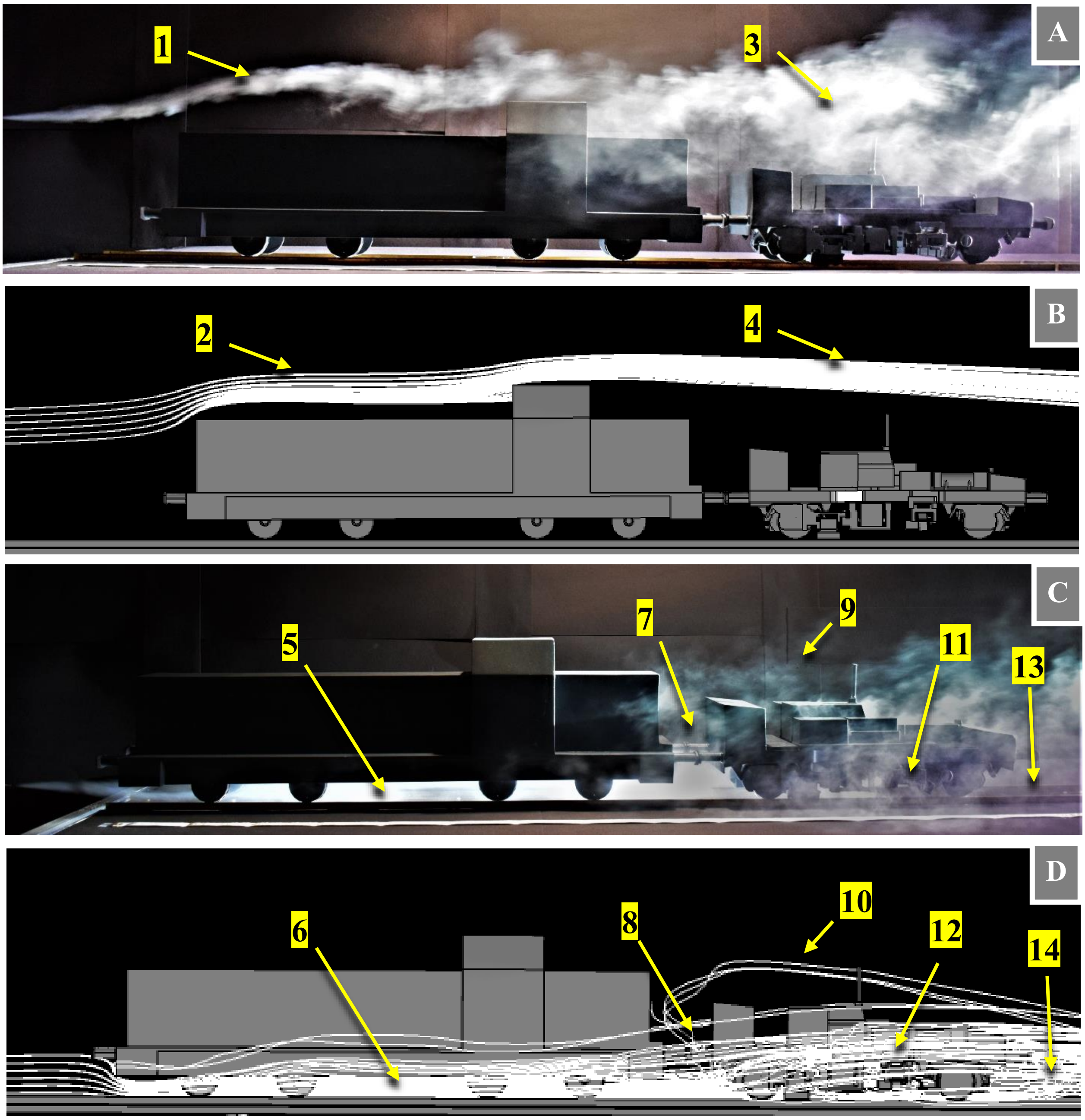

Figure 22: Side view of the experimental and numeric results in the BDD. **A**: Experimental result of configuration 3, **B**: numeric result of configuration 3, **C**: experimental result of configuration 4, **D**: numeric result of configuration 4. **1-2)** Direct after injection the flow moves upwards over the locomotive, **3-4)** behind the locomotive, the flow moves slightly downwards and transfers in the direction of the upper surface of the SIM, **5-6)** the injected smoke flows under the whole length of the locomotive, **7-8)** when the flow reaches the inter-car gap between the locomotive and SIM, it starts to become irregular and moves in three main directions, **9-10)** a first part of the flow moves upwards in the inter-car gap and then further over the upper body of the SIM, **11-12)** a second part moves into the underbody of the SIM, then to the sides of the vehicle, and then slightly upwards in the direction of the front part of the SIM, **13-14) a** third part moves straightforward through the underbody region of the SIM to its front end.

When the flow reaches the inter-car gap between the locomotive and SIM, it starts to become irregular and moves in three main directions (Figure 22.7–8). A first part of the flow moves upwards in the inter-car gap and then further over the upper body of the SIM (Figure 22.9–10). A second part moves into the underbody of the SIM, then to the sides of the vehicle, and then slightly upwards in the direction of the front part of the SIM (Figure 22.11–12). A third part moves straightforward through the underbody region of the SIM to its front end (Figure 22.13-14).

The top-view results of configuration 4 are found in Figure 23 **(**Figure 23A, the experimental results and Figure 23B, the numerical results). Both show that the injected flow in front of the locomotive moves straight through the whole underbody length. Only at the end of the locomotive, at the right side, the flow bends a bit to the side and starts becoming visible (Figure 23.1–2). This phenomenon also appears at the inter-car gap on the left side (Figure 23.3–4) and follows a path parallel to the SIM. The rest of the flow moves straight into the underbody region of the SIM and starts becoming irregular. Most of the air is then pushed to the sides of the SIM (Figure 23.5–6).

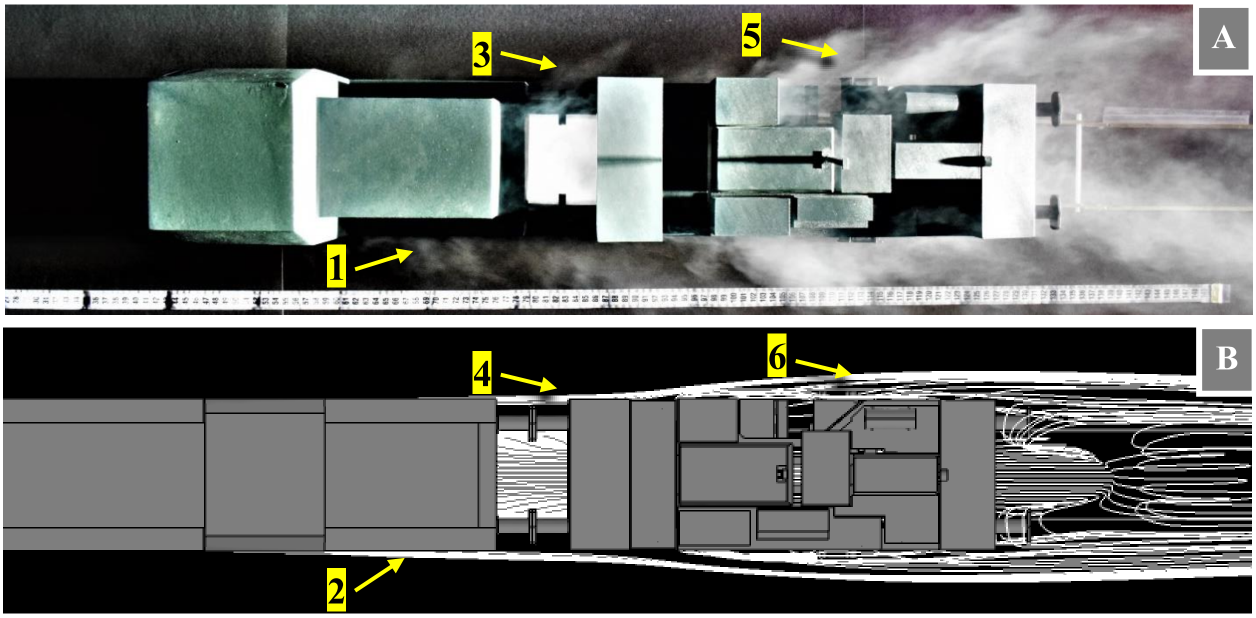

Figure 23: Upper view of the experimental and numeric results in the FDD. **A**: Experimental result of configuration 4, **B**: numeric result of configuration 4. **1-2)** At the end of the locomotive, at the right side, the flow bends a bit to the side and starts becoming visible, **3-4) t**his phenomenon also appears at the inter-car gap on the left side, **5-6)** the flow at the underbody region of the SIM and starts becoming irregular and most of the air is then pushed to the sides of the SIM.

4.6 Conclusion

The main flow observed from the wind tunnel experiment is generally in good agreement with the numerical results, but two major discrepancies are observed. The first one entails the flow fluctuations observed in the experiment, which were not seen in the numerical results. This is a consequence of the averaging behaviour of the turbulence model (i.e. the κ-ε turbulence model used describes the average time-independent flow, whereas the wind tunnel result is an instantaneous photograph of a real time-dependent flow).

The second discrepancy is the upwards flow of the experimental results in configurations 2 and 4, which is not observed in the numeric results. A plausible reason for the phenomenon is that the relatively high temperature of the smoke causes this upwards movement.

Nevertheless, the numerical results are in agreement with the average main flow of the experimental results, and therefore it can be concluded that the quality of the numerical model has reached a sufficient level, forming a basis on which to expand with more realistic complexities.

Chapter 5

Configuration Analysis and Numerical Results

The experimental validation described in chapter 4 indicates that the numerical results are in good agreement with those from the wind tunnel test. Together with the findings from the mesh validation (chapter 3), this ensures enough confidence that the quality of the numerical model is at a sufficient level. This means that the numerical model provides a good description of the aerodynamics of the vehicles, which can be extended to study more complex scenarios.

This chapter starts with a description of the numerical setup used to analyse the influence of these more complex scenarios (section 5.1) and their results (section 5.2). The findings are then used to build an additional simulation, where the scenarios are combined in a single configuration. The general result of this scenario is discussed in section 5.3. A streamline analysis of those flows passing the sensor units is performed in section 5.4, followed by a detailed analysis of the zone near the sensor units.

5.1 Configuration Setup

The numerical setup described in chapter 3 was simplified to validate it with the wind tunnel tests; hence, there are several discrepancies with the real situation. Some of those simplifications could have a major influence, as mentioned in the literature review.

First, one major difference is the relative motion between the train and the ground. In the real situation, the relative motion will induce higher velocities near the ground and thereby influences the flow near the bogie region and the sensor units. Second is the influence of ballast and sleepers on the underbody flow. The current simulation results are based on a flat surface treatment. Neither the ballast nor sleepers have been considered. As described in the literature review, several studies have reported an influence of the geometry of the ballast and sleepers on the underbody flow. The third discrepancy involves the rotating motion of the wheels and axles.

Table 11: Overview of the four different simulation configurations, wherein the simulation of the track, the rotating wheels, and the relative motion of the ground are individually added to each configuration.

Config.	Description	Derivative	Condition
1	Basis Configuration (as in chapter 3)	BC	Vehicles: standing still Ballast and sleeper: flat and smooth Ground: not moving Wheel: not rotating
2	Ballast and Sleeper Configuration	BSC	Vehicles: standing still Ballast and sleeper: with roughness Ground: not moving Wheel: not rotating
3	Moving Ground Configuration	MGC	Vehicles: standing still Ballast and sleeper: flat and smooth Ground: moving Wheel: not rotating
4	Rotating Wheels Configuration	RWC	Vehicles: standing still Ballast and sleeper: flat and smooth Ground: not moving Wheel: rotating

Several researchers have found a major impact from the rotating wheels and suggested including the rotating boundary condition at the wheels to numerically simulate the underbody flow. The influences of these three additional features are individually analysed in different simulation configurations and compared with the simplified numerical (basis) simulation. These configurations are summarised in Table 11.

Configuration 1 is the simplified configuration described in chapter 3 i.e., the basis configuration (BS). Configuration 2 includes the simulation of both the ballast and sleepers and is called the ballast and sleeper configuration (BSC). This simulation is performed by adding an equivalent roughness to the simulated ground surface. This equivalent roughness is set to 7 mm, which is an average value from numerical and experimental data in literature (see section 2.3.2). Configuration 3 is the simulation of the relative motion between the ground (MGC) and the train by simulating a moving boundary condition between the ground surface and the rails, which has the same velocity as the inlet velocity in the fluid domain. Configuration 4 is the simulation of the rotating wheels and axles (RWC).

Table 12: Mesh and calculation statistics of the four different numerical configurations in the pushed orientation (FDD) performed on HP Desktop (128GB RAM) with two Intel(R) Xenon(R) 3.10 GHz processors (64 cores) with Windows 10 Enterprise 2016 (64 bit) as the operation system

Value	BC	BSC	MGC	RWC
Number of elements	3,619,959	3,610,094	3,994,322	3,613,959
Mesh quality	0.6336	0.6369	0.6287	0,6366
Calculation time	05h:44m:35s	05h:59m:45s	09h:20m:51s	05h:37m:12s

Table 13: Mesh and calculation statistics of the four different numerical configurations in the pulled orientation (BDD) performed on HP Desktop (128GB RAM) with two Intel(R) Xenon(R) 3.10 GHz processors (64 cores) with Windows 10 Enterprise 2016 (64 bit) as the operation system

Value	BC	BSC	MGC	RWC
Number of elements	3,598,223	3,598,223	3,994.322	3,613,959
Mesh quality	0.6391	0.6391	0.6391	0,6336
Calculation time	05h:30m:55s	08h:30m:09s	05h:11m:55s	05h:37m:12s

This configuration involves a rotational, no-slip boundary condition at the treads of the 12 wheels and on the surface of the six axles of both vehicles with an effective rotational speed of 5 m/s compared to the treads of the wheels, which is equal to the inlet velocity of the model domain. A fine mesh was used for all eight numerical configurations, and all calculations have converged to a solution. Statistical details of the simulation of the FDD are summarised in Table 12 and the BDD in Table 13. The results of these calculations are discussed in the next section.

5.2 Influence of the Different Configurations

To analyse the influence of the different configurations (compared to the BC), the pressure, velocity, and vorticity are derived and compared (a total of four scenarios, each with two moving directions). These three parameters are determined from a virtual line under the vehicles along the middle of the track at TOR height. The results are visualised (in dimensionless form) in six different graphs (Figure 24). The BC is depicted by the black line in these graphs.

5.2.1 Effect on Velocity

The velocity results at TOR height are given in Figures 24A and 24B, which show that the BSC and BC have almost the same velocity distributions except that the velocity of the BSC is slightly lower than the BC. However, near the front part of the leading vehicle, both configurations reveal more identical velocities (Figure 24.1–2). The slightly lower velocity of the BSC is likely due to the resistance generated by the roughness of the ground surface. In contrast to the BC, the MGC shows a higher velocity under the whole length of both vehicles (Figure 24.3–.4), which can be explained by the higher velocity induced by the moving ground, which has the same velocity as the inlet velocity.

The velocity of the RWC displays a more complex behaviour, especially in the FDD, where it is much lower between the rear axle of the SIM and the first half of the locomotive (Figure 24.5). In the BDD, the RWC has two peaks in the velocity curve, one at the rear axle and one at the front axle of the SIM (Figure 24.6).

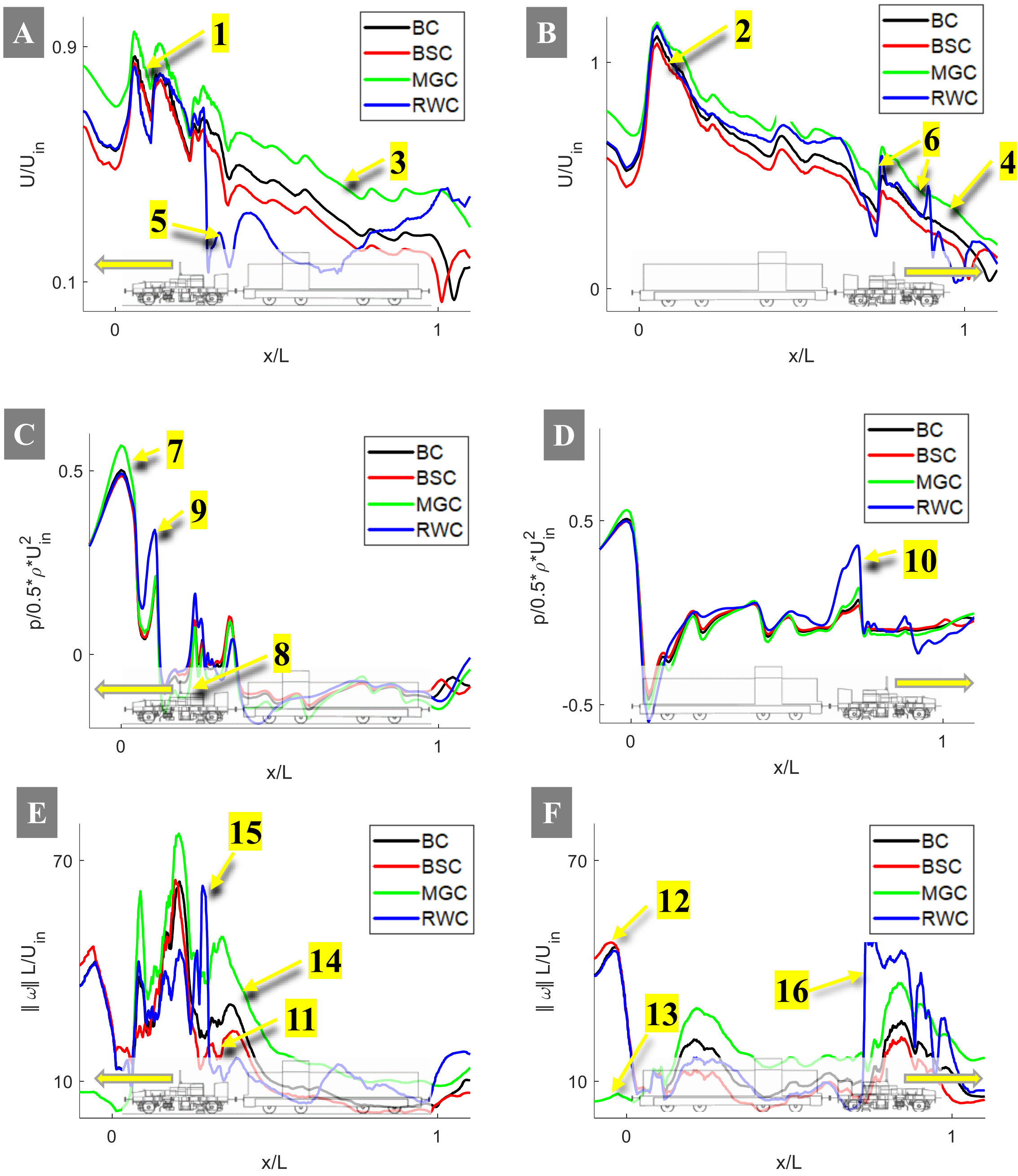

Figure 24: Relative velocity, pressure, and vorticity at TOR in relative longitudinal direction for four configurations and two driving directions. **A**: Relative velocity in the FDD, **B**: relative velocity in the BDD, **C**: relative pressure in the FDD, **D**: relative pressure in the BDD, **E**: relative vorticity in the FDD, **F:** relative vorticity in the BDD. **1-2)** Near the front part of the leading vehicle, both the BC and the BSC reveal almost identical velocities, **3-4)** **t**he MGC shows a higher velocity under both vehicles, **5)** the velocity of the RWC, is much lower between the rear axle of the SIM and first half of the locomotive, **6)** in the BDD, the RWC has two peaks in the velocity curve, **7-8)** the pressure has a higher peak value in the front of the SIM and a lower pressure in between its e axles, **9-10)** the moving wheels and axle largely affect the pressure near the front axle of the SIM (FDD) and near the rear axle (BDD), **11)** the BSC generally displays a slightly lower vorticity under the SIM and locomotive, **12)** however, before passing the underbody region of the vehicles, the flow reveals a slightly lower vorticity, **13)** The MGC presents very low vorticity upstream and downstream of the vehicles, **14)** under the vehicles of the SIM and locomotive, there is a much higher vorticity; **15-16)** large vorticity peak just before the rear axle in the FDD, and just after the rear axle in the BDD.

5.2.2 Effect on Pressure

When viewing the overall pressure (Figures 24C and 24D**),** there is almost no difference between the BSC and the BC. However, the MGC shows much more influence on the pressure in both driving directions. For example, in the FDD, the pressure has a higher peak value in the front of the SIM (Figure 24.7) and a lower pressure in between the axles of the SIM, compared to the BC (Figure 24.8). The RWC has even more influence on the pressure compared to the BC. The moving wheels and axles seem to largely affect the pressure near the front axle of the SIM in the FDD (Figure 24.9) and near the rear axle in the BDD (Figure 24.10).

5.2.3 Effect on Vorticity

The values of the dimensionless magnitude of the vorticity at TOR are reflected in Figures 24E and 24F for the FDD and the BDD, respectively. The dimensionless vorticity magnitude shows a more fluctuating behaviour compared to the velocity and the pressure, especially under the SIM. However, at the underbody of the locomotive, the vorticity is smoother. This is due to the smoother under surface of the locomotive compared to the more complex under surface of the SIM. The BSC generally displays a slightly lower vorticity under the SIM and locomotive compared to the BC (see, e.g., Figure 24.11). Before passing the underbody region of the vehicles, however, the flow reveals a slightly lower vorticity (Figure 24.12). The MGC presents very low vorticity upstream and downstream of the vehicles (Figure 24.13), which can be explained by the low velocity difference between the ground and the air in this region. However, under the vehicles of the SIM and locomotive, there is a much higher vorticity (see, e.g., Figure 24.14). This is likely due to the velocity difference between the moving ground and the stationary vehicles. The relative vorticity of the MWC at TOR presents a more complex behaviour. In the forward direction, it is generally lower under the SIM and higher under the locomotive and vice versa in the backward direction. There is also a large vorticity peak just before the rear axle in the forward direction (Figure 24.15) and just after the rear axle in the backward direction (Figure 24.16).

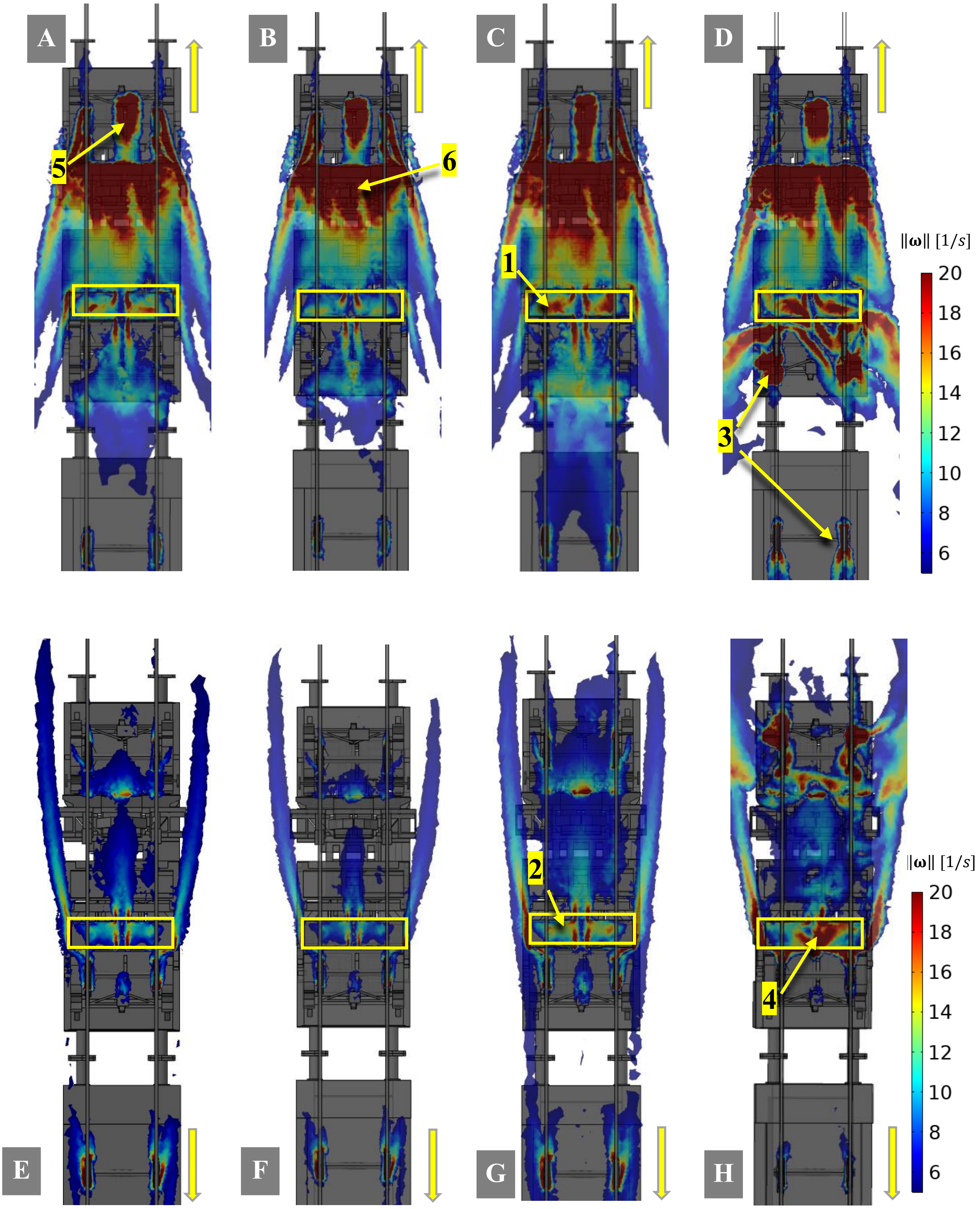

Figure 25: Visualisation of vorticity of the underbody region of the SIM moving in the forward direction. **A**: Basis configuration, **B**: ground roughness configuration, **C**: moving ground configuration, **D**: rotating wheels boundary condition. In the backward direction, **E**: basis configuration, **F**: ground roughness configuration, **G**: moving ground configuration, **H**: rotating wheels boundary condition. **1-2)** Large impact of the moving ground near the sensor units, **3-4)** large effect from the rotating wheels, especially near the wheels and the sensor units, **5-6)** for all configurations in the FDD, there is a large amount of vorticity at protruding elements, such as behind the brake system and windshield of the camera system.

In addition to a line graph of the vorticity at the middle of the track at TOR height, a 2-D plot of the vorticity at TOR is also illustrated in Figure 25. These figures visualise the vorticity over the whole surface area under the SIM. Here, Figure 25A is the BC, Figure 25B the BSC, Figure 25C the MGC, and Figure 25D the RWC for the FDD and Figures 25E–H for the BDD, respectively.

In agreement with the line graphs, these figures indicate a limited influence of ballast and sleepers but a larger impact of the moving ground, for example, near the sensor units (Figure 25.1–2). Additionally, it shows a large effect from the rotating wheels, especially near the wheels (Figure 25.3) and the sensor units (Figure 25.4). These figures reveal that for all configurations in the FDD, there is a large amount of vorticity at protruding elements, such as behind the brake system (Figure 25.5) and windshield of the camera system (Figure 25.6).

5.2.4 Conclusions of Configuration Analysis

This section analyses the influences of the different configurations of four scenarios (recap Table 11), each simulated in both driving directions. These eight configurations are compared by analysing the velocity, pressure, and vorticity at a virtual line in the middle of the track along both vehicles at TOR height. In addition, a 2-D visualisation of the vorticity at the whole under surface is examined.

All these analyses reveal a minor influence of the simulation of ballast and sleepers at this height, which is in agreement with other comparable studies in the literature review. The simulation of ballast and sleepers results, in general, in lower velocity and lower vorticity under both vehicles.

On the other hand, the consideration of a moving ground boundary condition reflects a major impact on the flow under the vehicle. This configuration shows, in general, higher velocity and higher vorticity under the whole vehicle. It also reveals higher pressure fluctuations at the front part of the vehicle. When including the moving ground condition, the vorticity near the sensor units increases significantly, especially in the FDD. The simulation of the rotating wheels and axles causes a large pressure peak at the rear part of the SIM when driving in the backwards direction. The rotating wheels also induce more vorticity under the SIM and especially around the sensor units. This major influence of the rotating wheels is in accordance with the expectation (described in chapter 2).

Finally, it can be concluded that the rotating wheels and the moving ground boundary conditions are essential for describing the flow under the SIM. Therefore, these two configurations are combined in an additional simulation described in the following sections.

5.3 General Flow Characteristics

As mentioned in the previous section, the relative motion between the train and ground (configuration 3) and the rotation of the wheels (configuration 4) are important simulation parameters combined to form a new configuration (configuration 5). An overview of this moving ground and rotating wheels configuration (MGC and RWC) is presented in Table 14.

Table 14: Overview of the combined configuration of the moving ground and rotating wheels

Config.	Description	Derivative	Condition
5	Moving Ground Configuration & Rotating Wheels Configuration	MGC & RWC	Vehicles: standing still Ballast and sleeper: flat and smooth Ground: moving Wheel: rotating

This more complex simulation setup is expected to better match reality and is calculated for both driving directions. Statistical details are summarised in Table 15. The general results of these simulations are described below.

Table 15: Simulation statistics of the combined RWC and MGC for both driving directions performed on HP Desktop (128GB RAM) with two Intel(R) Xenon(R) 3.10 GHz processors (64 cores) with Windows 10 Enterprise 2016 (64 bit) as the operation system

	FDD	BDD
Num. of mesh elements	3,6113,959	3,598,223
Mesh quality	0.6366	0.6391
Calculation time	05h:03m:21s	07h:03m:21s

The results of these numeric simulations are provided in Figure 26, which depicts a 3-D visualisation of the geometry of the SIM, including the locomotive and the vorticity (> 10 1/s) of the airflow around it. Figures 26A and 26B show the results of the FDD and BDD, respectively.

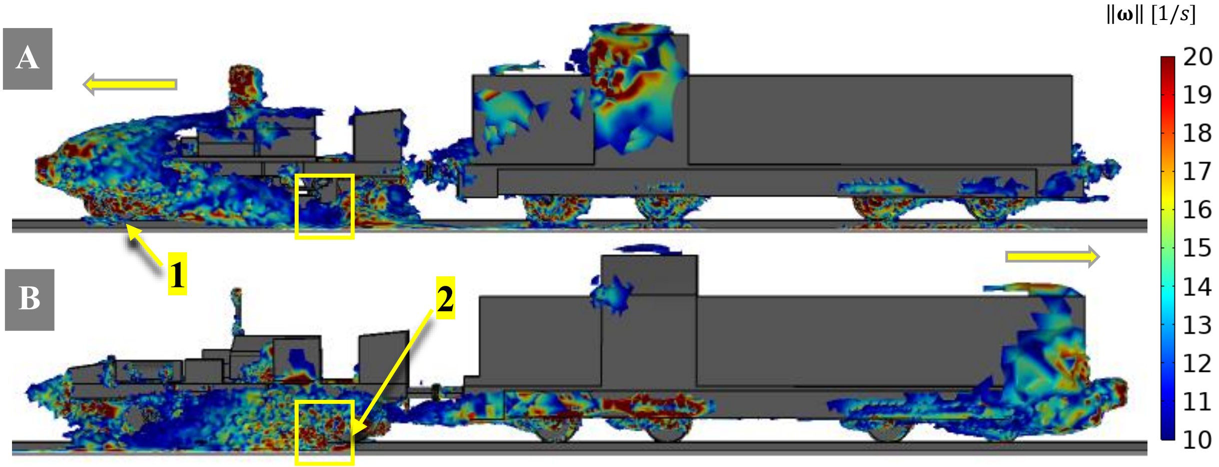

Figure 26: Side view of 3-D vorticity plot (> 10 1/s). **A**: FDD (to the left), **B**: BDD (to the right). **1)** In the FDD, the highest vorticity is in the front half of the underbody the SIM, **2)** in the BDD, the highest vorticity is at the second half of the SIM, which is close to the sensor unit.

The most unsteady flow occurs at the underbody of the SIM. In the FDD, the highest vorticity is in the front half of the underbody of the SIM (Figure 26.1). In the BDD, it moves to the second half of the SIM (Figure 26.2), which is close to the sensor unit.

A bottom-view 3-D visualisation of the vorticity (> 20 1/s) is depicted in Figure 27 (Figure 27A, the FDD and Figure 27B, the BDD). Both figures clearly indicate a low vorticity field at the smooth underbody of the locomotive (Figure 27.1). Near the wheels, the vorticity is relatively high, but significant differences in the intensity can be observed between both driving directions. In the FDD, all wheels of the locomotive and the rear wheels of the SIM generate more vorticity than those in the BDD (Figure 27.2). However, in the BDD, the opposite seems to be the case. The front wheels of the SIM generate relatively more vorticity, whereas the other wheels generate less (Figure 27.3). There also appears to be a large difference in vorticity near the sensor boxes in both

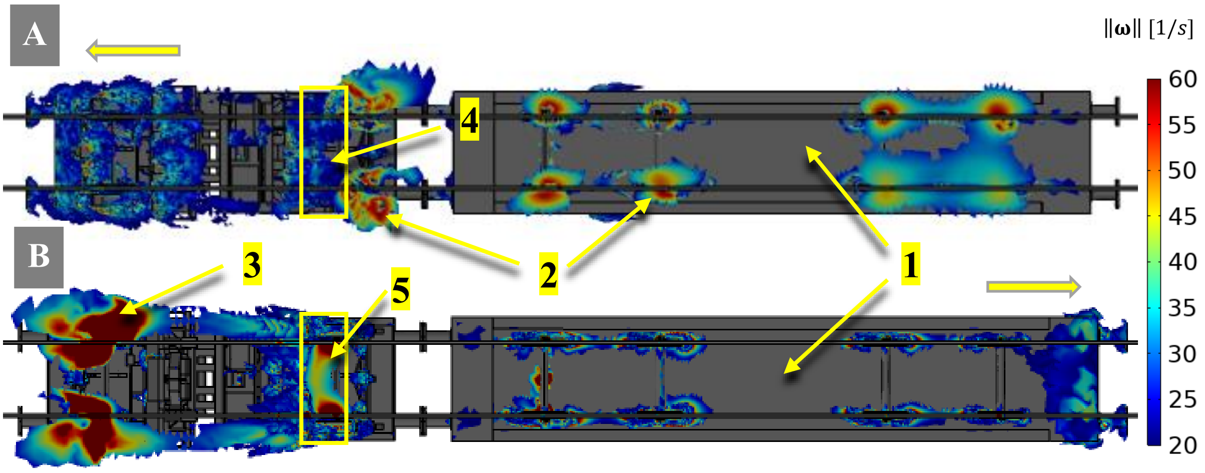

Figure 27: Bottom view 3-D vorticity plot (> 20 1/s). **A**: FDD (to the left), **B**: BDD (to the right). **1)** both figures clearly indicate a low vorticity field at the smooth underbody of the locomotive, **2)** in the FDD, all wheels of the locomotive and the rear wheels of the SIM generate more vorticity than those in the BDD, **3)** in the BDD the front wheels of the SIM generate relatively more vorticity, whereas the other wheels generate less, **4-5)** a large difference in vorticity near the sensor boxes in both driving directions, where in the FDD, this is quite low, whilst in the BDD, the vorticity is much higher.

driving directions. In the FDD, this is quite low (Figure 27.4), whilst in the BDD, the vorticity is much higher (Figure 27.5).

5.4 Streamline Analysis

A streamline analysis around the sensor unit can lead to a better understanding of the route which the air particles take upstream and downstream of the sensors. This also provides valuable information when designing a geometric modification to avoid large fluxes of air or droplets near the sensor units. Figure 28 is an illustration of 500 streamlines passing through the sensor unit.

Figure 28A shows the streamlines passing the sensor units in the FDD. It reveals that particles which reach the sensor unit generally come from the middle front part of the SIM and then move between the ground and the under surface of the SIM in the longitudinal direction towards the sensor units. Here, the air particles enter the sensor unit area in between the left and right units. The streamlines indicate a strong swirl downstream of the semi-closed areas of both sensor units. Here the air is temporary captured in swirling motion and then mainly escapes at the middle of the downstream part of both sensor units.

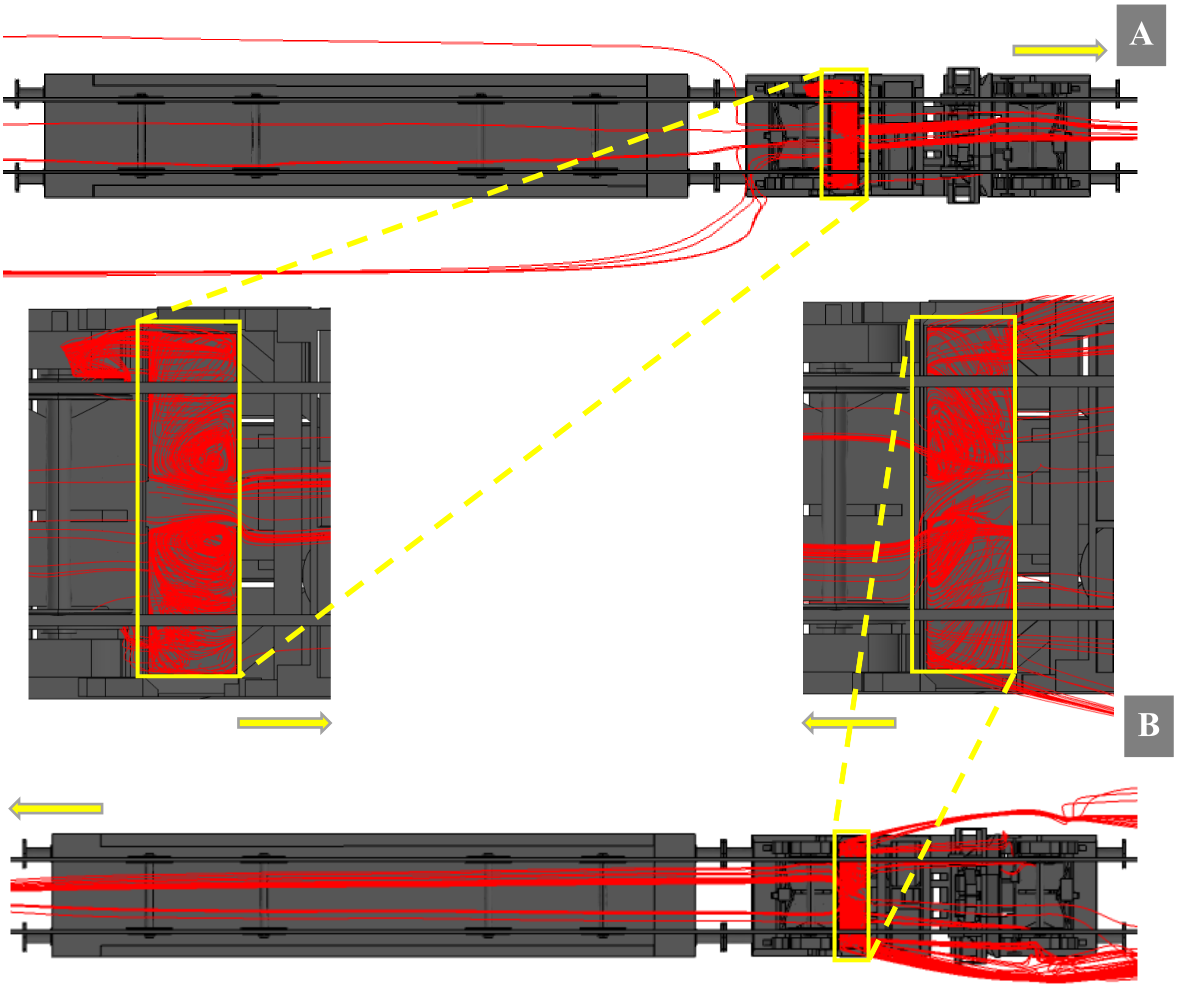

Figure 28: Visualisation of 500 streamlines passing the bottom of the sensor unit in **A**: the FDD and **B**: the BDD.

Figure 28B depicts the streamline pattern passing through the sensor units in the BDD. Here, the air particles come from the front part of the locomotive and move under its whole length. At the other side, they pass the space between the SIM and the locomotive, go further under the SIM, and enter the semi-closed area under it. In this area, the streamlines follow a swirl path through the whole under area of the sensor unit. The air particles exit this area mainly at the sides of the sensor unit and follow a path along the side of the SIM in the direction of its rear side.

In terms of particles carried by the air, it is reasonable to posit that dirt and water droplets from the underbody of the SIM and locomotive move with the airflow in the direction of the sensor unit. Since, in the BDD, the streamlines follow a path under the whole length of a 15m-long locomotive and the rear part of the SIM before they approach the sensor units, there is a high chance that this flow contains water droplets with dirt from the underbody of the locomotive.

5.5 Flow Near the Sensor Units

The previous section explains that air passing near the sensor units follows a complex path in the area near them, and air particles can stay there for a certain time before exiting the area. In the FDD, the streamlines seem to make a rotating movement in the area under the sensor units, whilst in the BDD, the flow is more chaotic. For more insight into the flow behaviour near the sensor units, a more in-depth analysis is discussed below.

5.5.1 Vorticity Field Near the Sensor Units

A 2-D image of the vorticity of the airflow near the sensor units is shown in Figure 29 (Figure 29A, the FDD and Figure 29B, the BDD). These plots only colour areas with $\|\omega\| > 10\mathrm{s}^{-1}$ vorticity. Both figures reveal a significant difference in flow behaviour between both driving directions. In the FDD, there is a jet of air near the edge of the brushes (Figure 29.1) on both sides in the direction of the window of the sensor units. The airflow directly under the centre of each sensor unit has relatively high vorticity (Figure 29.2).

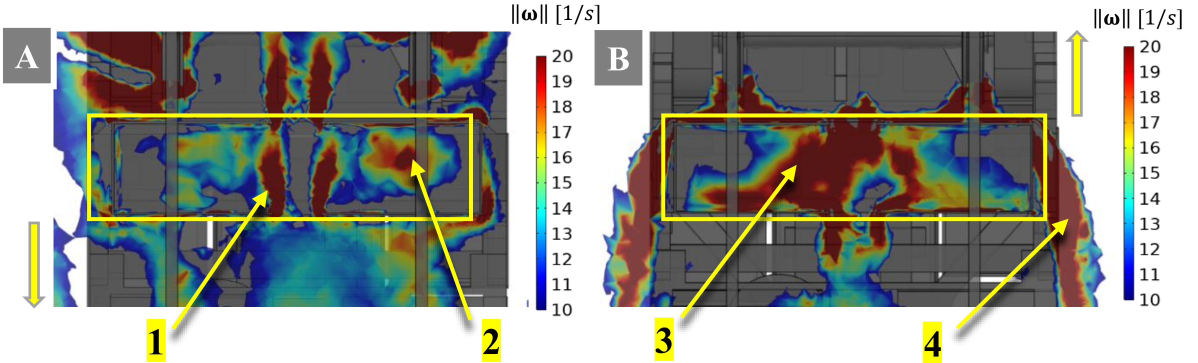

Figure 29: A 2-D visualisation of the vorticity $\|\boldsymbol{\omega}\| > 10s^{-1}$ just under the sensor units in **A**: the FDD and **B**: the BDD. **1)** is a jet of air near the edge of the brushes, **2)** The airflow directly under the centre of each sensor unit has relatively high vorticity, **3)** in de BDD**, t**he highest vorticity is observed at the inner side of each sensor unit, **4)** just next to the side of the sensor units, there is a large jet of vorticity caused by the air escaping the area under the sensor units at the outer sides.

In the BDD, the magnitude of the vorticity is relatively large compared to the area further away from the sensor units. The highest vorticity is observed at the inner side of each sensor unit (Figure 29.3). Additionally, just next to the side of the sensor units, there is a large jet of vorticity (Figure 29.4), caused by the air escaping the area under the sensor units at the outer sides.

5.5.2 Velocity Field Near Sensor Units

The streamline results in section 5.4 and the vorticity results in section 5.5.1 suggest a large difference of flow behaviour between both driving directions. In the FDD, the area just under the sensor units reveals relatively low vorticity and a swirling behaviour caused by the brushes at the sides of the units. In the BDD, the air under the sensor unit has a much higher vorticity and displays a much more chaotic swirling behaviour. For a better understanding of velocity values around the sensor units and the flow direction, a 2-D image of the velocity field and a normalised velocity vector field is presented in Figure 30.

In the FDD, there is a high velocity field in front of the sensor units (Figure 30.1). However, at the left and right sides of the SIM, the velocity magnitude is relatively low (Figure 30.2). This means that the velocity in the bogie area in front of the sensor unit

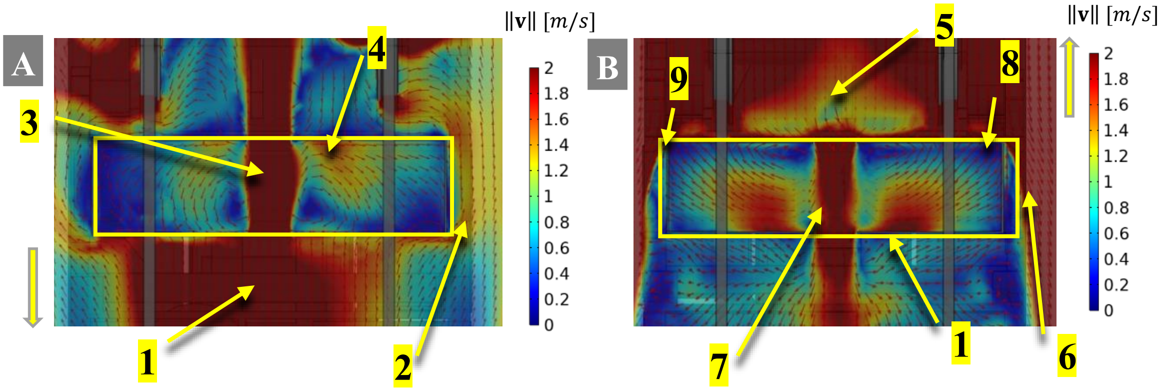

Figure 30: A 2-D visualisation of the velocity magnitude and direction field just below the sensor units **A**: in the FDD and **B**: in the BDD. **1)** A high velocity field in front of the sensor units, **2)** at the left and right sides of the SIM, the velocity magnitude is relatively low, **3)** in the space between the two sensor units, the velocity magnitude is relatively high, **4)** a circular flow with the highest velocity at the rear edge of the sensor unit, **5)** the flow velocity in front of the sensor units is relatively low, **6)** at both sides of the sensor units, the velocity in the BDD is much higher, **7)** the highest velocity is observed in the space between both sensor units, **8-9)** the flow seems to make a straight movement to the corner edges, **10)** relatively higher velocity under the sensor unit area compared to the FDD.

is higher than it is at the same longitudinal level at the sides of the SIM. Moreover, in the space between the two sensor units, the velocity magnitude is relatively high (Figure 30.3). It seems that the flow at the front end of the SIM mainly streams through the space between the sensor units. This high velocity flow between the sensor units generates a sideways flow under them, which results in a circular flow with the highest velocity at the rear edge of the sensor unit (Figure 30.4).

In the BDD, the flow velocity in front of the sensor units is relatively low (Figure 30.5) compared to that of the FDD (Figure 30.1). However, at both sides of the sensor units, the velocity in the BDD is much higher (Figure 30.6). Just as in the FDD, the highest velocity is observed in the space between both sensor units (Figure 30.7). This jet of air causes a lateral air movement in the region under the sensor units to both the left and right sides. In this case, however, the flow seems to make a straight movement to the corner edges (Figure 30.8–9) of the sensor unit, where it escapes this area instead of creating a rotating flow, as in the FDD. This also causes a relatively higher velocity under the sensor unit area compared to the FDD, especially at the inner corner edges on both sides (Figure 30.10).

This higher flux of air at the under region of the sensor unit in the BDD probably also indicates a higher chance that water droplets and dirt particles carried by the air arrive at the sensor units and accumulate at their windows. This is also in agreement with the findings from practical experience.

Chapter 6

Conclusions and Recommendations

In this study, a numerical model was developed and CFD was used to describe the airflow under the SIM inspection vehicle to understand the airflow physics behind the contamination of dirt and water on sensor units mounted underneath. The simplified numerical model was validated against a wind tunnel test using a smoke visualisation technique, and the results from the experimental validation were in agreement with the findings from the numerical simulations.

After the validation, more complex configurations revealed that the movement of the rotating wheels and the relative motion between the train and the ground have significant influence on underbody flow, whilst the impact of sleepers and ballast was limited. Therefore, the former two boundary conditions were combined in an additional simulation to analyse the underbody of the SIM and the flow around the sensor units.

Conclusions from this study are summarised below, followed by recommendations for a follow-up project to design a geometric modification.

6.1 Conclusions

Based on the steps performed in this study, the following conclusions can be formulated. The results from CFD and wind tunnel tests showed that the underbody flow of the SIM is highly turbulent and complex, which is enhanced by the bottom-surface geometry, the relative motion between train and ground, and the rotating wheels. The flow at the underbody of the SIM is further characterised by a high pressure drop and large longitudinal velocity component at the nose region. The pressure slowly increases, and the velocity slowly decreases along the longitudinal length of the SIM.

When the SIM is moving in the FDD, there is an inward flow between the nose of the SIM and the ground, which is then mainly pushed to the sides, caused by the components under the SIM. In the BDD, there is an inward flow at the nose of the locomotive, passing its whole length and then streaming inward at the underbody of the SIM. The streamline which passes the bottom surface of the sensor units follows a straight path in the longitudinal direction at the underbody of both the SIM and the locomotive.

A detailed analysis of the flow near the sensor units revealed that the air under the surface of the sensors has a high vorticity, and there is a large flux of air in the space between both sensor units. The strong flux causes swirls in the area under the sensors. When driving in the FDD, these swirls are of relatively low speed. However, in the BDD, they are much more irregular and have higher velocity. Moreover, in the BDD, there is also a relatively higher flux of air moving from the inner sides to the outer sides of the sensor units before it escapes at the side edges of the sensors.

The large, open gap in the front and rear side of the SIM and the low-pressure area under the SIM cause high fluxes of air under the SIM, and it is likely that waterdrops and dirt particles carried by the air enter the bogie area and accumulate here. This can be aggravated by the dirty and wet bottom of the vehicles and the track infrastructure. As, in the BDD, the flow which passes the sensor unit first moves under the whole length of the locomotive, it is probable that this air contains more water droplets and dirt coming from the locomotive and/or pushed upwards from the track. Therefore, there is a strong potential that this air results in more pollution than when the SIM drives in the FDD. Finally, the much higher flux of air which passes the sensor units in the BDD is responsible for more pollution than in the FDD. This is also in agreement with operational experience.

6.2 Recommendations

Since this study is limited to the underbody airflow, and knowledge about particle movement under a train is limited overall, and solutions regarding geometric modification are rare, a more in-depts study to particle and droplets trajectories in combination with a geometric modification study, is recommend.

The underbody flow of a train is generally highly unsteady and therefore hard to describe and predict. This means that a full manipulation of the flow or the movement of particles is unlikely. However, there are some suggestions regarding geometric modification to multiple the underbody flow (e.g. smoothing the under surface of trains is proposed in literature to reduce underbody turbulence). However, this is not a feasible and applicable solution for this case.

A more viable recommendation is bogie fairing and the introduction of deflectors at the nose region, which are also proven solutions to reduce airflow and turbulence between the underbody surface of the train and the track. Mounting a deflector at the rear side will presumably reduce the flux of air under the SIM and thus the number of water droplets which potentially pass the sensor unit. A second, more subtle solution is reducing the flux of air in between the sensor units since flow which reaches the windows of the sensors comes from the space between them. A final recommendation is mounting extra brushes at the inner side of the sensor units to avoid the flow from the space between them easily deviating in the direction of the sensors.

To summarize, the result of this study gives a fundamental basis to perform a more in-depth study of a geometric modification of the SIM and the effect of particle and droplet trajectories on it. The findings from this follow-up project can be used to design, implement, and homologate a geometric modification which helps reducing the pollution of the sensor units and to guarantee a safe and reliable railway infrastructure.

References

Baker, C. (2014). A review of train aerodynamics Part 1 – Fundamentals. *The Aeronautical Journal*, 201-228.

Baker, C. (2019). *Train aerodynamics : fundamentals and applications.* Oxford: Butterworth-Heinemann.

Bettez, M. (2011). *Winter technologies for High Speed Rail.* Trondheim: Norwagian University of Science and Technology .

Cao, Y., Huang, J., & Yin, J. (2016). Nummeric Simulation of Three-Dimensional ice accretion on an aircraft wing. *International Journal of Heat and Mass Transfer*, 34-54.

Carretero, J., Pérez, J., & García-Carballeira, F. (2003). Applying RCM in large scale systems: a case study with railway networks. *Reliability engineering & safety*, 257-273.

CFD Module User's Guide. (2018). Burlington, Massachusetts, United States: COMSOL Inc.

Corshammar. (2005). *Perfekt spår: din framgång i järnvägsunderhåll och driftsäkerhet.* Lund, Sweden: Corshammar, P.

Deeg, P., Jonsson, M., Kaltenbach, H., Schober, M., & Weise, M. (2008). *Cross-comparison of Measurement Techniques for the Determination of Train Induced Aerodynamic Loads on the Trackbed.* Mila,, Italy: BBAA VI International Colloquium on: Bluff Bodies Aerodynamics & Application.

Driver, D., & Seegmiller, H. (1985). Features of a Reattaching Turbulent Shear Layer in Diverging Channel Flow. *American Institute of Aeronautics and Astronautics Journal*, 163-171.

Gao, G., Zhang, Y., Xie, F., Zhang, J., & Zhang, Y. (2019). Numerical study on the anti-snow performance of deflectors in the bogie region of a high-speed train using the discrete phase model. *Proceedings of the Institution of Mechanical Engineers Part F Journal of Rail and Rapid Transit* , 141-159.

García, J., Crespo, A., Berasarte, A., & Goikoetxea, J. (2011). Study of the fow between the train underbody and the ballast track. *Journal of Wind Engineering and Industrial Aerodynamics*, 1089-1098.

Giappino, S., Rocchi, D., & Schito, P. (2016). Cross wind and rollover risk on light weight railway vehicles. *Journal of Wind Engineering & Industrial Aerodynamics*, 106-112.

Huang, Z., Chen, L., & Jiang, K. (2012). Infuence of length of train formation and vestibule diaphragm structure on aerodynamic drag of high speed train model. *Journal of Fluid Mechanics*, 36-41.

Ido, A., Saitou, S., Nakade, K., & Likura, S. (2008). *Study on under-flour flow to reduce ballast flying phenomena.* Tokyo, Japan: Railway Technical Research Institute.

Kaltenbach, H., Gautier, P., Agrirre, G., Orelano, A., Schroeder-Bodenstein, K., Testa, M., & Tielkes, T. (2008). *Assessment of the aerodynamic loads on the trackbed causing ballast projection: results from the DEUFRAKO project Aerodynamics in Open Air (AOA).* Munich, Germany: Deutsche Bahn AG, DB Systemtechnik.

Kim, M., Jang, D., Hong, J., & Kim, T. (2015). Thermal modeling of railroad with installed snow melting system. *Cold Regions Science and Technology*, 18-27.

Kloow, L. (2011). *High-speed train operation in winter climate.* Stockholm, Sweden: Royal Instutute of Technology.

Kwon, H., & Park, C. (2006). *An Experimental Study on the Relationship between Ballast-Ffying Phenomenon and Strong Wind under High-speed Train* . Gyeonggi, Republic of Korea: Korea Railroad Research Institute.

Liang, X., & Shu, X. (2003). Nummeric simulation research on train aerodynamic drag affected by the train windshield. *Journal of the China Railway Society*, 34-37.

Liu, M., Wang, J., Zhu, H. K., & Zhang, Y. (2020). A numerical study on water spray from wheel of high-speed train. *Journal of Wind Engineering & Industrial Aerodynamics*, 104086.

Lyngby, N., Hoksta, P., & Vatn, J. (2008). *RAMS management of railway track.* Trondheim, Norway: The Norwegian University of Science and Technology.

Nieuwstadt, F. (2016). *Turbulentie: Theorie en toepassingen van turbulente stromingen.* Amsterdam, The Netherlands: Epsilon Uitgaven.

Niu, J., Zhou, D., & Liang, X. (2017). *Nummeric simulation of the effect of obstacle deflectors on the aerodynamic performance of stationary high-speed trains at two yaw angles.* London, England: Institution of Mechanical Engineers.

Paz, C., Suárez, C., & Cabarcos, A. (2018). Effect of realistic ballast track in the underbody flow of a high-peed train via CFD simulations. *Journal of Wind Engineering & Industrial Aerodynamics*, 1-9.

Premoli, A., Rocchi, D., Schito, P., Somaschinini, C., & G., T. (2015). Ballast flight underhigh-speedtrains: Windtunnel full-scale experimental tests. *Journal of Wind Engineering and Industrial Aerodynamics*, 351-361.

ProRail. (2021, March 7). *Programma Hoogfrequent Spoorvervoer*. Retrieved from prorail.nl.

Quinn, A., Hayward, M., Baker, C., Schmid, F., Priest, J., & Powrie, W. (2010). A full-scale field monitoring and modelling study of ballast flight under high-speed trains. *Proceedings of the Insitution of Mechanical Engineerings, Part F: Journal of Rail and Rapid Transit*, 61-74.

Ramaekers, R., Wit, d. T., & Pouwels, M. (2009). *Het Nederlandse spoorgebruik in vergelijking met de rest van de EU-27.* Den Haag/Heerlen, The Netherlands: Centraal Bureau voor de Statestiek.

Rocchi, D., Schito, P., Tomasini, G., Giappino, S., & Premoli, A. (2013). *Nummerical-experimental study on flying ballast caused by high-speed trains.* Cambridge, England: In: Proceedings of the Sixth European and African Conference on Wind Engineering.

Salvenberg, F., Bakker, P., Ooststroom, v. H., & Anne Anneman, J. (2007). *Marktontwikkeling in het personenvervoer per spoor 199-2020.* The Hague, The Netherlands: Kennisinstituut voor Mobiliteitsbeleid.

Soper, D., Baker, C., Jackson, A., Milne, D., Pen, L. L., G., W., & Powrie, W. (2017). Full scale measurement of train underbody and track forces. *Journal of Wind Engineering & Industrial Aerodynamics*, 251-264.

Tian, H. (2019). Review of research on high-speed railway aerodynamics in China. *Transportation Safety and Environment*, 1-21.

Van Velthoven - Van der Meer, S. (2018, July 12). *Kamerbrief uitgangspuntennotitie groot project Programma Hoogfrequent Spoorvervoer (PHS).* Retrieved from Rijksoverheid.nl.

Versteeg, H., & Malalasekera, W. (2007). *An Introduction to Computational Fluid Dynamics. The finite Volume Method. Second Edition.* Harlow, England: Pearson.

Wang, J., Zang, J., Xie, F., Zhang, Y., & Gao, G. (2018). A study of snow accumulating on the bogie and the eefects on deflectors on the de-icing peformance in the bogie region of a high-speed train. *Cold Regions Science and Technology*, 121-130.

Wang, J., Zang, J., Zang, Y., Xie, F., & Krajnović, S. (2018). Impact of Bogie cavity shapes and operational environment on snow accumulating on the bogies of high-speed trains. *Journal of Wind Engineering & Industrial Aerodynamics*, 211-224.

Wilcox, D. (1998). *Turbulence Modeling for CFD, 2nd Edition.* Ann Arbor, Michigan, United States: DCW Industries.

Zhang, J., Li, J., Tian, H., Gao, G., & Sheridan, J. (2016). Impact of ground and wheel boundary conditions on numerical simulation of the high-speed train aeodynamic performance. *Journal of Fluids and Structures*, 249-261.

Zhang, J., Wang, J., Wang, Q., Xiong, X., & Gao, G. (2018). A study of the influence of bogie cut outs' angles on the aerodynamic performance of a high-speed train. *Journal of Wind Engineering & Industrial Aerodynamics*, 153-168.

Zheng, X., Zhang, J., & Zhang, W. (2011). Nummeric simulationof aerodynamic drag for high speed train bogie. *Journal of Traffic and Transportation Enginineering*, 45-51.

Zhu, J., Hu, Z., & Thompson, D. (2016). Flow behaviour and aeroacoustic characteristics of a simplified high-speed train bogie. *Proceedings of the Institution of Mechanical Engineers Part F - Journal of Rail and Rapid Transit* , 1642-1658.

Summary

A common way of performing railway infrastructure inspections is with track recording vehicles equipped with optical measurement systems. By measuring track parameters such as the rail profile, for instance, infrastructure managers or maintenance contractors can evaluate rail wear to guarantee the quality and safety of the infrastructure. However, operational movement of these vehicles generates a flow of air between the car underbody and the railway track. This underbody flow is a matter of concern since airflow near the sensor units brings dirt and water droplets, which accumulate on the rail profile measuring system. This accumulation can block the view of the cameras and laser sensors and leads to inaccurate or missing measurement data.

The goal of this study is to investigate the general flow under the inspection vehicle, find its main influential parameters, and describe the flow near the optical sensors. An additional aim is to provide recommendations for a next-phase project to investigate the effect of geometric modifications on the pollution of the optical sensors.

In this study, the underbody flow of a specific inspection vehicle (SIM) is described with the help of computational fluid dynamics (CFD) simulation by using the commercial software COMSOL. A κ-ε RANS turbulence model and a simplified geometric model of the SIM and a locomotive are used to calculate the flow around and underneath the vehicle. The CFD model is qualitatively validated by a wind tunnel test using smoke visualisation techniques with a 1:18 scale model. After the validation, full-scale numeric simulations are performed, and different complexities are added

individually: relative motion between train and ground, the consideration of ballast and sleepers, and the rotation of the axels and wheels.

These full-scale simulations show a limited influence of the ballast and sleepers but a major influence of the relative motion of the ground and the rotation of the wheels and axles on the underbody flow of the SIM. Therefore, these two major complexities are combined in a single simulation for both driving directions and the results analysed.

Both the wind tunnel test and the CFD simulations indicate a highly turbulent flow and a low-pressure area under the vehicles and large swirls at the inter-car gap between the SIM and the locomotive. The complex underbody geometry of the SIM vehicle makes the flow even more irregular compared to the smoother surface of the locomotive. With the SIM as the leading vehicle, the underbody flow is straight in the first part of the vehicle and then a sideways flow to both sides for the remaining part of the vehicle. With the locomotive as the leading vehicle, the underbody flow shows as a straight turbulence flow over its whole length. Behind the locomotive, there is a highly complex multidirectional flow under and around the whole SIM caused by the wake of the relatively large locomotive.

An evaluation near the sensor unit under the SIM reveals an unsteady and irregular flow in the bogie area with high vorticity, resulting in high energy dissipation, which is reinforced by the rotating wheels and the moving ground. It also reflects a high flux of air in the space in between both sensor units, especially with respect to the moving ground condition. This large flux of air in between induces swirls in the area under the sensor boxes.

Finally, the complex geometry of the SIM, the rotating wheels, and the wake of the locomotive cause a highly turbulent flow and a low-pressure field under the vehicle. Together with the open gap between the front and rear sides of the SIM and the bogie area, this allows water droplets and dirt to easily enter the bogie area of the SIM. Moreover, the relatively high speed between both sensor units causes swirls directly under it, and small dust and water particles can accumulate on the sensor boxes. Both driving directions show these phenomena, but the main difference is the flux of air and the trajectories of the air particles which pass the sensor box. When the SIM is the leading vehicle, the air flux under the sensor units is low, and the trajectories of air particles only pass the bottom surface of the front side of the SIM. When the SIM is the trailing vehicle, the flow under the sensor units is more unsteady and has higher velocities near the sensor units, and the trajectories pass the whole length of the bottom surface of the locomotive before reaching the sensor units. It could be that water droplets and dirt from the bottom surface of the locomotive are carried by the flow of air in the direction of the sensor units. This could be the reason that, in the pulled direction, contamination of the sensor unit more often occurs.

Because the flow is highly unstable, it is hardly possible to fully eliminate dirt and water droplets, but a longer-term solution could be mounting a windshield in front of the vehicle which push the flow directly to the sides, resulting in a lower flux of air under the vehicle. In addition, filling the gap between the sensor boxes can reduce high air flow and the energy dissipation locally and prevent airflow coming in the area under the sensor box. A study into these geometric modifications and its effect on the trajectories of particles and droplets is recommended.